INFORMATION TO USERS

This manuscript has been reproduced from the microfilm master. UMI films the text directly from the original or copy submitted. Thus, some thesis and dissertation copies are in typewriter face, while others may be from any type of computer printer.

The quality of this reproduction is dependent upon the quality of the copy submitted. Broken or indistinct print, colored or poor quality illustrations and photographs, print bleedthrough, substandard margins, and improper alignment can adversely affect reproduction.

In the unlikely event that the author did not send UMI a complete manuscript and there are missing pages, these will be noted. Also, if unauthorized copyright material had to be removed, a note will indicate the deletion.

Oversize materials (e.g., maps, drawings, charts) are reproduced by sectioning the original, beginning at the upper left-hand corner and continuing from left to right in equal sections with small overlaps.

ProQuest Information and Learning
300 North Zeeb Road, Ann Arbor, MI 48106-1346 USA
800-521-0600

PREPARATION AND CHARACTERIZATION OF RAPID SOLIDIFIED YTTRIA-ALUMINA FIBERS

by

Ena Athenea Aguilar Reyes

Department of Mining and Metallurgical Engineering
McGill University
Montreal, Canada

A Thesis Submitted to the
Faculty of Graduate Studies and Research
in partial fulfillment of the requirements for the degree of
Doctor of Philosophy

August, 2000

To my parents for making it all possible.
To my husband, Carlos, and my son, Carlos Emiliano
for their unconditional love.

ABSTRACT

A melt extraction process with a new approach to making ceramic fibers was used to produce amorphous fibers in the Y_2O_3-Al_2O_3 system within the 20-30 micron size range. Three different compositions were studied, E1, Y_3A_5 and E2 with 79, 62.5 and 57.5 mol% Al_2O_3, respectively. Such fibers were X-ray amorphous and transparent, regardless of composition in the as-produced state, and showed all the principal characteristics of the fibers made by this process: a cross section which is almost circular, a line of contact with the wheel and a clean and defect-free surface. However, the quality of the fibers was controlled by the wheel edge and rotational speed, with both having a significant effect on fiber diameter and avoidance of irregularities and instabilities along the fiber length. Moreover, compositional distribution analysis showed that the melt-extracted fibers were chemically homogeneous between the core and the edge of the fiber and, in addition, were very close to theoretical stoichiometry.

Thermal analysis was performed in order to determine the glass transition, crystallization and phase transformation temperatures. E1 fibers showed two exothermic peaks at 949 and 1040 °C that correspond to the crystallization of YAG and δ-Al_2O_3 phases, respectively, and one small exothermic peak at 1300 °C due to the phase transformation of δ-Al_2O_3 to α-Al_2O_3. In the case of Y_3A_5 and E2 fibers, both showed one single exothermic peak at 942 and 939 °C due to the crystallization of YAG and YAP cubic phases, respectively. YAP orthorhombic and YAG phases appeared in E2 fibers after heat-treating at 1400 °C for 1h with no identifiable exothermic peak in the DTA scan.

Differential thermal analysis was used to study the crystallization phenomena in the as-extracted fibers. The activation energy values were calculated using both Kissinger and Augis-Bennett equations by measuring the variation of the peak temperature in the differential thermal scans with heating rate, and the crystallization mode was identified using the Ozawa analysis. After crystallization, there was a conversion of the transparent glass fiber to an opaque polycrystalline material and both E1 and Y_3A_5 fibers had a nanocrystalline microstructure with a grain size typically of 100-500 nm. In the case of E2, the grain size was 1-2 μm.

Tensile strengths and elastic moduli of the fibers in the glassy state varied from 606 to 776 MPa and from 95 to 121 GPa, respectively. Furthermore, fibers exhibited brittle fracture initiated from flaws on the fibers surface.

RÉSUMÉ

Un procédé d'extraction à l'état liquide fut utilisé pour développer une nouvelle approche de production de fibres céramiques amorphes provenant du système Y_2O_3-Al_2O_3, ayant des dimensions variant entre 20-30 microns. Trois différentes compostions furent étudiées, soit E1, Y_3A_5 et E2 contenant respectivement 79, 62,5 et 57,5 %mol. Al_2O_3. Ces fibres sont, face aux rayons X, amorphes et non influencées par la composition après production. Elles présentent les mêmes caractéristiques principales que possèdent les fibres fabriquées de cette façon: une coupe transversale presque circulaire, une surface de contact avec la roue d'extraction définie ainsi qu'une surface sans défauts. Cependant, la qualité des fibres est contrôlée par la surface de contact avec la roue et la vitesse de rotation, ces deux paramètres possédant un effet significatif sur le diamètre de la fibre et l'élimination des irrégularités et instabilités sur la longitude de la fibre. De plus, des analyses de distribution chimique montrent que les fibres sont chimiquement homogènes entre le centre et la surface et que chaque composition respective est très proche de la composition stœchiométrique théorique.

Des évaluations thermiques ont été effectuée pour déterminer les températures de transition vitreuse, de cristallisation et de transformation de phase. Les fibres de composition E1 présentent deux pics exothermiques à 949 et 1040°C, qui correspondent respectivement à la cristallisation des phases YAG et δ-Al_2O_3 ainsi qu'un autre pic de moindre intensité à 1300°C provoqué par le passage de la phase δ-Al_2O_3 à α-Al_2O_3. Dans le cas des fibres Y_3A_5 et E2, un pic exothermique singulier est observé à 942 et 939°C respectivement lors de la cristallisation des phases cubiques YAG et YAP. Les phases YAP orthothombique et YAG apparaissent pour les fibres E2 suite à un traitement thermique d'une heure à 1400°C tout en ne présentant pas de pic exothermique identifiable lors d'ATD.

Des analyses thermiques différentielles ont été utilisées pour étudier le phénomène de cristallisation des fibres extractées brutes. Les valeurs d'énergie d'activation ont été calculées utilisant et les équations de Kissinger et d'Augis-Bennett, suite à la mesure de la variation de la température des pics lors des essais thermiques différentiel en variant le taux d'augmentation de la température. Le mode de cristallisation a été identifié en utilisant l'analyse Ozawa. Suite à la cristallisation, une conversion des fibres vitreuses en matériau poly cristallin pour les fibres E1 et Y_3A_5 possédant une microstructure nanocristalline avec des grains de dimension typiquement entre 100-500 nm. Dans le cas des fibres E2, la dimension des grains est de 1-2 μm.

La résistance à la fracture ainsi que le module d'élasticité des fibres à l'état vitreux varient entre 606 et 776 MPa et entre 95 et 121 GPa respectivement. En outre, les fibres présentent des ruptures fragiles initiées par des défauts de surface.

ACKNOWLEDGEMENTS

First at all, I wish to express my gratitude to my supervisor, Professor Robin Drew, for his support and guidance throughout my graduate studies at McGill, and for providing me with the opportunity to participate in conferences to strengthen my knowledge of materials science.

A special thanks goes to Dr. Rafael Quintana of Universidad Central de Las Villas in Cuba, for his valuable comments and assistance.

I extend my appreciation to the administrative personnel in general. I am also grateful for the advice and laboratory assistance of Helen Campbell, Glenn Poirier, Monique Riendeau, Robert Paquette, Florence Paray and E. Siliasukas. A special recognition must be given to Mary Dikeakos and Dr. Zaven Altounian for DTA analysis. I would like to thank Mr. A. Gagnon, Mr. Harold Ward, and all machine shop personnel, for making wokpieces and providing me with tools and suggestions.

This work has also profited from friendship and discussions with my colleagues, both past and present, of the Department of Mining and Metallurgical Engineering, specially the advanced ceramic and composites group. Sincere thanks to José Lemus for his friendship and Mathieu Brochu for translating the abstract.

I wish to thank DLR in Cologne, Germany, for providing access to the DSC and tensile testing facilities for experimental data, especially Claudia Milz, Dr. Bernd Hildmann, and Dr. Bilge Saruhan.

I would like also to acknowledge CONACYT (Consejo Nacional de Ciencia y Tecnologia, Mexico) for granting me a scholarship and NSERC (Natural Science and Engineering Research Council of Canada) for partial support of this research.

On a personal level, I specially thank my parents, brothers and sisters for all that they have done to help along the way. I would like to thank my husband, Carlos, and my son, Carlos Emiliano, for their encouragement, patience, and understanding.

TABLE OF CONTENTS

LIST OF FIGURES

Chapter 2

Chapter 3

Chapter 4

Chapter 5

Appendix A

Appendix B

LIST OF TABLES

Chapter 2

Chapter 3

Chapter 4

Chapter 5

CHAPTER 1

INTRODUCTION

Continuous oxide ceramic fibers are attractive as reinforcing phases for high-temperature structural materials since they combine high strength and elastic modulus with high-temperature capabilities and a general freedom from environmental attack. They also possess good thermal properties because of their higher melting points and lower thermal expansion coefficients. The incorporation of ceramic fibers into polymers, metal alloys, and ceramics has the potential for providing substantial property improvements over monolithic materials. Of critical importance in the fabrication of reinforced composites are the properties of the reinforcement phase and of the interface between the reinforcement and the matrix [1, 2].

Motivated by aerospace applications requiring composite materials that are lightweight, stiff, and strong, fiber research and development efforts over the last two decades have resulted in a variety of commercially available high performance, continuous fibers with low densities (< 4 gm/cm^3), high Young's moduli (> 200 GPa), and high tensile strengths (> 1 GPa). However, for certain applications requiring high structural reliability,

very few of these fibers are ideally suited as reinforcement for either metal matrix composites (MMC) or ceramic matrix composites (CMC). That is, in their current production state, these commercial fibers fail to meet all the necessary property requirements for providing MMC or CMC with high strength and toughness [3, 4].

On the other hand, the system Y_2O_3-Al_2O_3 is a promising material for refractory coatings and for ceramic and semiconductor technologies. Doped single crystals of yttrium aluminates are widely used in lasers and polycrystalline yttrium aluminium oxide ceramics are a very important family of advanced ceramic materials. In addition, the translucent ceramics of this system are known to be useful optical materials. Yttrium aluminum garnet or YAG, has been used widely as a laser host material [5]. It has promising properties for applications such as high temperature coatings and high temperature structural components. For structural applications, the bulk material may be used in the monolithic form or as the matrix phase for composites. In either case, an important requirement is that the fabricated material must have nearly full density and a controlled grain size.

Although their potential as a matrix material has been investigated [6-11], there is a relatively little known about the behavior of YAG and Al_2O_3-YAG eutectic fibers, as the few which exist are still in the developmental stages. Al_2O_3-YAG eutectic fibers have been produced using an edge-defined film-fed growth technique (EFG) and a laser heated float zone method (LHFZ) [12-14] and exhibit properties substantially better than those reported for monolithic ceramics prepared in a similar manner. Morscher [15] has investigated the creep behavior of YAG fibers prepared using alkoxide sol-gel precursor. King [16, 17] has prepared

YAG fibers by dry spinning solutions of yttrium and aluminum carboxylate polymers (precursor route) and by dry spinning aqueous oxide sols (sol-gel route). Other investigations have produced Al_2O_3-YAG eutectic and YAG fibers by using the sol-gel method [18, 19], using alkoxides, aqueous and metal oxohydroxopropionates precursors and by extrusion of a mixture of a thermoplastic polymer and YAG powder [20]. Recently, YAG glass fibers were produced by pulling from undercooled molten oxide precursor [21].

The melt extraction technique is a very rapid and low cost fiber fabrication method compared to other current ceramic high performance fiber fabrication methods. These other techniques include chemical vapor deposition (CVD), used to grow ceramics on tungsten and graphite filaments, the pyrolisis of cured polymer fibers, slurry processing of a ceramic powder and organic polymer mixture and diffusion based sol-gel processing of metal alkoxides. Ceramic fibers of CaO-Al_2O_3, ZrO_2-Al_2O_3, ZrO_2-Al_2O_3-SiO_2, ZrO_2-Al_2O_3-TiO_2, have been produced using the melt extraction process [22]. This technique allows fibers to be made from materials that form inviscid melts, i.e. have very low viscosity, generally < 0.1 Pa·s. In order to decrease the ceramic melting temperatures, eutectic compositions of binary or ternary ceramic systems are used in melt extraction.

The content of this thesis includes several chapters dealing with various aspects of melt extraction. The literature review, *Chapter 2*, describes advanced inorganic fibers, focuses on principles and concepts, analyses experimental and commercial processes, and relates process variables to structures, fiber properties and end-use performance. General

properties of oxide compounds used in this study are highlighted in the second part of the literature review. This chapter is closed by introducing the fundamentals of glass formation and crystallization. The experimental procedure is reviewed in *Chapter 3* and is followed by the results of fiber production and characterization in *Chapter 4*. Morphology, crystallinity, compositional distribution and mechanical properties of the fiber in the as-produced state are addressed in this chapter. In *Chapter 5*, the results of crystallization and kinetics are described, and includes crystallization of the amorphous fibers that focuses in the phase and microstructural evolution as a function of temperature and concludes with the calculation of kinetics parameters of crystallization. Finally, conclusions are given in *Chapter 6*, followed by recommendations for further investigation.

1.1 Objectives

Current technology for fiber synthesis is limited in the composition of materials from which fibers can be formed, the quality and diameter of the fibers than can be obtained, and the compatibility with coating and matrix materials that may be used in composites. The relatively high cost of oxide fibers available for composites materials also makes research and development very expensive.

The main objective of this research is to demonstrate the potential production of fine and high quality ceramic fibers in the Y_2O_3-Al_2O_3 system by a rapid solidification process, namely melt extraction technique.

Since one of the potential applications of oxide ceramic fibers is as a reinforcing phase to produce composites materials for high temperature applications, another objective of this work involves a fundamental study of the thermal behavior of the fibers through thermal analysis to determined crystallization temperatures, activation energies, and crystallization mode, as well as phase development and microstructural evolution.

Other objectives of this work are:

- Characterization of the fibers in the as-produced state relating to morphology and surface characteristics, evaluation of crystallinity and distribution of chemical composition.
- To assess tensile mechanical properties of the fibers in the as-produced state, and characterization of the strength distribution in the ceramic fibers by Weibull statistics.
- Examination of the phase composition of the fibers after quenching from the melt and annealing.

CHAPTER 2

LITERATURE REVIEW

PART I. INORGANIC FIBERS

During the last quarter of a century great progress has been made in the development of high-performance materials. One of the important reasons for this progress has been the production of inorganic or ceramic fibers with high tensile strength and modulus values as well as resistance to high temperatures. The incorporation of these fibers into advanced ceramics, polymers, and metals has produced composites with superior properties which have created new engineering possibilities. As a result, composites containing these inorganic fibers have made possible the construction of exotic space vehicles as well as superior sports equipment. Composites have provided lightweight structural materials with high strength and modulus values that can be tailored to meet specific loading conditions for aircraft. Composites are used in space vehicles because of their light weight, high strength, and resistance to high temperatures. Composites are used in military and civilian aircraft because they increase range, payload, and fuel consumption. In the sporting world, composites are used in racing car

bodies, boat spars, bicycle frames, golf club shafts, tennis racquet frames, and fishing rods [23].

2.1. Classification of Fibers

Fibers can be classified in a variety of ways. For example, the whole field of fibers may be divided into apparel and nonapparel fibers, i.e. based upon the final use of fibrous material. The apparel fibers include synthetic fibers such as nylon, polyester, spandex, and natural fibers such as cotton, jute, sisal, ramie, silk, etc. Nonapparel fibers include aramid, polyethylene, steel, copper, carbon, glass, silicon carbide, and alumina. These nonapparel fibers are used for making cords and ropes, geotextiles, and structural applications such as fiber reinforcements in a variety of composites and they possess higher stiffness and strength and a lower strain to failure than the apparel fibers. They are also characterized by rather difficult processing and a drastic strength degradation by the presence of small flaws, i.e. they generally have a low toughness.

Another classification of fibers can be made in terms of fiber length, continuous or staple fibers. Continuous fibers have practically an infinite length while staple fibers have short, discrete lengths (10-400 mm). Like continuous fibers, these staple fibers can also be spun into a yarn, called staple fiber yarn. This ability to be spun into a yarn can be improved if the fiber is imparted with a waviness or crimp. Staple fibers are excellent for providing bulkiness for filling, filtration, etc. Frequently, staple natural fibers (cotton, wool) and staple synthetic fibers (nylon, polyester) are blended to obtain the desirable characteristics of both.

Yet another convenient classification of fibers is based on natural and synthetic fibers, as shown in Figure 2.1.

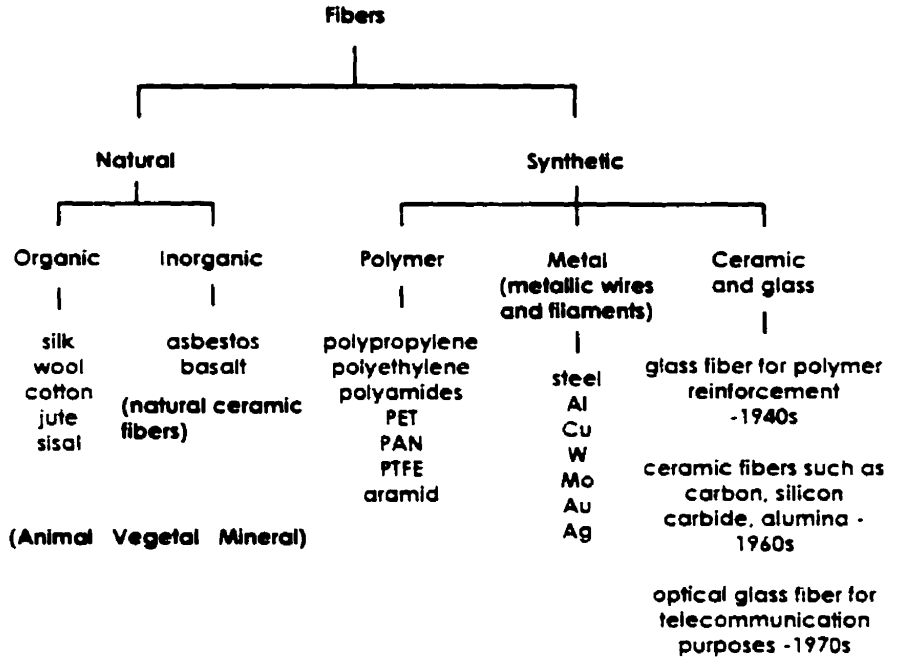

Figure 2.1 Classification of fibers based on natural and synthetic fibers.

Natural fibers occurring in the vegetable or animal kingdom are polymeric in terms of their chemical constitution, while natural fibers in the form of minerals are related to crystalline ceramics. A distinctive feature of natural fibers is that they are generally a mixture (chemical or physical) of different compounds. Synthetic fibers can further be classified as polymers, metals, ceramics or glass. Here, a very special and unique subclass of fibers should also be mentioned, *whiskers*. The term whisker is usually applied to single crystals having such a high degree of growth anisotropy that they have fibrous or fibrillar characteristics. Compared to polycrystalline continuous or discontinuous fibers, they commonly have exceptionally high tensile strength and high

modulus of elasticity. Whisker diameters range from 1 to 25 μm with aspect ratios between 100 to 15000 [24, 25].

2.2 Fiber Properties Requirements (Stiff and Strong Fibers)

As it was pointed out earlier, fibrous material is found extensively in nature. Up until the mid-twentieth century, most of the usage of fibers had been in clothing and other household uses. About the middle of the twentieth century, high performance fibers became available for use in a fabric form or as reinforcements for making composites. The use of fibers as high performance materials in structural engineering applications is based on three important characteristics:

(i) A small diameter with respect to its grain size or other microstructural unit. This allows a higher fraction of the theoretical strength to be attained than that possible in a bulk form. This is a direct result of the so-called size effect, namely the smaller the size, the lower the probability of having an imperfection of a critical size that would lead to failure of the material. Thus, even for a material in its fibrous form, its strength decreases as its diameter increases.

(ii) A very high degree of flexibility which is really a characteristic of a material having a high modulus and a small diameter. This flexibility permits a variety of techniques to be employed for making fabrics, ropes, cords, and fiber reinforced composites with these fibers.

(iii) A high aspect ratio (length/diameter, l/d) which allows a very large fraction of applied load to be transferred via the matrix to the stiff and strong fiber in a fiber reinforced composites.

The most distinctive feature of a fibrous material is that it has properties highly biased along its length. Fibers, in general, and continuous fibers, in particular, are very attractive for the reasons given above. A given material in a fibrous form has a high aspect ratio (length/diameter) and can be highly flexible. Such a flexible fiber can be made into yarn, which in turn can be braided, knitted or woven into rather complex shapes and forms. Some materials are inherently brittle in their bulk form such as glass, alumina, or silicon carbide, etc. In the form of an ultra fine diameter fiber, they can be as flexible as any organic textile fiber, such as nylon that is commonly used. Quite frequently, a material in a fibrous form has a higher strength and, sometimes, as in a highly oriented fiber, even a higher elastic modulus than in the bulk form. These characteristics have led to the development of fiber-reinforced composites with a variety of matrix materials such as polymers, metals, glasses, and ceramics.

The important fiber properties required for structurally reliable MMCs and CMCs are listed in Figure 2.2. Although many are generally independent of matrix character, there are some, such as fiber diameter and interfacial bonding, which are strongly dependent on whether the matrix deforms plastically or elastically. These aspects can best be appreciated by considering the deformation and fracture mechanisms controlling strength and toughness for each composite type.

GENERAL FIBER REQUIREMENTS:

* Continuous (High length/diameter ratio)
* High volume fraction aligned in load direction
* High tensile strength

High strength retention under composite fabrication conditions

Thermal expansion near that of the matrix

SPECIFIC FIBER REQUIREMENTS:

MMC (Ductile matrix):

Strong matrix bonding

* Large diameter

CMC (Brittle matrix):

* High modulus
* Creep resistant
* Small diameter

Weak matrix bonding

High strength retention in air and other service environments

Figure 2.2 Fiber property requirements for structurally reliable MMCs and CMCs. Asterisks indicate those that are generally independent of matrix chemical and physical properties.

2.2.1 Strong and Tough MMCs

Assuming a ductile metal matrix, fiber-controlled composite fracture, and unidirectional composite loading, the general microstructural requirements for a strong MMC are the alignment in the load direction of a high volume fraction of high strength fibers which are equally strained under composite loading. This implies that the reinforcing fibers must be continuous (high length to diameter ratio), be strongly bonded

to the matrix (for good load transfer), possess a high as-produced tensile strength, and be capable of retaining a large percentage of this strength under the fabrication and service conditions typically encountered with the MMC.

Because high performance fibers typically fracture in a brittle manner, strength retention problems relate to fiber abrasion during composite processing and to fiber-matrix reaction during high temperature composite processing and use. These problems can degrade composite strength by creating new flaws on the fiber surface and also by forming these flaws with a high density along the fiber length. High flaw density implies a greater probability that neighboring fibers will have critical flaws on the same transverse plane, so that upon individual fiber fracture, the composite is more likely to experience a low-strength cleavage-type of fracture. Another strength degradation problem relates to fiber-matrix thermal expansion mismatch which upon composite thermal cycling, can introduce undesirable residual stresses and subsequent in-situ fiber fracture or fiber-matrix debonding.

For tough MMCs, the general microstructural requirements are that high stresses be needed to fracture fibers at the tip of composite cracks and that the stress concentrations at the crack tips be as low as possible. The first requirement again implies the need for fibers with high in-situ tensile strength with a low linear density of critical flaws. The second requirement implies that full advantage should be taken of the crack blunting capabilities of the ductile metal matrix. This can be achieved by maximizing the interfiber spacing without reducing fiber volume fraction. Since interfiber spacing

increases with increasing fiber diameter, tough MMCs should contain very strong fibers with as large a diameter as possible within the dimensional constraints of the particular application.

High in-situ strength and large diameter are also important in achieving MMC with high-energy absorption capability under mechanical impact. The high fiber strength allows the fibers to absorb maximum elastic energy before fracturing. The large fiber diameter allows the ductile matrix between fibers to contribute maximum plastic energy absorption under the shear-type deformation modes often encountered under impact conditions.

2.2.2 Strong and Tough CMCs

Typical CMC macroscopic fracture is not initiated by fiber fracture as in MMCs but by the low-strain propagation of inherent microcracks within the as-produced brittle matrix. This difference in fracture mechanism results in significantly different fiber properties required for achieving high strength and high toughness CMC.

To illustrate this, consider Figure 2.3 which is a schematic of the stress-strain curves typically encountered for monolithic ceramics and for CMC with continuous reinforcing fibers aligned along the load direction. For an unreinforced monolithic matrix with elastic modulus E_m, low temperature fracture is initiated by processing-related bulk flaws at an average applied strain ε_m and an average applied stress $\sigma_m=E_m\varepsilon_m$. The initial departure from non-linearity in the CMC stress-strain curve results from cracking of the

matrix. For the non-catastrophic mode of failure, the first crack in the matrix extends indefinitely, breaking only a small fraction of fibers. Further loading causes formation of periodic matrix cracks, with spacing dictated by a characteristic stress transfer length associated with the bridging fibers. These cracks divide the composite into "blocks" of matrix held together by intact fibers. The ultimate strength is determined by fiber bundle failure, with the tail of the curve corresponding to pullout of broken fibers. The extent of this fiber pullout region depends critically on the interfacial frictional resistance, τ_i.

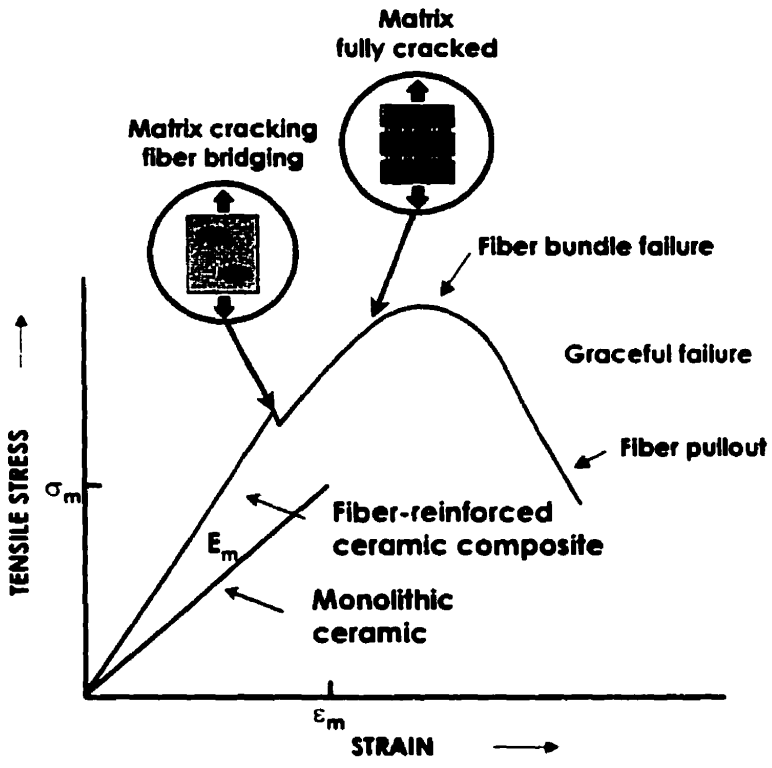

Figure 2.3 Schematic of typical stress-strain curves for monolithic ceramic and CMC with continuous fibers aligned in the load direction.

High composite fracture strain is achieved by avoiding formation of larger matrix flaws during composite processing than the flaws typically formed during monolithic

matrix processing. Another method involves high concentration of fibers bridging the matrix microcracks. Under composite loading, these bridging fibers reduce crack openings, thereby requiring greater applied strains for matrix crack propagation than those needed in the reinforcing matrix.

If the fiber-matrix interfacial bonding is strong, the stress concentration on fibers at the crack tip, due to previously initiated matrix crack propagation, will generally be high enough to fracture the fibers. This results in a low-toughness cleavage-type of CMC fracture. However, if the interfacial bonding is weak, matrix cracks will propagate around the fibers and not through them. If the load carrying ability of the fibers is high enough to support the full-applied load, then, as each the critical matrix crack propagates to the composite surface, the composite will elongate but will not fracture catastrophically. The resulting CMC fracture appears as a series of macroscopic matrix cracks that are bridged by the reinforcing fibers.

The above description of CMC deformation and fracture suggests that a strong CMC should contain a high volume fraction of fibers that are continuous, stiffer than the matrix, and possess a small diameter. The first two properties serve to increase composite stiffness, thereby increasing the stress level needed to produce macroscopic composite fracture. Under elastic deformation conditions at low temperature, high fiber stiffness implies high modulus. Under time-dependent deformation conditions at high temperature, high fiber stiffness implies both high modulus and high creep resistance.

The high volume fraction and small diameter properties insure that a sufficient number of fibers bridge the processing-related matrix microcracks. This prevents microcrack propagation until higher strain levels. An additional performance advantage of a small diameter fiber is that the fiber length required for full fiber-matrix load transfer (critical transfer length) is also small. This critical length increases with diminishing interfacial bonding strength. Thus, with a smaller fiber diameter, maximum composite performance (e.g., stiffness) can be more readily achieved, even in CMC of small dimensions.

Small diameter fibers in CMC also reduce the risk of introducing processing related flaws that are larger than the typical inherent matrix flaws. These new flaws could arise from the low strain fracture of individual fibers weakened during composite processing, or perhaps from unconsolidated matrix material between fibers. In either case, the size of the new flaws might be expected to be close to that of the fiber diameter.

The CMC should contain a high volume fraction of continuous fibers that are weakly bonded to the matrix, possess a high in-situ tensile strength, and are capable of retaining a high percentage of this strength in air and other service environments to which the CMC will be exposed. These prerequisites will facilitate operation of the high strain mechanism in which fibers bridge macroscopic matrix cracks [1, 3, 4, 26, 27].

The increase in the requirements for the thermal and chemical stability of fibers and the efficiency of using composites with metallic and ceramic matrices has stimulated

great interest from oxides, carbides, nitrides, borides, and other ceramic materials. Ceramic fibers can be used to reinforce composites with any matrices, ensuring a broad set of properties for manufactured articles [28].

2.3 Ceramic Fibers

2.3.1 Inorganic Ceramic Fibers

Synthetic ceramic fibers have been available for the reinforcement of light alloys from the beginning of the 1960s. The earliest fibers were produced by chemical vapor deposition onto a tungsten substrate, first to give boron and then silicon carbide fibers. Carbon fibers were also developed around this time and attempts were soon made to use them as reinforcements for aluminum. Composite structures consisting of aluminum or magnesium reinforced with these fibers have been developed and have found a limited number of applications. The reactivity of carbon with the metal matrix has still not been completely surmounted and research continues in this area. However the oxidation of carbon above 400 °C limits the use of carbon fibers at high temperature in the presence of oxygen. Silicon carbide fibers produced by CVD onto tungsten or carbon cores today represent the only viable reinforcement for titanium metal matrix composites. Such fibers are produced with a sophisticated protection barrier which makes possible titanium matrix composites for use up to 600 °C.

Short fine alumina-silica fibers were produced in the early 1970s and these fibers, under the name Saffil, today represent the most widely used filamentary reinforcement for light alloys. Small diameter continuous α-alumina fibers were produced in the 1970s

and began to be incorporated into metal matrix composites towards the end of that decade. The composites which were produced showed great improvements in stiffness and creep resistance when compared to unreinforced aluminum. However high cost and the brittleness of the fibers which were then available limited their use. Since 1980 other fibers based on alumina plus a small amount of silica or mullite, have been produced, which are easier to handle, with the result of reducing their Young's moduli and their creep resistance.

The development in the early 1980s of small diameter fibers based on silicon carbide and produced by the conversion of an organo-silicon precursor has generated much interest in the possibility of producing ceramic composites capable of being used for long periods in air above 1000 °C. These fibers retain their properties up to 1000 °C when heated in air, although above this temperature their strength falls due to internal modifications of the structure. Also, because of their non-stoichiometric microstructure, their mechanical properties are not those of bulk silicon carbide. The most recent generation of small diameter ceramic fibers of this type have been produced with a modified microstructure destined to improve their high temperature stability. Long term stability in air at 1300 °C to 1400 °C is the aim of this type of fiber. For temperatures above this range, hope resides with oxide fibers, either with carefully controlled microstructures, so as to avoid problems at grain boundaries, but also to limit dislocation mobility, or with the development of oriented single continuous crystal filaments.

Advances in this field are occurring rapidly and the goal is to enable composites to be produced that will considerably extend the temperature range of advanced structural materials.

The last quarter of the twentieth century saw tremendous advances in the processing of continuous, fine diameter ceramic fibers. Figure 2.4 provides summary of some of the important synthetic fibers that are available commercially. Two elemental fibers have been included, carbon and boron, while the amorphous ones, silica-based glasses, have been excluded. Two main categories of synthetic ceramic fibers are: oxide and nonoxides. A prime example of oxide fibers is alumina while that of nonoxide fibers is silicon carbide [24].

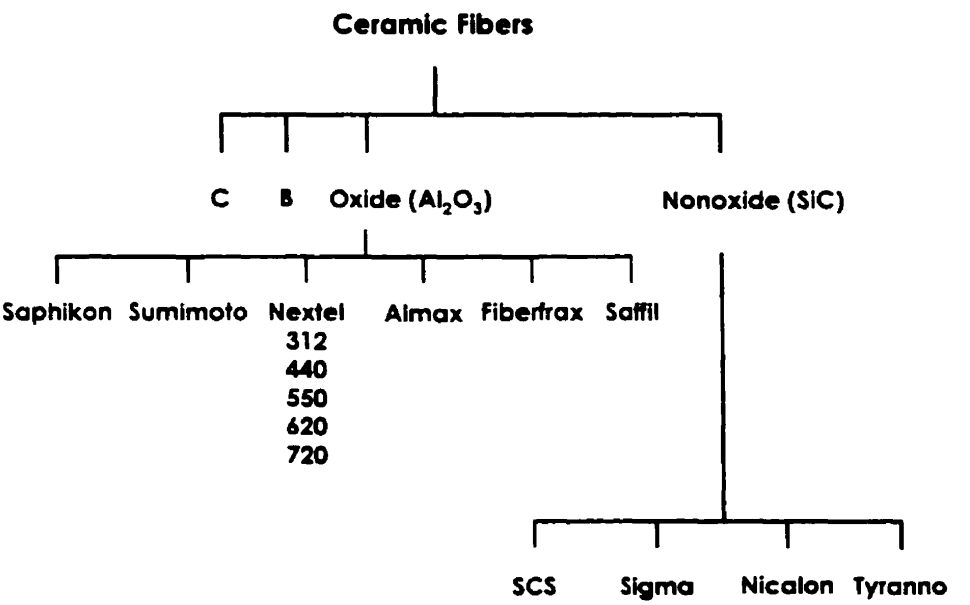

Figure 2.4 Some of the important synthetic ceramic fibers that are available commercially.

2.3.2 Fabrication Methods of Oxide Fibers

Slurry Spinning Methods

In the slurry process, an aqueous suspension of Al_2O_3 particles is prepared that can contain dissolved organic polymers such as poly(vinyl alcohol) to increase viscosity of the slurry and to stabilize the suspension of the particles; also, aluminum salts can be added to aid densification at the sintering stage, and other additives may include materials to control grain growth. The slurry is extruded into air, dried, and then fired at a low temperature to permit shrinkage without distortion. Finally, the fiber is flame fired to eliminate porosity and complete the conversion to α-Al_2O_3, the high-temperature-stable and high modulus value crystalline form.

The first small diameter continuous ceramic fiber became available in 1979 from Du Pont consisted of almost pure α-alumina and was called **Fiber FP**. This fiber, which had a grain size of 0.5 μm and a diameter of 20 μm, had a low strain to failure which made it difficult to handle and this limited its use and eventually caused its withdrawal from production. However, the FP fiber retained its strength up to around 1000 °C. From this temperature, however, intergranular plasticity accompanied by grain growth occurred when the fiber was under load, generally weakening it. At these temperatures the fibers were seen to creep.

Fiber FP is a continuous α-alumina yarn with a 98% theoretical density. The three basic steps involved in the basic fabrication procedure are as follows:

(i) The spin dope is either a dispersion of a fine α-Al_2O_3 powder (e.g., 0.5 μm mean size) or an ultrafine γ-transition alumina powder (0.02 μm mean grain size) in an aqueous solution of a basic aluminum chloride, for example, the water soluble $Al_2(OH)_5Cl \cdot 2H_2O$ salt containing various additives, including (a) high molecular weight polymers acting as spinning aids, (b) sintering aids and (c) a grain growth inhibitor such as MgO (as magnesium chloride).

(ii) The dope is concentrated by heating under vacuum and is then dry spun through a spinneret from this spinnable slurry.

(iii) Finally, the dry spun yarn is subjected to two-step firing: Low firing controls the shrinkage (300 to 800 °C to devolatilize and calcine) while flame firing improves the density of α-Al_2O_3 (at temperatures up to 1800 °C). A thin silica coating is generally applied. It serves to heal the surface flaws, giving about 50% higher tensile strength than the uncoated fibers. Figure 2.5 gives the flow diagram and fiber FP process [23, 24, 28].

A later candidate for reinforcing light alloys produced by Du Pont was the **PRD 166 fiber**. This fiber was microcrystalline based on α-alumina but containing approximately 20 wt% of tetragonal zirconia partially stabilized with yttrium oxide. Fiber PRD-166 which has been produced by the slurry process, is manufactured in tows of 200 filaments of 20 μm in diameter. The largest α-alumina grains were of the order of 0.3 μm. The zirconia had a size of 0.1 μm and was located at triple points of alumina grains ant its role was to improve strength and toughness, which resulted in a slight

improvement in strain to failure compared to the FP fiber. At high temperatures the PRD-166 fiber showed greater resistance to creep which began at 1100 °C. The PRD-166 fiber only reached the pilot plant stage and was not taken to production.

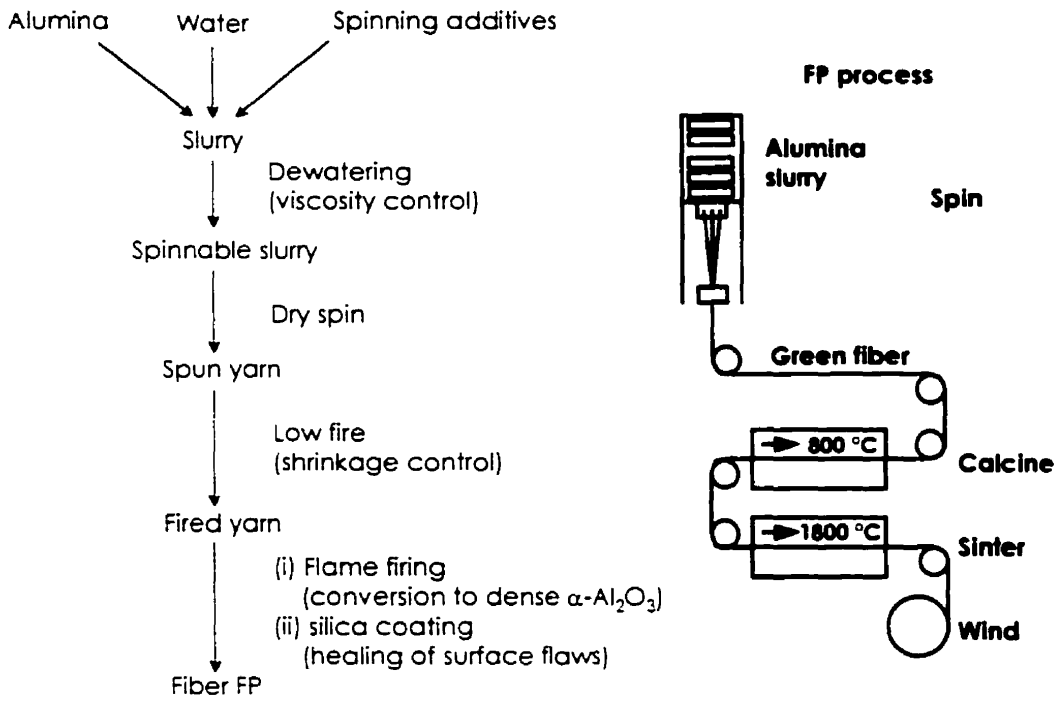

Figure 2.5 Flow diagram and process of fiber FP (Al_2O_3) fiber.

The alumina-based fibers from Du Pont were not developed into commercial products. However other producers now make commercial fibers based on α-alumina. Mitsui Mining produces the **Almax fiber** by slurry spinning with a diameter of 10 μm, which allows it to be woven. These fibers have a microstructure which is more porous than FP fibers and which also shows considerable internal stresses. This leads to a lower

density, failure stress and Young's modulus, and, at high temperature, easier grain boundary sliding and grain growth.

Sol-Gel Methods

In the solution or sol-gel process, viscous, concentrated solutions of aluminum compounds are spun, followed by drying and heat treatment of the fiber. The solvent in the spinning solution may be either water or an organic solvent. In aqueous spinning, the aluminum compounds may be basic aluminum chlorides, to which are added water-soluble polymers, to control the rheology of the spinning solution, and other additives for control of phase stabilization and grain growth. One of the additives may be SiO_2. The resulting viscous solution is extruded through an orifice into dry air or onto a rapidly rotating disk. The fiber is exposed to increasing temperatures to remove HCl from $AlCl_3$, burn off organic matter, and form a crystalline Al_2O_3. After the HCl and organic matter are removed, an amorphous Al_2O_3 initially forms; then, with increasing temperature, the Al_2O_3 becomes crystalline, the crystal form changing from η through γ, δ, θ, and finally to α.

As the temperature is increased, not only do the crystal forms change, but grain size increases and porosity decreases. With these changes there is a simultaneous decrease in tensile strength and shrinkage at high temperatures, as well as increases in elastic modulus, crystallinity, and stability.

Yet another variety of alumina fiber available commercially is δ-Al_2O_3, a short staple fiber produced by ICI (trade name **Saffil**). Saffil fibers were first produced by ICI in 1972 as refractory insulation and have since become the most widely used filamentary reinforcement for light alloys. These fibers are short in length, have a diameter of 3 μm and consist of approximately 97% of δ-alumina and 3% of silica.

A sol-gel method is used to produce silica-stabilized alumina (Saffil) and calcia-stabilized zirconia fibers. The flow diagram is shown in Figure 2.6.

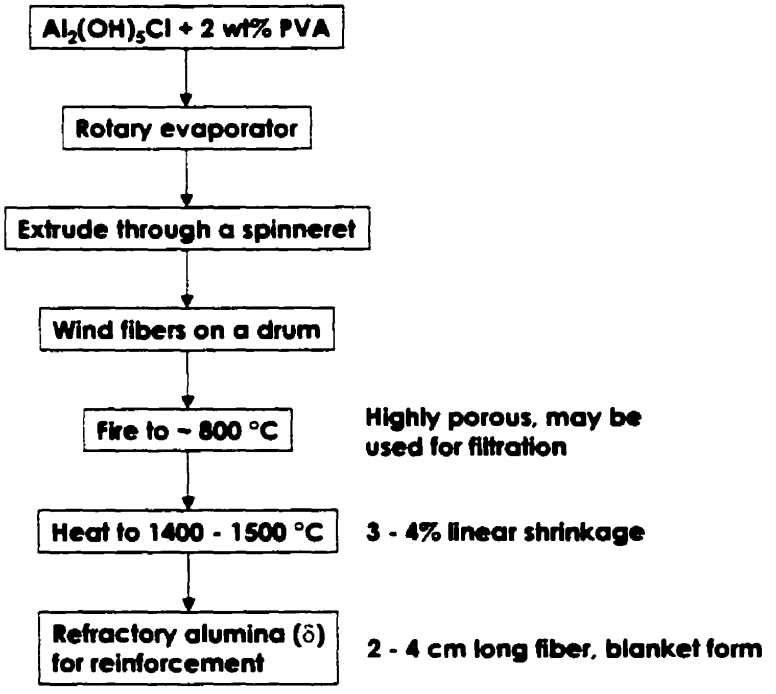

Figure 2.6 Flow diagram of sol-gel processed δ-alumina, staple fibers (Saffil).

For Saffil alumina fiber, aluminum oxychloride [$Al_2(OH_5)Cl$] is mixed with a medium molecular weight polymer such as 2 wt % polyvinyl alcohol. The aqueous phase contains an oxide sol and an organic polymer. This solution is slowly evaporated in a rotary evaporator until a viscosity of about 80 $Pa \cdot s$ (800 poise) is attained. This solution is extruded through a spinneret, and the fibers are wound on a drum and fired to about 800 °C. The organic material is burned away and a fine-grained alumina fiber having 5-10 % porosity and a diameter of 3-5 μm is obtained. The fibers produced at this stage are suitable for filter purposes because of their high porosity. By heating them to 1400-1500 °C which causes a 3-4 % linear shrinkage, one obtains a refractory alumina fiber suitable for reinforcement purposes.

Sumimoto Chemical Co. produces a mixture of alumina and silica fiber (**Altex fiber**). The flow diagram of this process is shown in Figure 2.7. Basically, the process starts with an organoaluminum (polyaluminoxanes or a mixture of polyaluminoxanes and one or more kind of silicon-containing compounds) and a precursor fiber is obtained by dry spinning. This precursor fiber is calcined to produce the final fiber. Compositionally, this fiber consists of crystalline gamma alumina + amorphous silica.

The γ-alumina fiber contains 15 wt % of silica and this leads to a much lower Young's modulus than that of the α-alumina fibers but a greater strain to failure and therefore easier handling. The alumina crystallizes in the γ phase with a very fine grain

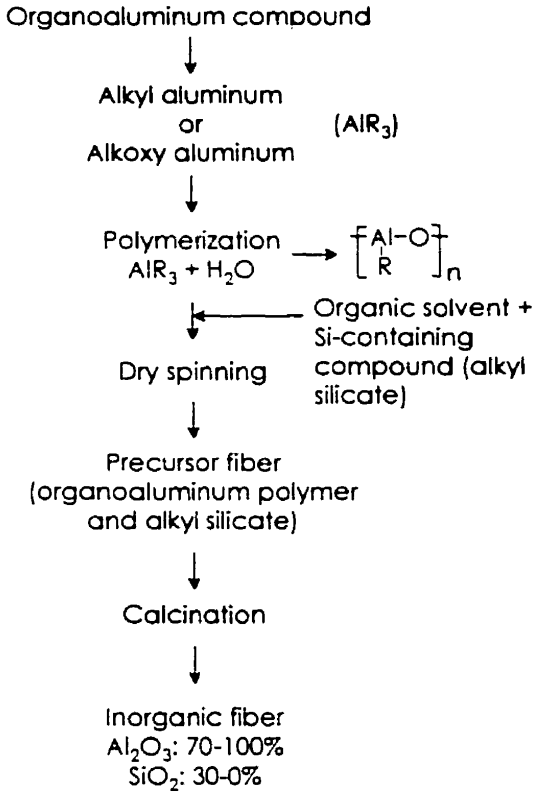

Figure 2.7 Flow diagram of an alumina + silica fiber production (Altex).

size, a low density, and an active surface. The role of the silica, which is amorphous and makes up 15 wt % of the structure, is to stabilize the alumina in the γ phase. The fibers conserve their strength and stiffness at least up to 800 °C with little noticeable loss in tensile properties at 1000 °C. Above this temperature the tensile properties fall and at temperatures above 1150 °C the fiber deforms plastically. The fiber is observed to suffer considerably from creep above 1000 °C. Above 1100 °C, softening of the silica accounts for the rapid acceleration of the creep processes. Heat treatment produce changes in the diffraction pattern with the appearance of mullite at and above 1127 °C. The rate at which the structure is converted to mullite is strongly temperature dependent. An excess of

alumina exists after the conversion to mullite due to insufficient silica being in the structure with which to combine with the alumina.

An important polycrystalline α-alumina fiber has been developed by 3M. This α-alumina fiber, trade name **Nextel 610**, is made via a sol-gel route. The sol-gel process of making fibers involves the following steps common to all sol-gel processing:

(i) Formulate sol;

(ii) Concentrate to form a viscous gel;

(iii) Spin the precursor fiber;

(iv) Calcine to obtain the oxide fiber.

Specifically, in the case of the 3M process of making Al_2O_3 fiber, the following steps are involved:

(i) Use an organic basic aluminum salt solution as the starting material.

(ii) Drive out the organics by decomposing and volatilizing without causing cracking, blistering, or other defects.

(iii) Final firing at 1400 °C under carefully controlled conditions.

(iv) A low temperature straightening treatment.

Figure 2.8 shows the 3M process schematically.

The Nextel 610 has been developed by 3M, has a diameter of 10 μm and is composed of α-alumina with 1.15% total impurities including 0.67% Fe_2O_3 as a

nucleating agent and 0.35% SiO_2 as grain growth inhibitor. The grain size is one fifth the size of the alumina grains in the FP fiber, having a size of 0.1 μm. The fiber possesses a failure stress of 1.9 GPa, a strain to failure of 0.5% and a Young's modulus of 380 GPa. Creep resistance is better than that seen with the Almax fiber, which has the same diameter, but is not improved, compared to the FP fiber.

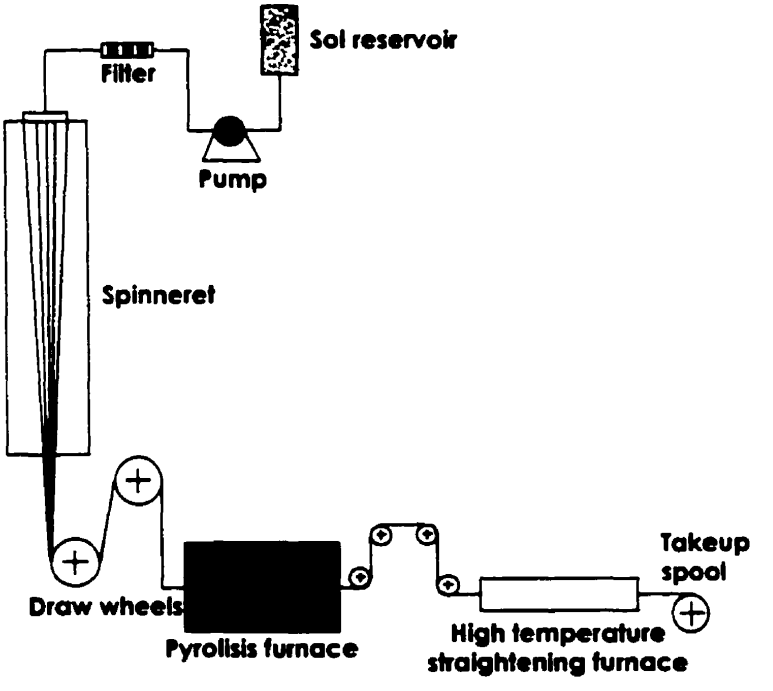

Figure 2.8 Schematic of the 3M process of making alumina fiber.

There exists several fibers based on phases of alumina other than α-alumina and in which silica is added, but in differing amounts, to inhibit grain growth. The greater the

percentage of silica the greater the strength of the fiber but the lower the Young's modulus and also the lower the resistance to creep.

The Nextel series of fibers produced by 3M are mainly based on a mullite composition with varying percentages of boron oxide to restrict grain growth. The fibers are oval in cross section, due to solvent and shrinkage induced by filament drying during the sol-gel fabrication process, but a study by image analyses gives an average diameter of 11 μm. The **Nextel 312** fiber is a specific case. Although its Al_2O_3/SiO_2 molar ratio is that of nominal mullite, it also contains a large amount of boria. When fired at 900-1100 °C, the fiber consists of an aluminum borosilicate crystalline phase mixed with amorphous silica. If the firing temperature is raised above 1100 °C, a quite significant weight loss occurs due to B_2O_3 volatilization. As a result, the chemical composition of the fiber is shifted toward that of mullite with a grain size increase [29]. The **Nextel 440** fiber consists of two crystalline phases, one of mullite and the other of γ-alumina in amorphous silica, with a much reduced boria content. The more crystalline **Nextel 480** (no longer available), contained only mullite as a crystalline phase and much reduced boron oxide. The grain size in this latter fiber was 50 nm and the structure is not fully evolved up to 1200 °C except for the completion of the mullite crystallization. The manufacturer reports that the Nextel fibers conserve at least 75 % of their properties up to 1000 °C and that they creep over 1000 °C. Data from the manufacturer gives an activation energy of 472 kJ/mol which is close to that found for the Altex fibers.

The sol-gel manufacturing process used by 3M uses metal alkoxides as the starting materials. Metal alkoxides are M(OR)*n* type compounds where M is the metal, *n* is the metal valence, and R is an organic compound. Selection of an appropriate organic group is very important. It should provide sufficient stability and volatility to the alkoxide so that M-OR bond is broken and MO-R is obtained to give the desired oxide ceramics. Hydrolysis of metal alkoxides results in sols that are spun and gelled. The gelled fiber is then densified at intermediate temperatures. The high surface free energy available in the pores of the gelled fiber allows for a relatively low-temperature densification. The process provides close control over solution composition and rheology of fiber. The disadvantage is that rather large dimensional changes must be accommodated upon sintering so that fiber integrity is conserved.

An important fiber in this series is **Nextel 720**. It is also a sol-gel processed fiber with the composition 85 % Al_2O_3-15 % SiO_2. The distinctive feature of this fiber is that it has a two-phase crystalline microstructure consisting of globular and elongated grains (100 nm) of α-Al_2O_3 and mullite ($3Al_2O_3 \cdot 2SiO_2$) and large, globular mosaic crystals (0.5 μm) of mullite and α-alumina. The mosaic structure consists of multiple grains having similar crystal orientations and separated by low angle grain boundaries. This microstructure results in much improved creep properties with a creep rate at 1200 °C which is reported by the manufacturer as being three orders of magnitude less than that of the FP-fiber. The final ceramic fiber is obtained by firing at 1350 °C to convert the 85 % alumina + 15 % SiO_2 (amorphous) composition to approximately 59 vol % mullite and 41 vol % Al_2O_3.

With the exception of the Nextel 720, which retains its high temperature properties better, all other alumina based fibers lose their strengths above 1150 °C, which tends to exclude these fibers from most ceramic matrix composites materials [23, 24, 30-32].

There are a variety of non-commercial ceramic fibers that have been produced recently by the sol-gel process. These include fibers of mullite and mullite-zirconia [33], yttrium aluminum garnet (YAG) [16-19, 34], α-Al_2O_3 [18, 34], Al_2O_3-YAG eutectic [18], $MgAl_2O_4$ (spinei) [18], and alumina-baria [35]. Table 2.1 lists properties and compositions of some commercial alumina based fibers.

Liquid Processing

Edge-Defined Film-Fed Growth (EFG)

In the EFG process, a refractory metal die is partially immersed in a crucible containing a melt of the composition to be grown. Liquid from the melt rises in capillaries in the die and wets the upper surface of the die. A seed crystal is touched to the liquid film on the die surface and withdrawn. As it is withdrawn the crystal grows continuously downward toward the liquid film from which it is being pulled. The edge of the die defines the shape of the object being grown. Growth rates as high as 200 mm/min have been attained. A molybdenum or tungsten die is commonly used which must be stable at the melting temperature of the material to be grown. Figure 2.9 shows a schematic of the EFG method.

Fiber type	Manufacturer	Trade Mark	Composition (wt %)	Diameter (μm)	Density (g/cm^3)	Strength (GPa)	Strain to Failure (%)	Young's Modulus (GPa)
	3M	312	62% Al_2O_3 24% SiO_2 14% B_2O_3	10-12 or 8-9	2.7	1.7	1.12	152
	3M	440	70% Al_2O_3 28% SiO_2 2% B_2O_3	10-12	3.05	2.1	1.11	190
	3M	480	70% Al_2O_3 28% SiO_2 2% B_2O_3	10-12	3.05	1.9	0.86	220
	3M	550	73% Al_2O_3 27% SiO_2	10-12	3.03	2.2	0.98	220
	3M	720	85% Al_2O_3 15% SiO_2	12	3.4	2.1	0.81	260

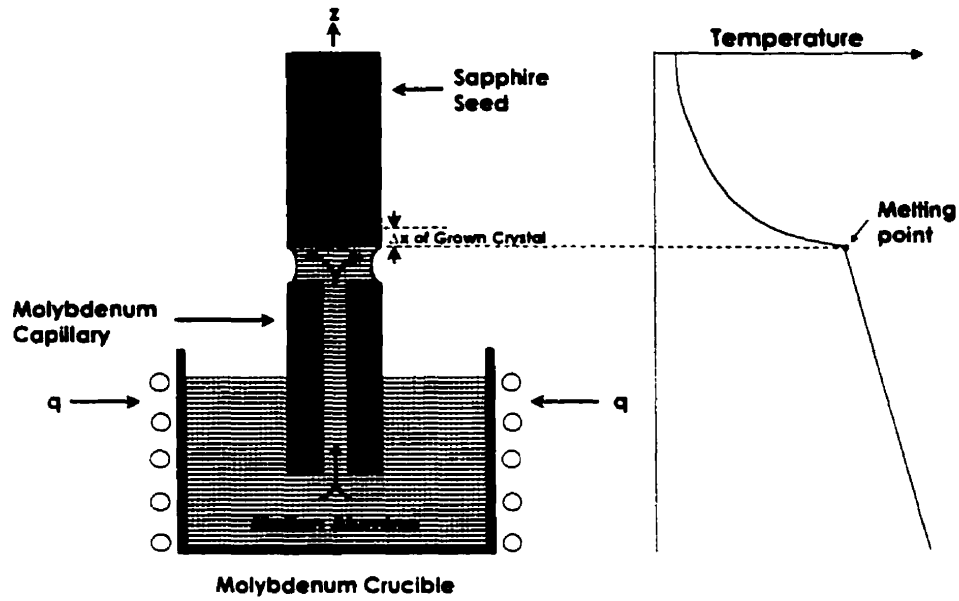

Figure 2.9 Edge-defined film-fed growth (EFG): q represents energy input, z translation of bar.

The EFG technique has been used to make continuous, monocrystalline sapphire (Al_2O_3), as well as continuous fibers of yttrium aluminum garnet (YAG), Al_2O_3-YAG eutectic and Al_2O_3-ZrO_2 eutectic [12, 23, 36, 37].

Laser-Heated Floating Zone (LHFZ)

The LHFZ technique is particularly suited to producing small crystals of virtually any congruently melting compound. Its major advantage over EFG crystal growth is that the purity of the growth crystals is determined solely by the purity of the source material, as there is no crucible involved since this led to contamination problems in the EFG process. Other advantages are that a minimal amount of material is required to determine its suitability for crystal growth; and, since the growing crystal is not enclosed, it is easy

to study the shape of the molten zone and solidification behavior during the growth process. This growth process maximizes the range of host compositions, dopants and atmospheres that can be considered without regard to restrictions which are typical of high-temperature materials experiments, and resulting fibers are free of unwanted impurities.

In general, the LHFZ equipment comprises a CO_2 laser and a growth chamber (Figure 2.10). The laser beam is first attenuated to reduce its power by 98% before being radially dispersed by a conical mirror. The beam is then reflected by a series of planar and parabolic mirrors to focus it to a very fine spot on the tip of the feed material. The power of the laser is increased until a molten pool is formed on the end of the feed material, at which point a seed crystal is dipped into the pool and then withdrawn at a constant rate to form a fiber. The diameters of the growing fibers are established by maintaining equal mass flow rates into and out of the molten zone through the relative insertion and withdrawal rates and the relative densities of the fiber and feed rod. Fiber diameters can be easily reduced to 1/3 of the feed rod diameter under robust, absolutely stable conditions; further diameter reductions are possible under metastable conditions. Absolute zone stability is maintained as long as the zone height does not exceed approximately three times the diameter of the smallest attached solid. The rate at which the feed material is fed into the laser beam and seed crystal is withdrawn determines the overall change in cross-sectional area from the feed material to the seed crystal. As in conventional floating zone process, melts are supported by and contact only a solid feed

rod and a growing crystal having a composition that is in equilibrium with the melt. Growth atmospheres may be selected freely to optimize the growth process and the properties of the resulting fibers.

With the small dimensions involved, gravity has a negligible effect on melt zone shape or stability. Fibers can be pulled in any direction; downward pulling direction minimizes problems with entrapment of bubbles that form in the melts as gases are rejected from solution and with the formation of condensates on the fiber surfaces; these important advantages are not achievable with the EFG process. Crystallographic growth axes are determined simply with preoriented seed crystals. In sequence, the end of the feed rod is melted and stabilized, the seed crystal is attached to the melt, and pulling is initiated after the melt zone has stabilized [24, 36, 38].

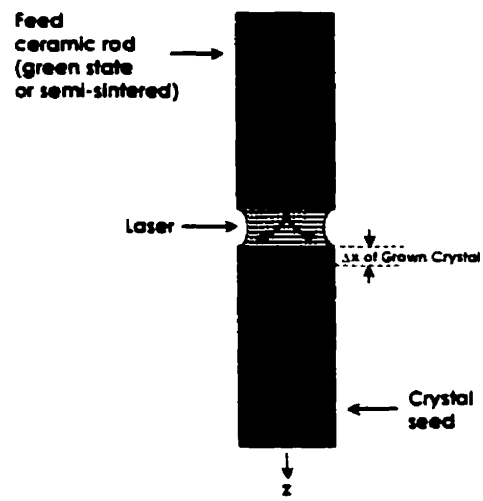

Figure 2.10 Heated-Laser Floating Zone; q represents energy input, z translation of bar.

A laser-heated floating zone method has been devised to make a variety of ceramic fibers. Sigalovsky, Haggerty *et al.* [39-42] used laser heating for crystal growth of $MgAl_2O_4$, Y_2O_3-stabilized cubic ZrO_2, and $ZrO_2(Y_2O_3)$-Al_2O_3 eutectic. Doleman and Butler [14] processed Al_2O_3-YAG eutectic fibers and Sayir *et al.* [43] sapphire fibers by the LHFZ technique.

Continuous monocrystalline filaments have been developed commercially by the Saphikon Company in the USA. These filaments are grown from molten alumina and, as a consequence, are produced at a slow rate, high cost and with large diameters, usually in excess of 100 μm. The near stoichiometric composition of these fibers, with the absence of grain boundaries, ensures that they should be able to better withstand high temperatures above 1600 °C. Careful orientation of the seed crystal enables the crystalline orientation to be controlled so that creep resistance can be optimized. Published data on the strength of Saphikon fibers as a function of temperature reveals that strength variation is not a single function of temperature. The observed fall in strength around 300 °C, which is then followed by an increase in strength around 500 °C, could be due to stress corrosion. These fibers are not without defects and characteristic bubbles can be seen in the fibers most probably due to meniscus at the point of fiber growth and convection in the melt.

The same manufacturing processes have been employed to produce an eutectic fiber consisting of interpenetrating phases of α-alumina and YAG. The structure is

lamellar and oriented parallel to the fiber axis. This fiber does not show the same fall in strength seen with the single phase alumina fiber. However, such fibers are seen to relax from 1100 °C but do not have as strong a dependence on temperature as the polycrystalline oxide fibers [13, 44].

2.3.3 Rapid Solidification Techniques

Inviscid Melt Spinning

Another novel technique of making oxide fibers is called the inviscid melt technique. It is true that, in principle, any material that can be made molten can be drawn into a fibrous shape. Organic polymeric fibers such as nylon, aramid, etc. as well as variety of glasses are routinely converted into a fibrous form by passing a molten material, having an appropriate viscosity, through an orifice. The inviscid (meaning *low viscosity*) melt technique uses this principle, and a schematic of the method is shown in Figure 2.11. Essentially, the technique involves the extrusion of a low viscosity molten jet through an orifice into a chemically reactive environment. The low-viscosity jet is unstable with respect to surface tension because of a phenomenon called Rayleigh waves.

Melt spinning is the latest and lowest-cost fiber fabrication process known. However, the application of the conventional melt spinning technique to ceramics with low melt viscosity, such as alumina, is impossible due to Rayleigh break-up of the ceramic molten stream. Inviscid melt spinning (IMS) has been applied to the production of ceramic fibers of low melt viscosity (< 10 Pa·s). By introduction of a reactive

propane gas, a carbon sheath can be formed at the surface of the molten stream. The carbon sheath can prevent Rayleigh break-up and stabilize the molten stream until solidification occurs.

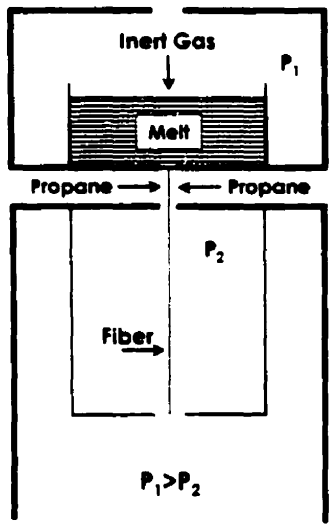

Figure 2.11 Schematic drawing of inviscid melt spinning process.

Chemical Jet Stabilization

Inviscid melt spinning is a dynamic process. The following events may occur concurrently or consecutively: the temperature of the inviscid jet decreases because of radiant and convective cooling; the propane decomposes to give particulate carbon and hydrogen; carbon enters into the surface of the molten jet, creating a carbon-rich skin, and may in part react with the oxide to form carbides and oxycarbides; the jet solidifies, yielding an amorphous or crystalline fiber. Particulate carbon may, but does not always, deposit on the jet surface to form a sheath as the jet (fiber) cools.

Consequently, chemical jet stabilization, which is capable of converting an otherwise unstable jet into a stable jet, might rely on one or more of these mechanisms: (1) formation of a carbon sheath on the surface of the jet and fiber, (2) rapid cooling of the jet due to the endothermic decomposition of propane and/or the endothermic surface reaction between oxide and carbon, and/or (3) an increase of viscosity in the surface of the molten jet through incorporation and/or formation of particulates [24, 45-47].

Alumina-based ceramic fibers Al_2O_3-CaO-MgO (74 wt% Al_2O_3) [48], Al_2O_3-MgO (98.16 wt% Al_2O_3) [49], Al_2O_3-CaO [45, 46], and Al_2O_3-ZrO_2 (57.5 wt% Al_2O_3) [50] have been produced using the IMS method. The melting temperature of alumina was decreased by addition of oxides such as MgO, CaO, and/or ZrO_2. Those IMS fibers were in short crystalline fiber forms, showing some degree of porosity, except for the Al_2O_3-CaO fibers, which were vitreous and void-free as spun.

Melt Extraction

Melt Extraction involves bringing the edge of a spinning disk into contact with a source of molten material. The material solidifies on the disk edge, adheres there briefly, and then is spontaneously released in the form of solid filament, fiber, or powder. When the molten material is contained in a crucible, the process is referred to as Crucible Melt Extraction (CME). When the source of molten material is a droplet formed on the end of a rod of the same material, the process is referred to as Pendant Drop Melt Extraction (PDME).

This technique overcomes some of the problems inherent to melt spinning, such as orifice blocking and instability of the liquid stream. By introducing notches in the edge of the extraction disk, the continuity of the casting is interrupted, and staple fibers may be cast, the length dependent on the notch spacing.

Crucible Melt Extraction (CME)

CME is a process wherein the periphery of a rotating heat-extracting disk is brought into contact with the surface of a source of molten ceramic. As the periphery of the disk passes through the molten ceramic, the ceramic solidifies onto and adheres to the disk. This solidified ceramic is extracted from the melt, still clinging to the disk periphery, and continues to cool. As a result of thermal contraction and centrifugal force, the fiber, in the form of a fiber, is spontaneously thrown free of the disk after a short residence time. The process is shown schematically in Figure 2.12(a).

The important elements of the process are (a) the melting system, (b) the disk drive, (c) the disk geometry and properties, (d) the feed system, and (e) the surface chemistry of the melt.

Pendant Drop Melt Extraction (PDME)

PDME is similar in many respects to CME. That is, disk design, speed ranges, control of fiber shape and length, and collection techniques are similar. The fundamental difference is in the nature of the source of molten material. A sketch of a simple PDME

system is shown in Figure 2.12(b). In PDME, the melt is a droplet supported by its own surface tension on the end of a rod of the same material, or of some other material. The greatest single advantage of this system is the elimination of the crucible. This makes it possible to fiberize high-melting-point materials and highly reactive materials with little difficulty.

Because of the limited supply of material in the droplet, it is easier in PDME to limit the contact of the liquid with the disk periphery, and hence the method lends itself to the production of finer fibers. Fibers with effective diameters in the range 25-125 μm are typical. Because of its relative simplicity, PDME is readily adaptable for operation in vacuum [51-53].

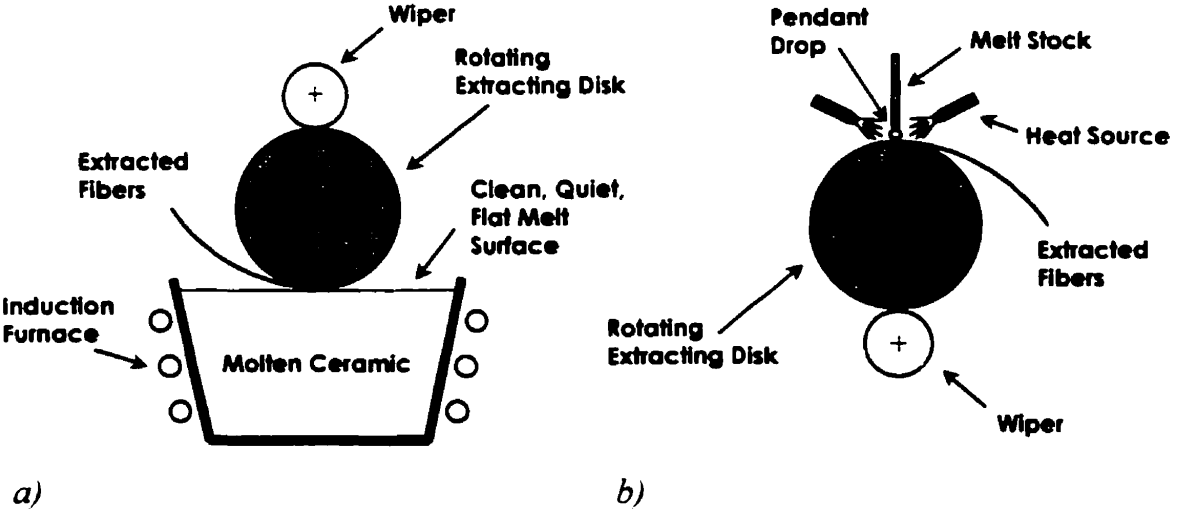

Figure 2.12 Schematic of (a) Crucible Melt Extraction and (b) Pendant Drop Melt Extraction.

PART II. YTTRIA-ALUMINA SYSTEM

Many of the compounds which form within the pseudo-binary system between alumina (Al_2O_3) and yttria (Y_2O_3) have assumed some economic significance in recent years as important components of both electronic and optical devices.

In addition to the two end members of the Al_2O_3-Y_2O_3 system, three intermediate compounds are known to exist. These correspond to the compositions $Y_3Al_5O_{12}$, $YAlO_3$ and $Y_4Al_2O_9$. The nomenclature used to describe these three compounds is somewhat confusing. They are frequently referred to in terms of their crystal structures so that $Y_3Al_5O_{12}$ and $YAlO_3$ become respectively yttrium aluminum garnet and yttrium aluminum perovskite with the acronyms YAG and YAP finding increasing usage. The extension of this nomenclature to $Y_4Al_2O_9$ as yttrium aluminum monoclinic, shortened to YAM, is not entirely self-consistent since the garnet and perovskite terms are derived from geological counterparts and no such equivalent exists for $Y_4Al_2O_9$.

The most self-consistent and understandable terminology would be to use the molecular ratios in conjunction with the shorthand of Y for yttria and A for alumina, as used by ceramists in other oxide systems, the calcia-alumina (C-A) system being a good example. Thus the garnet becomes Y_3A_5 (from $3Y_2O_3 \cdot 5Al_2O_3$); the perovskite becomes YA ($Y_2O_3 \cdot Al_2O_3$) and the monoclinic phase becomes Y_2A ($2Y_2O_3 \cdot Al_2O_3$) in order of increasing yttria concentration [54].

2.4 Major Uses of the Compounds Within the Y_2O_3-Al_2O_3- System

Traditionally, alumina has been used extensively in polycrystalline form as a refractory material with some developments as the major component of alloy systems such as the ceramics Lucalox (Al_2O_3 with MgO additions), utilized as translucent envelopes for sodium vapor lamps, and β alumina (Al_2O_3 with Na_2O additions), which is an ionic conductor [55]. An early use for single-crystal alumina, sometimes doped with small amounts of chromia to make artificial ruby and generally grown by the Verneuil flame fusion process, was a bearing material in small mechanical devices such as watch mechanisms. Undoped single-crystal alumina is also used for its wear resistant properties as the transparent protective cover for some watch faces. The first commercially important use of yttria was as a component of the red phosphors (yttrium vanadate doped with europium) used in cathode ray tubes for color display systems such as television [56]. However, the major impetus towards the increased importance of the Al_2O_3-Y_2O_3 system as a whole has been derived from the contribution made by its constituent compounds towards solid state laser development. Ruby was the material in which solid state laser action was first demonstrated in 1960 with emission in the red region of the visible spectrum at 695 nm [57, 58] and the basic alumina host lattice when doped with Ti^{3+} has recently shown potential as a tunable solid state laser operating between 710 and 912 nm [59]. YAG doped with Nd^{3+} and emitting at 1064 nm was also an early material [60] in this field and has proved to be the most outstanding solid-state laser combination so far, with room temperature operation, and the choice of either continuous wave or pulsed emission. YAP doped with Nd^{3+} [61] was also technically developed to laser standards but

its commercial exploitation has been restricted by the success of YAG. When doped with Tb^{3+}, YAG and substituted derived garnets [62] have also proved to be useful phosphors in the blue-green region of the visible spectrum, and particularly in high brightness cathode ray tubes where extremely rugged phosphors are a prerequisite. In addition to its laser applications, Al_2O_3 has also proved to be an extremely important insulating substrate for the heteroepitaxial deposition of silicon in the very large scale integration (VLSI) of electronic circuits [63].

In all these new uses, except the phosphor applications, the compounds within the Al_2O_3-Y_2O_3 system are required in the form of highly perfect single crystals and are produced by growth from the melt using the Czochralski technique. It is the demonstration that melt growth of single crystals of these compounds is possible which has helped to resolve the enigmas which once existed concerning the extent of compound formation in this refractory system. More recently, a new use of the system has been developed in that YAG and the Al_2O_3-YAG eutectic were found to be potential candidate materials for reinforcement fiber in ceramic and intermetallic matrix composites for structural applications [7, 8, 64].

2.5 The Stability of the Component Phases

2.5.1 The End Components

Little doubt has been expressed about the existence, stability, structure and composition of either alumina or yttria, except for refinements of their melting points,

which are reported from time to time largely because of the difficulty in making accurate measurements at such high temperatures under oxidizing conditions. Both these compounds are stable from their melting points (Al_2O_3, 2050 °C; Y_2O_3, 2440 °C) to room temperature; however yttria undergoes a phase transformation from hexagonal to cubic at 2310 °C. These compounds have been produced as stable single crystals from their own melts, alumina single crystals having been grown by both the Verneuil [65] and Czochralski [66] processes and yttria by gas-laser heated float zoning [67].

2.5.2 The Intermediate Phases

The chronological development of the Al_2O_3-Y_2O_3 phase diagram is illustrated in Figure 2.13, from which it is apparent that the major enigma has concern the existence and stability of YAP. One of the early phase diagrams by Schneider *et al.* [68] established the presence of YAG and YAM over the temperature range 1000-1800 °C but hinted only at the presence of YAP at temperatures above 1800 °C. Both Olds and Otto [69] and Warshaw and Roy [70] were not convinced that YAP was a stable phase and did not include it in their diagrams. Later work by Toropov *et al.* [71] suggested that YAP had very limited stability, being formed peritectically from YAM and liquid at 1875 °C, but decomposing at 1835 °C into YAM and YAG. The first suggestion that YAP was a congruently melting phase came from Mizuno and Noguchi [72] who established a melting point at 1875 °C but again indicated the decomposition reported by Toropov *et al.* [71]. The occurrence of YAP as a stable congruently melting phase was finally established by the melt growth of large single crystals. Such crystals were grown first by Class [73] using

a float-zoning process. Subsequently Czochralski growth was developed for YAP by many other groups, who confirmed that single crystals could be produced which remained stable during cooling to room temperature and within the exacting thermomechanical environment of a laser cavity. Hence single crystal YAP is sufficiently stable for this phase to be included in the Al_2O_3-Y_2O_3 phase diagram and the most recent version, produced by Abell *et al.* [74], is shown in Figure 2.13.

In contrast with YAP, YAM has been shown on all the phase diagrams published for the Al_2O_3-Y_2O_3 system. Several studies also agree that this phase becomes unstable below 1000 °C. The phase melts congruently but whereas those studies on sintered or fused powder samples suggest melting points in the range 2020-2050 °C, a much lower value of 1930 °C was noted by Cockayne and Plant in single–crystal growth studies reported by Abell *et al.* [74].

YAG has always been identified as a stable phase and included in all versions of the phase diagram. It was grown first in single-crystal form by Yoder and Keith [75] using flame fusion Verneuil process and its melting point was estimated to be 2110 ± 70 °C. This has been revised by several groups carrying out either phase studies or single-crystal growth of YAG by the Czochralski technique and a melting point of 1970 °C was established. Even it is the most stable of the three intermediate phases, YAG reveals one enigma in its solidification behavior in that, in some instances, the solidified melts can

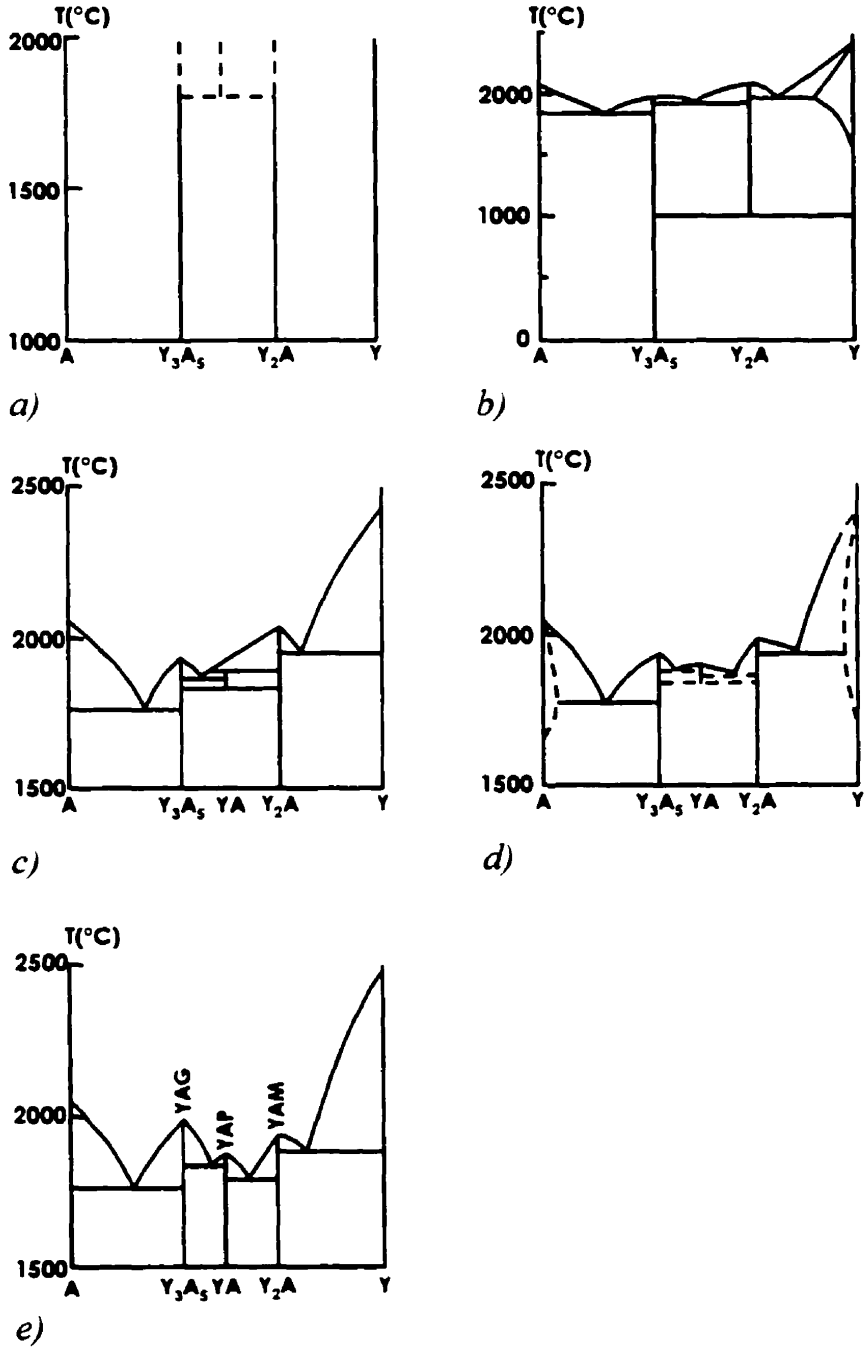

Figure 2.13 Chronological development of the Al_2O_3-Y_2O_3 phase diagram: (a) Schneider *et al.* (1961), (b) Olds and Otto (1961), (c) Toropov *et al.* (1964), (d) Mizuno and Noguchi (1967) and (e) Abell *et al.* (1974).

appear transparent and crystalline and in others ceramic and opaque. Cockayne and Lent [76] showed that this was a feature of the pure YAG melts used in Czochralski growth, in which the solidifying phases can deviate substantially from those predicted by the phase diagram. They showed that melts not artificially nucleated at the YAG melting point could withstand considerable undercooling to 1710 °C. At this temperature crystallization occurs according to a simple eutectic phase system formed between Al_2O_3 and YAP as shown in Figure 2.14. Such material corresponds to the opaque ceramic; whereas the transparent material corresponds to YAG which is nucleated at its melting point. The degree of supercooling which can be exhibited by pure YAG melt establishes that homogeneous nucleation of the garnet phase is difficult. This may well be associated with

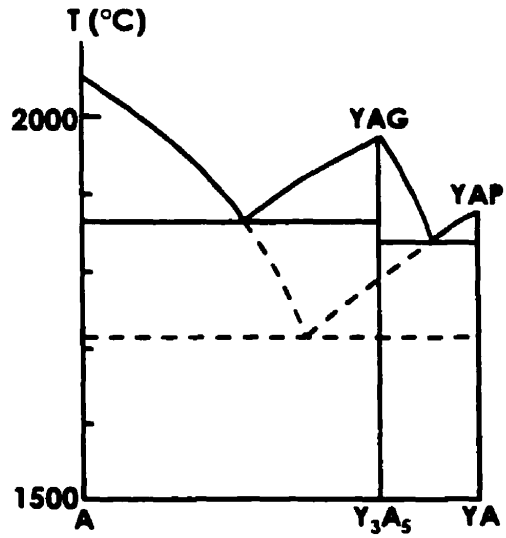

Figure 2.14 The phase relationships in the region Al_2O_3-$YAlO_3$ comparing the solidification behavior of undercooled melts with the established equilibria [76].

the complex crystal structure, containing some 160 atoms in each unit cell, which could pose difficulties for the creation of a nucleus greater than the critical size required for growth. As the undercooling is increased, the viscosity of the fluid increases and mixing by convective flow is decreased. Under such conditions, which may become diffusion limited, the creation of the simpler YAP and Al_2O_3 structures with only 20 atoms and 10 atoms per unit cell respectively could be energetically more favorable.

Caslavsky and Viechnicki [77] reported that YAG melts congruently and is stable to its melting point at 1940 ± 7 °C. YAP (perovskite) melts incongruently with a peritectic at 1916 ± 7 °C and a liquidus at 1934 ± 7 °C. A metastable phase diagram was defined (Figure 2.15) with a metastable eutectic at 1702 ± 7°C, which is in excellent agreement with the temperature published by Cockayne and Lent [76] and 23 mol % Y_2O_3-77 mol % Al_2O_3. YAP formed during metastable solidification transforms to YAG in the presence of Al_2O_3 at 1418 ± 7 °C which is accompanied by a volume change and has an endothermic character.

When melt temperatures do not exceed 1940 °C, the melts of Y_2O_3 and Al_2O_3, ranging in composition from 10 to 45 mol % of Y_2O_3, retain aluminum in four-fold co-ordination; therefore, they obey the crystallization path of the equilibrium phase diagram (solid lines in Figure 2.15). However, at approximately 2000 °C a structural change takes place in the liquid; consequently, melts cooled down from temperatures above 2000 °C, follow the crystallization path of the metastable phase diagram (doted lines in Figure

2.15). The metastability is due to the fact that aluminum prefers the six-co-ordination in the melt, which also explains the difficulty of growing YAG single crystals from melts, since the growth rate is predominantly controlled by the rate of a decrease in the aluminum co-ordination [76].

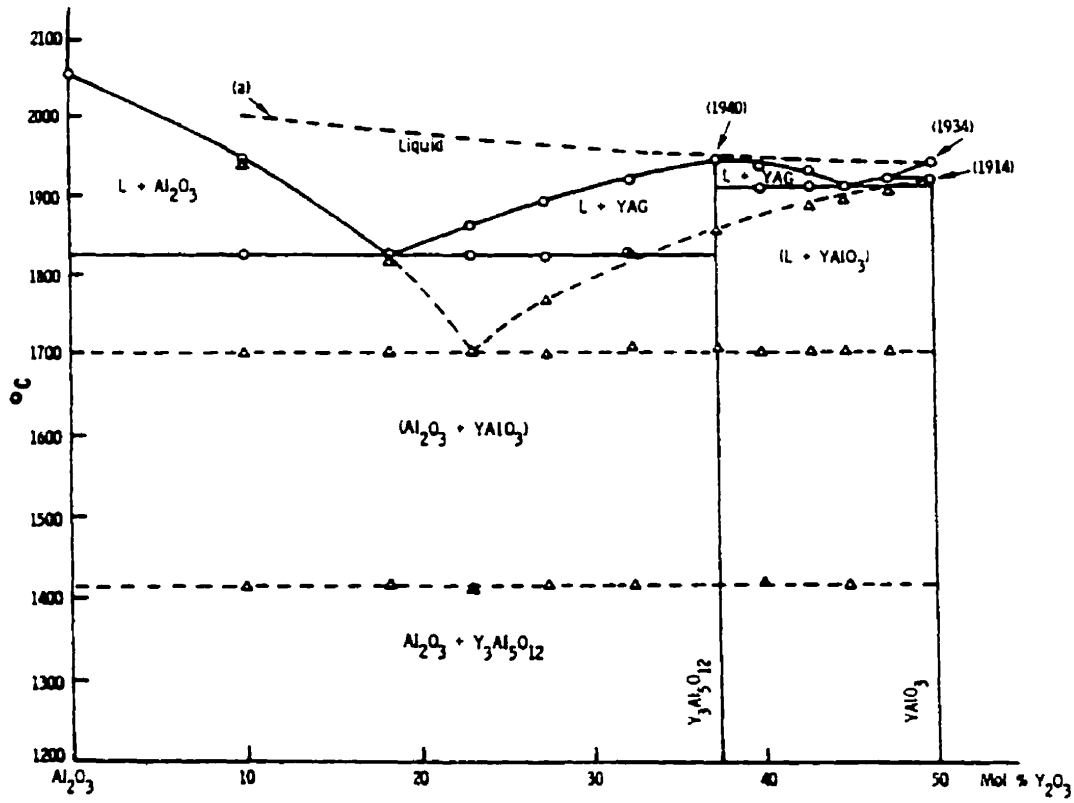

Figure 2.15 Phase diagram of the alumina-rich portion of the Al_2O_3-Y_2O_3 system (Caslavsky and Viechnicki). Equilibrium phase diagram is shown in solid lines; pertinent phase fields are labeled without parentheses. The metastable phase diagram is superimposed with dashed lines and its pertinent phase fields are labeled with parentheses [77].

A more reasonable explanation of the preferential formation of non-equilibrium YAP over the YAG structure seems to lie in the fact that the aluminum has to decrease its co-ordination in order to form the garnet structure. Aluminum-oxygen octahedra are the

most important structural elements in solid and molten structures of aluminum oxide. It is not unreasonable to expect that the solid structure closest to the short-range order of the liquid will be energetically favored and is likely to form whether or not it is stable under the existing equilibrium conditions. As seen from Figure 2.15, YAP (in the composition range 10.0 to 47.5 mol% Y_2O_3) transforms to YAG in the solid state at 1418 °C. This transformation is accompanied by a volume change and has an endothermic character. Both those effects confirm that the YAG structure has a higher energy of formation than the perovskite structure. The higher free energy of the YAG structure results from the necessity to force aluminum into a four-fold co-ordination site to form YAG [77].

Observation of liquids of YAG composition during crystal growth revealed that they are always opaque, in contrast to Al_2O_3 and YAP melts, which are transparent. Formation of two immiscible liquids appeared to be a possible explanation of the opacity. Since the metastable eutectic has been determined between Al_2O_3 and YAP, it was inferred that, after melting, YAG forms two immiscible liquids Al_2O_3 and YAP. This was also confirmed by Aasland and McMillan [78] in a more recent work.

The most recent results by Adylov *et al* [79] corroborated the existence of three compounds in the Y_2O_3-Al_2O_3 system: yttrium aluminum garnet YAG, which forms cubic crystals with a = 1.200 nm and space group I*a*3*d*, the monoaluminate YAP, which forms orthorhombic crystals (orthorhombically deformed perovskite structure) with space group *Pnmd* and the lattice parameters a = 0.5184, b = 0.7368 and c = 0.5317 nm, and the

compound YAM, which forms monoclinic crystals with space group $P2_1/c$ with the lattice parameters a = 0.7368, b = 1.0464, c = 1.1109 nm and β = 108.6°. All three compounds are congruent, and stable at the temperatures studied (above 1200 °C).

The crystallization temperature of Al_2O_3 is 2050 °C, and that of Y_2O_3 is 2440 °C, the temperature of the *hexagonal to cubic* transformation of yttrium oxide is 2310 °C. The crystallization temperatures of the yttrium aluminates are 1942 °C (YAG), 1917 °C (YAP), and 1977 °C (YAM).

The liquidus of the system is characterized by four eutectic points, at 1820 °C (21 mole % Y_2O_3), 1905 °C (42.5 mole % Y_2O_3), 1910 °C (57 mole % Y_2O_3), and 1967 °C (71 mole % Y_2O_3), and a peritectic point at 2310 °C (95 mole % Y_2O_3). The results were used to construct the equilibrium diagram of the Y_2O_3-Al_2O_3 system (Figure 2.16).

Relevant properties for the end components are summarized with those for the intermediate phases in Table 2.2.

In later works, Jin and Chen [80] and Gröbner *et al.* [81] presented thermodynamic calculations of the system using the available phase diagram and thermodynamic data. The results from both calculations are rather similar, and indicate that all three aluminates melt congruently (in the range from 1930 to 2030 °C) and are stable down to ambient temperature. This does not agree with a recent investigation of the melting behavior of

YAP, which gave strong experimental evidence for incongruent melting of this compound at 1875 °C [82]. Recently, a reversible phase transition of YAM at around 1377 °C has been reported [83, 84].

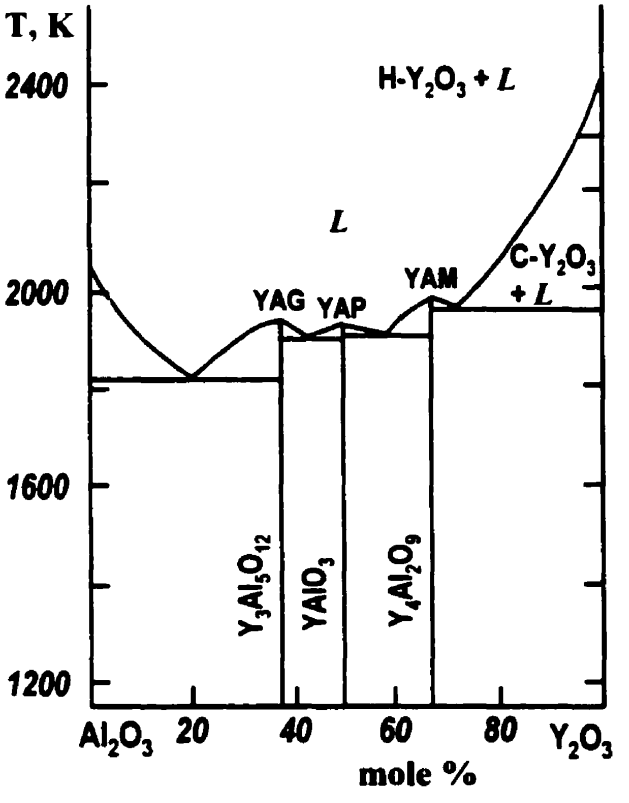

Figure 2.16 Equilibrium phase diagram of the Y_2O_3-Al_2O_3 system (Adylov *et al.*) [79].

Despite the large amount of experimental work performed on this system, there still are some discrepancies concerning the melting and crystallization behavior of YAP and YAG, the composition and the temperature of specific eutectics, the liquidus data on the Y_2O_3-rich side, and the thermodynamic stability of YAP at lower temperatures. Some workers assume that YAP decomposes at temperatures < 1800-1400 °C to form YAM

and YAG, whereas the majority of researchers suggest YAP to be stable from its melting point down to ambient temperature [85].

Table 2.2 Composition, melting point, stability and structure of the phases in the Al_2O_3-Y_2O_3 system.

Chemical Composition	Melting Point (°C)	Stability range	Structure of room temperature phase
Al_2O_3	2050	Melting point to room temperature	Hexagonal
$Y_3Al_5O_{12}$ (YAG)	1942	Melting point to room temperature	Cubic (garnet)
$YAlO_3$ (YAP)	1917	Melting point to room temperature	Orthorhombic (perovskite)
$Y_4Al_2O_9$ (YAM)	1977	Melting point to 1000 °C	Monoclinic
Y_2O_3	2440	Melting point to room temperature hex ↔ cubic transformation at 2310 °C	Cubic

PART III. FUNDAMENTALS OF GLASS FORMATION AND CRYSTALLIZATION

A non-crystalline solid phase represents the ultimate state of solid metastability and may be formed by a number of different routes, including solidification from the liquid or vapor states, deposition from a chemical solution or an electrolyte and by high-

energy ion- or neutron-bombardment of crystalline materials. A non-crystalline solid formed by continuous cooling from the liquid state is known as a glass in the original sense of the word. The vitrification of a melt requires that it be cooled at a rate sufficiently high to avoid a significant degree of crystallization, so that the 'disordered' atomic configuration of the liquid state is frozen-in, or at least largely so. Glass formation occurs easily in some familiar classes of non-metallic material such as silicates and organic polymers. In these, the nature of the bonding places severe limits on the rate at which the atomic or molecular rearrangements, necessary for maintaining thermodynamic equilibrium during cooling can occur; thus the melt solidifies to a glass, even at low rates of cooling often less than 10^2 K/s. In contrast, in metallic and ceramic oxides melts, that have non-directional bonding, the atomic rearrangements occur very rapidly, even a high degrees of undercooling below their equilibrium freezing temperatures. Hence, very high cooling rates (> 10^5 K/s) must generally be imposed to form glasses.

2.6 Undercooling of the Melt and Glass Formation

The basic effect of applying rapid cooling to ceramics is analogous to that for metals. It suppresses diffusion within the material and thus inhibits the attainment of equilibrium phases and microstructures which are characteristics of "slowly" cooled materials. Thus, the expected effects from rapid solidification of ceramics are also similar to metals, namely:

(i) Grain size decreases with increasing solidification rate.

(ii) Increased chemical homogeneity (optimization) with increasing solidification rate.

(iii) Extension of solid solubility with increasing solidification rate.

(iv) Metastable crystal structures.

(v) "Complete" suppression of crystallization to produce noncrystalline, amorphous or vitreous (glassy) ceramics [86].

When a metal or alloy melts, the three dimensional lattice arrangement of atoms, that is, the long-range order, is destroyed and, in the liquid, the atoms vibrate about positions that are constantly and rapidly interdiffusing. During melting, the crystal and liquid phases are in equilibrium and, for pure metals, the volume, enthalpy and entropy undergo discontinuous change; the enthalpy and entropy increase, and the volume usually does also, except where the atomic packing in the crystal is relatively open, as for metalloids. A liquid, at temperatures above the melting point, is in a state of internal equilibrium and its structure and properties are independent of its thermal history. It is characterized by inability to resist a shear stress. Metallic and ceramic oxides liquids have high fluidity because of the non-directional nature of the metallic and ionic bond, respectively, while, in contrast, molten silicates, borates and similar substances, in which the atomic bonding is strongly covalent, are characterized by very low fluidity or, conversely, high viscosity.

Melts of metals as well as ceramic oxides have low viscosities. All solidify at a sharp and well-defined melting point. These melts are inviscid above the melt temperature and their viscosities are comparable to that of motor oil at room temperature, i.e., < 0.16 Pa·s.

On cooling, a liquid must undercool below the equilibrium crystallization temperature before crystallization can begin because of the existence of an energy barrier to the formation of nuclei. The degree of undercooling depends on several factors, including the initial viscosity of the liquid, the rate at which the viscosity increases with decreasing temperature, the temperature dependence of the free energy difference between the undercooled liquid and the crystal phase, the interfacial energy between melt and crystal, the volume density and the efficiency of heterogeneous nucleating particles and the imposed cooling rate. If the liquid is cooled rapidly by heat removal to a sink, the influence of heterogeneous nucleants is increasingly delayed for kinetics reasons and, as the cooling rate is increased, the undercooling is enhanced and recalescence decreased. Thus, the temperature range over which crystallization proceeds becomes increasingly depressed, leading to structural modifications; this then leads initially to the refinement of microstructural features. For alloys, depending on the compositions, an extension of solute solubility and the formation of metastable crystalline phases occur. Eventually, when the cooling rate is sufficiently high, crystallization is suppressed because of insufficient time for significant growth or, in the extreme, for nucleation. In this case, the shear viscosity of the melt η increases continuously, as shown in Figure 2.17.

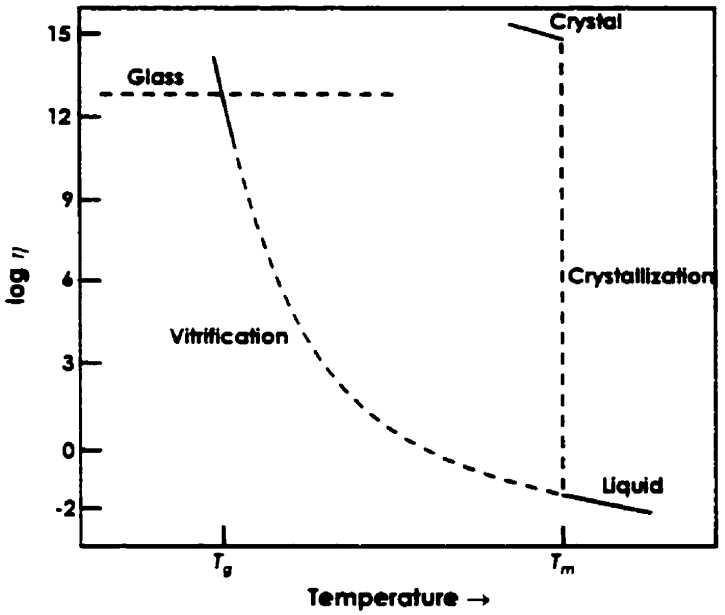

Figure 2.17 Viscosity (η)-temperature (T) behavior corresponding to crystallization and vitrification of a metallic melt.

Although the driving force for nucleation is continually increasing, this is opposed by the rapidly decreasing atomic mobility which, at very high undercoolings, dominates. Eventually, the atomic configuration of the liquid departs from equilibrium and then shortly after that becomes homogeneously frozen in, at the so-called glass transition temperature T_g. This structural freezing to the glass state is, by convention, considered to occur when η is about 10^{13} poise. However, in practice, there is no unique glass structure for a given material since the temperature and structure, at which departure from configurational equilibrium occurs, depends on the cooling rate. Thus T_g and the glass structure are both cooling-rate dependent, the variation in the latter manifesting itself in different structural relaxation behavior during subsequent annealing of the glass. At T_g,

the temperature dependence of the volume and of the enthalpy decrease discontinuously, the marked decrease in specific heat C_p reflecting the fewer degrees of freedom resulting from the freezing of the structure (Figure 2.18). Whereas the difference, ΔC_p, in the specific heat of the undercooled liquid and the crystalline state increases with falling temperature, it becomes very small once vitrification has taken place. On the free volume model of atomic transport, the glass transition corresponds to the elimination of most of the free volume.

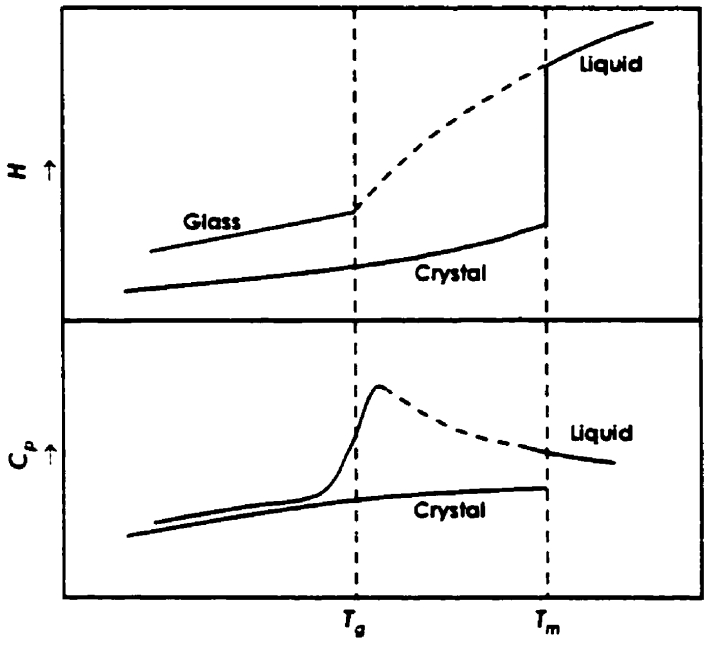

Figure 2.18 Temperature dependence of the enthalpy H and the specific heat C_p corresponding to crystallization and vitrification of a metallic melt.

The process of vitrifying a liquid is, therefore, strictly, one of avoiding the nucleation of crystals during cooling, although a more practical definition would be the avoidance of a just detectable fraction of crystal. The glass forming ability of a material is

then determined by the kinetics of the nucleation process and, for practical purposes, of the early stages of crystal growth.

2.7 Crystallization

A glass is defined as any solid formed by the continuous cooling of a liquid such that detectable crystallization is avoided. This is possible to illustrated simply by referring to Figure 2.19, which shows schematically, as a function of temperature, the time taken for a small amount of crystallinity to form in an undercooled melt. An essential feature of this (TTT) diagram is that as the liquid is undercooled below T_m (the equilibrium melting point), the crystallization rate does not continue to rise indefinitely but reaches a maximum at a temperature T_n. Consequently if the liquid is quenched from above T_m to well below T_n in a time less than t_{min}, the minimum time for crystallization, the undercooled liquid is retained and, at T_g, the glass transition temperature, the configuration is frozen to form a glass. For metallic alloys and ceramic oxides systems, this requires a cooling rate of between 10^2 to 10^{10} K/s. It also follows from Figure 2.19 that if the glass is subsequently heated to a temperature $T < T_n$ and held isothermally for a time t_x it will begin to crystallize. Alternatively if the glass is heated slowly from room temperature, crystallization begins at a temperature, T_x, which increases with increasing heating rate. If it were possible to heat sufficiently quickly to pass the nose of the diagram, crystallization could be totally prevented. The ease with which this devitrification occurs varies widely between different glassy systems. The familiar oxide glasses transform so sluggishly that extreme measures (such as the deliberate introduction

of nuclei) are often needed to induce crystallization even at T_n; on the other hand, metallic glasses transform so rapidly that is rarely possible to heat them much above $0.5T_m$ before spontaneous crystallization occurs.

It should be clear from Figure 2.19 that, unlike melting and other changes of state, crystallization of a glass does not occur at a unique temperature; rather, given sufficient time, devitrification can occur at any temperature, though the time-temperature relationship is such that even most metallic glasses can be considered as stable indefinitely at room temperature; a similar behavior can be assumed for glass ceramic oxides.

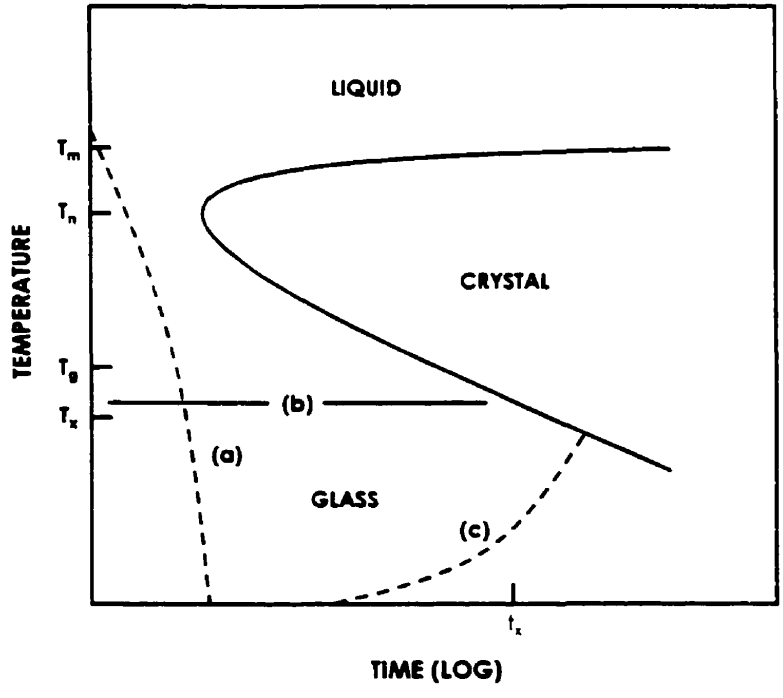

Figure 2.19 Schematic TTT diagram for crystal growth in an undercooled melt, illustrating (a) fast cooling to form a glass, (b) isothermal heat treatment of the glass giving crystallization at time t_x, and (c) slow heating of the glass producing crystallization at T_x.

In practice, the above description is over simplistic in two respects. In the first place a single isothermal transformation diagram has been used to describe both isothermal and dynamic heat treatments whereas an accurate description of the latter requires either continuous cooling (CCT) or continuous heating (CHT) transformation diagrams. However, the only difference to the isothermal diagram is a shift of the transformation to longer times at a given temperature. Secondly, only one potential crystallization product has been considered. There are a number of possible crystallization reactions, each of which should be represented on the transformation diagrams. Figure 2.20 illustrates one possibility. Just below T_m, the undercooled liquid

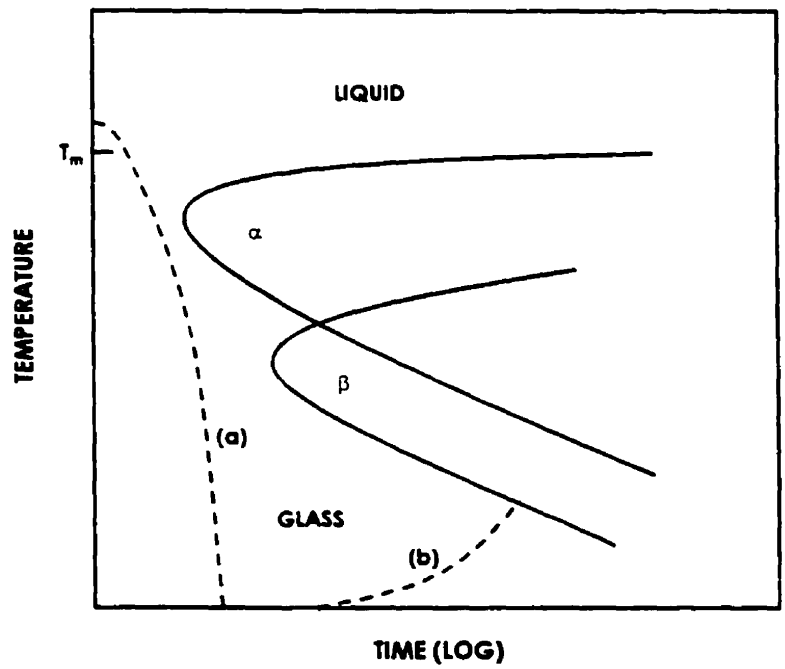

Figure 2.20 Modification of the TTT diagram of Figure 2.19 to show equilibrium (α) and non-equilibrium (β) phases. (a) During rapid quenching to form a glass, crystallization of α must be avoided; (b) heat treatment of the glass generally produces β.

crystallizes to the equilibrium phase, α, whilst at a lower temperatures a second, metastable β phase can form. Most metallic glasses crystallize initially to one or more metastable phases. An important consequence of this is a non-dependence of the kinetics of crystallization (in this case of β) on those of glass formation (i.e. avoidance of α).

Crystallization of metallic glasses occurs by a nucleation and growth process identical to that in liquids just below the melting point, and as such offers a unique opportunity to study under controlled conditions the growth of crystals into an isotropic medium and to test the applicability of classical nucleation and growth theories at large undercoolings [87].

2.7.1 Heterogeneous Nucleation

It was shown that below the equilibrium melting temperature a temperature interval exists, referred to as the metastable zone, in which nuclei do not form at a detectable rate. In this zone, however, crystals can grow if nuclei are provided, i.e. if the melt is "seeded" or "inoculated". At temperatures below this region the crystallization process is controlled by two factors: the rate of formation of nuclei and the crystal growth rate. Melts which increase rapidly in viscosity during cooling, such as those which can form glasses, show maxima in nucleation and crystal growth rates because at the lower temperatures the high viscosity hinders the atomic rearrangements and diffusion processes which are necessary for nucleation and crystal growth. Consequently, curves

for nucleation rate and crystal growth rate for a viscous melt have the form shown in Figure 2.21.

It is evident from this figure that if the aim is to produce the largest possible number of small crystals, nucleation should occur at or near to the temperature at which the maximum nucleation rate occurs. Selection of the optimum nucleation temperature is important in the production of glass-ceramics.

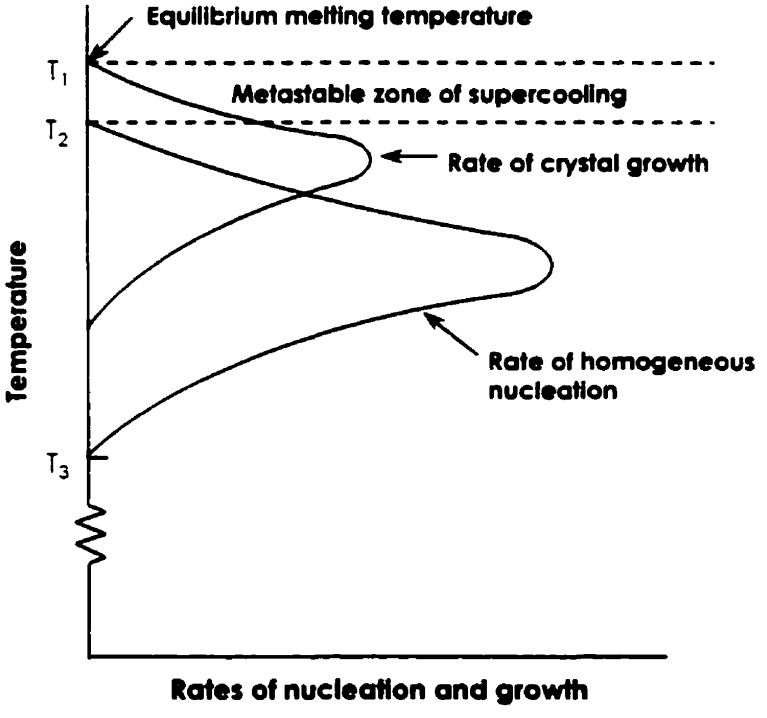

Figure 2.21 Rates of homogeneous nucleation and crystal growth in a viscous liquid.

The metastable zone of supercooling (T_1 - T_2) below the equilibrium melting temperature occurs because the very tiny crystal nuclei have melting temperatures

appreciably below that of the bulk material. From Figure 2.21 it will be noted that there also exists a temperature T_3, below which the homogeneous nucleation rate is zero due to high viscosity of the melt.

In order to form a new phase (the nuclei) within the mother phase, an increase in free energy of the system must occur and this constitutes a barrier to nucleation. There are two contributions to the change of free energy that occurs on nucleation. First, the formation of a boundary or surface between the embryo and the mother phase results in a gain of free energy due to the interfacial energy. Secondly, since the arrangement of the atoms within the embryo will be less disordered than that in the surrounding phase, there will be a reduction in free energy of the system.

The effect of pre-existing surfaces in a supersaturated solution or a supercooled melt is to reduce the value of ΔF^*, the free energy for homogeneous nucleation, by decreasing the value of Δf_s, the interface energy which appears in Equation 2.1.

$$\Delta F^* = 16\pi(\Delta f_s)^3 / 3(\Delta f_v)^2 \qquad (2.1)$$

where Δf_v is the change of free energy per unit volume resulting from transformation from one phase to the other and Δf_s is the energy per unit area of surface between the two phases; Δf_s can be equated with σ, the interface tension.

The volume free energy change Δf_v between the liquid phase and the crystal phase is not altered by heterogeneous nucleation and neither is the activation energy for

diffusion, Q. The important feature of heterogeneous nucleation is that the interfacial tension between the heterogeneity and the nucleated phase must be low. Therefore the influence of the catalyzing surface is determined by the contact angle θ at the substrate-melt-precipitate junction. The activation energy of heterogeneous nucleation can be expressed as:

$$\Delta F_c^* = \Delta F^* f(\theta). \tag{2.2}$$

Turnbull and Vonnegut (1952) modified the equation for homogeneous nucleation rate ($I = A\exp(-\Delta F^*/kT)$) to give an expression for heterogeneous nucleation rate:

$$I_c = A^1 \exp\left[-\Delta F^* f(\theta)/kT\right] \tag{2.3}$$

and if the activation energy for diffusion is included, as suggested by Stokey (1959a), the equation becomes:

$$I_c = A^1 \exp\left[-\left(\Delta F^* f(\theta) + Q\right)/kT\right]. \tag{2.4}$$

Thus heterogeneous nucleation can be described in terms of the parameters which describe homogeneous nucleation and a single additional parameter, θ, where the term $f(\theta)$ is given by:

$$f(\theta) = (2+\cos\theta)(1-\cos\theta)^2/4 \tag{2.5}$$

If the nucleus has the form of a spherical cap on the heterogeneity; the latter is assumed large compared with the nucleus. The angle θ is determined by the balance of surface tensions:

$$\sigma_{HL} = \sigma_{SH} + \sigma_{SL}\cos\theta \tag{2.6}$$

where:

σ_{HL} is the interfacial free energy (tension) between the heterogeneity and the melt,

σ_{SH} is the interfacial free energy between the heterogeneity and primary crystal phase,

σ_{SL} is the interfacial free energy between the crystal phase and the melt.

For any contact angle (θ) less than 180°, the free energy barrier is less for nucleus formation on the surface of the heterogeneity than for homogeneous nucleation. As a result, heterogeneous nucleation will occur wherever possible in preference to homogeneous nucleation.

The presence of heterogeneities that have the effect of reducing ΔF^*, will also reduce the incubation time τ. For heterogeneous nucleation the incubation time τ_H is given by

$$\tau_H = \tau f(\theta) \tag{2.7}$$

where τ is the incubation time for the "pure' glass, and $f(\theta)$ is given by:

$$f(\theta) = (1 - \cos\theta/2) - (\cos^2 \theta/2). \tag{2.8}$$

With increasing efficiency of the nucleating particle, the incubation time is reduced and the potency of a nucleation catalyst can be expressed as τ/τ_H.

2.7.2 Crystal Growth

The controlled crystallization of glasses involves crystal growth as well as nucleation. While the latter process is highly critical to the production of microscrytalline

glass-ceramics, the growth process is also of considerable importance in determining the morphology of the material produced.

Crystal growth is dependent upon two factors:

(i) The rate at which the irregular glass structure can be re-arranged into the periodic lattice of the growing crystal;

(ii) The rate at which energy released in the phase transformation process can be eliminated, that is: the rate of heat flow away from the crystal-glass interface.

Considering first the process of structural transformation: an atom in the crystal structure has a lower free energy than a corresponding atom in the glass phase by an amount ΔG, the bulk free energy of crystallization. Also, for an atom to cross the interface between the glass and crystal phases it must overcome an energy barrier corresponding to a free energy of activation, $\Delta G''$.

Thus an expression for crystal growth rate, U, can be derived:

$$U = a_0 \nu \exp[-\Delta G''/RT][1 - \exp \Delta G/RT] \qquad (2.9)$$

where a_0 is the interatomic separation and ν is the vibrational frequency at the crystal-glass interface.

However, growth generally takes place by mechanism in which it is energetically favorable for atoms to be added to step sites provided by screw dislocations intersecting

the interface. Thus only a fraction of the total number of sites is available for growth; this fraction is given by:

$$f \approx \Delta t / 2\pi T_m \,. \tag{2.10}$$

It is necessary therefore for the right-hand side of Equation 2.9 to be multiplied by this factor.

Returning to Equation 2.9, a further expression can be derived as follows. The diffusion coefficient, D, is given by:

$$D = a_0^2 \nu \exp[-\Delta G''/RT] \tag{2.11}$$

and also,

$$D = RT/3\pi N \eta a_0 \tag{2.12}$$

Substituting these and introducing the factor f we have

$$U = fRT[1 - \exp \Delta G/RT]/3\pi N a_0^2 \eta \,. \tag{2.13}$$

This expression makes clear the marked effect of change of viscosity (η) in modifying crystal growth rates in glasses. Thus although the growth rate increases at first as the melt is cooled below the liquidus temperature, the rapid increase of viscosity soon exerts a dominating influence causing the growth rate to fall and leading to the typical growth rate curve (Figure 2.21) [88].

As pointed out earlier, in some cases a further factor controlling crystal growth rate may be the rate at which heat can flow away from the growing crystal. This situation occurs when the rate of heat flow is insufficient to prevent an increase of the temperature of the crystal-liquid interface to a value which will cause a reduction of growth rate. In general two factors are important: Δhf the molar heat of crystallization and the thermal diffusivity of the liquid surrounding the crystal.

The heat flux J created during crystallization is:

$$J = UA\rho\Delta Hf/M \tag{2.14}$$

where U is the linear growth rate, A is the interfacial area, ρ is the density, and M is the molecular weight.

Also, the heat flux is proportional to the temperature gradient,

$$J = AkdT/dx \tag{2.15}$$

where k is the thermal conductivity.

Hence,

$$dT/dx = UP\Delta Hf/Mk \tag{2.16}$$

In certain glass-ceramic systems crystal growth rates as high as 10 μm/sec are observed, and here the temperature gradients at the crystal glass interface may be sufficient to have an effect upon crystal growth rates.

CHAPTER 3

EXPERIMENTAL PROCEDURE

3.1 Starting Materials

Aluminum oxide (A17, Alcoa Industrial Chemical Division) with 99.5% purity and yttrium oxide (Grade 5600, Union Molycorp) with 99.99% purity were used as starting materials (Table 3.1).

Table 3.1 Particle size and chemical composition of starting materials.

	Aluminum oxide, Al_2O_3		**Yttrium oxide, Y_2O_3**	
Particle size, μm [1]	3.0-3.5		4.0-5.0	
Chemical composition	Al_2O_3, %	99.5	Y_2O_3, %	99.99
	SiO_2, (max)	0.02 (0.04)	CaO ppm	< 2
	Fe_2O_3, (max)	0.01 (0.03)	SiO_2	< 25
	Na_2O, (max)	0.08 (0.10)	Fe_2O_3	< 1
			Na_2O	< 1
			La_2O_3	2
			Nd_2O_3	4
			Dy_2O_3	2
			CeO_2	< 1

1. Medium micrometer, by sedigraph.

Figure 3.1 shows SEM micrographs for Al_2O_3 and Y_2O_3 powders. It can be seen that large Al_2O_3 particles contain fine agglomerates on their surface. which does not occur for Y_2O_3 angular shape particles.

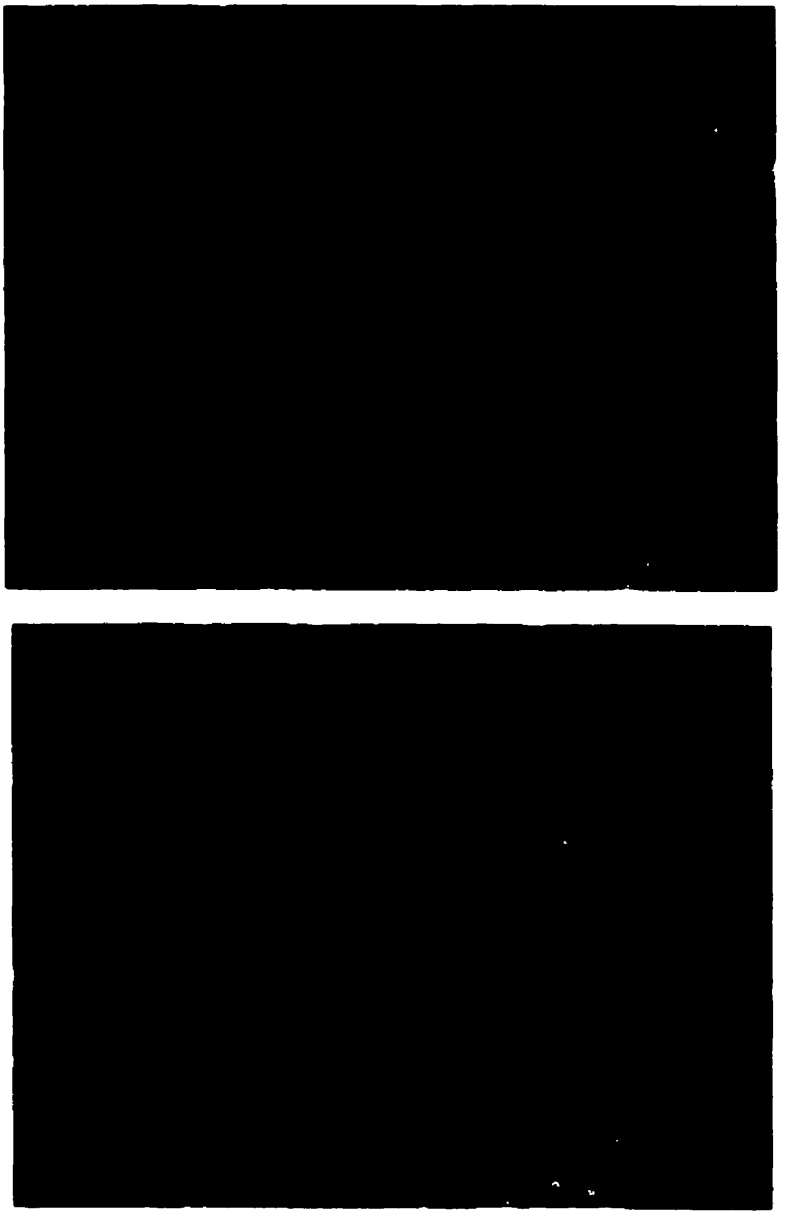

Figure 3.1 SEM micrographs for starting materials: (a) Al_2O_3 powder and (b) Y_2O_3 powder.

3.2 Rod Fabrication

In this study the terms YAG, YAP and YAM will be used to refer to the crystalline compounds, but the molecular ratios, i.e. Y_3A_5, YA and Y_2A, will be used when discussing the chemical composition of the starting material.

Several compositions may be melt-extracted in the Al_2O_3-Y_2O_3 system, however compositions of interest are those based on the alumina-rich section of the phase diagram (Fig. 3.2). Three different compositions were investigated: Al_2O_3-Y_3A_5 eutectic (E1), Y_3A_5 (pure YAG), and Y_3A_5-YA eutectic (E2). The stoichiometric amounts were mixed and attrition milled for 2 h using alumina balls and water as media and fluid, respectively (Table 3.2). The resultant slurry was dried for 20 min in a microwave oven. The 3-mm-diameter ceramic rods were made by extrusion of the ceramic powder using water, and 8 % of hydroxypropyl cellulose as a plasticizer, and dried for 24 h in air. They were then fired at 1500 °C for 1 hour prior to their use for melt extraction.

Table 3.2 Chemical compositions and approximate melting temperatures of the mixtures studied.

Compound	Al_2O_3 wt % (mol %)	Y_2O_3 wt % (mol %)	Melting point °C
E1	62.9 (79.0)	37.1 (21.0)	1820
Y_3A_5	43.0 (62.5)	57.0 (37.5)	1942
E2	37.9 (57.5)	62.1 (42.5)	1905

E1: Al_2O_3-Y_3A_5 eutectic, E2: Y_3A_5-YA eutectic.

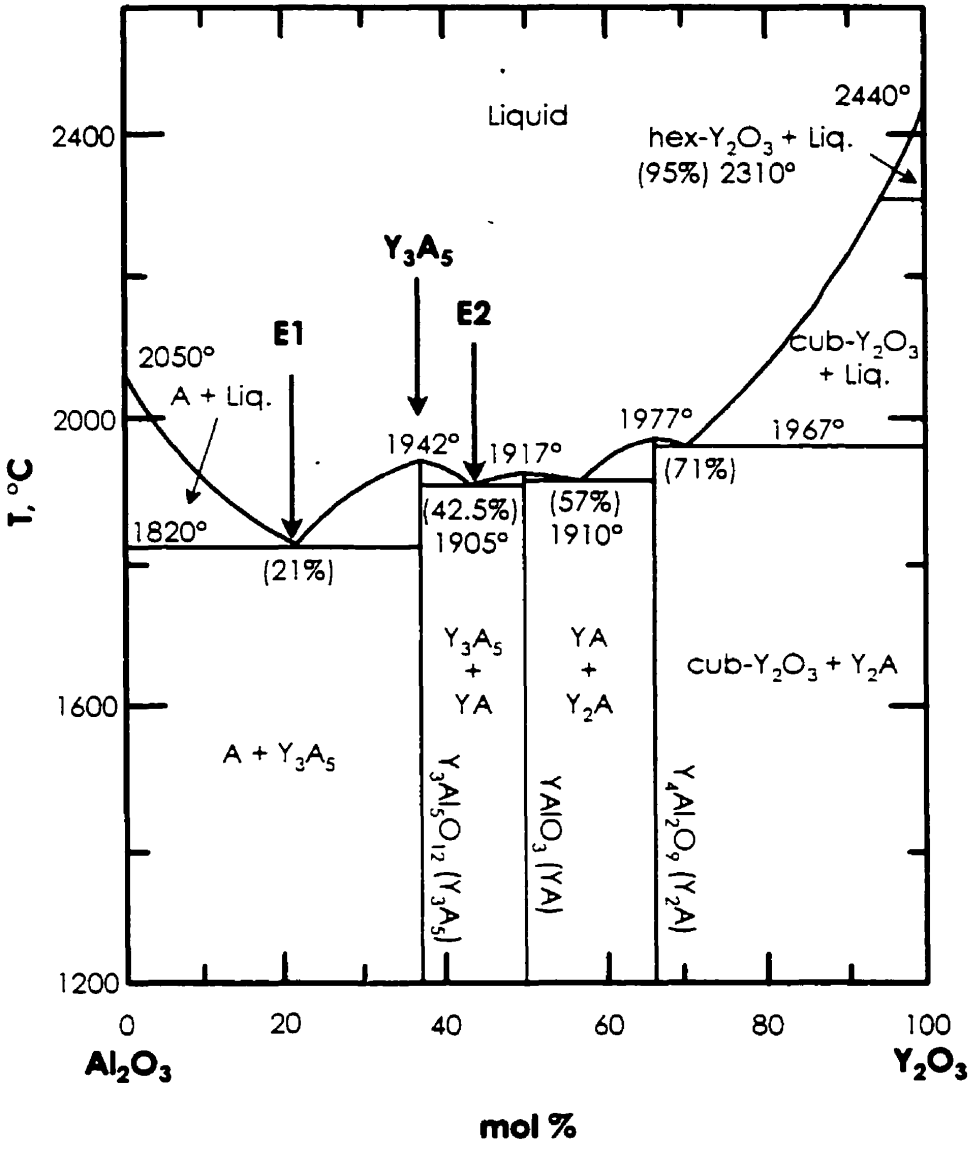

Figure 3.2 Al_2O_3-Y_2O_3 phase diagram [79, 89].

The flowchart of the fiber processing is shown in Figure 3.3.

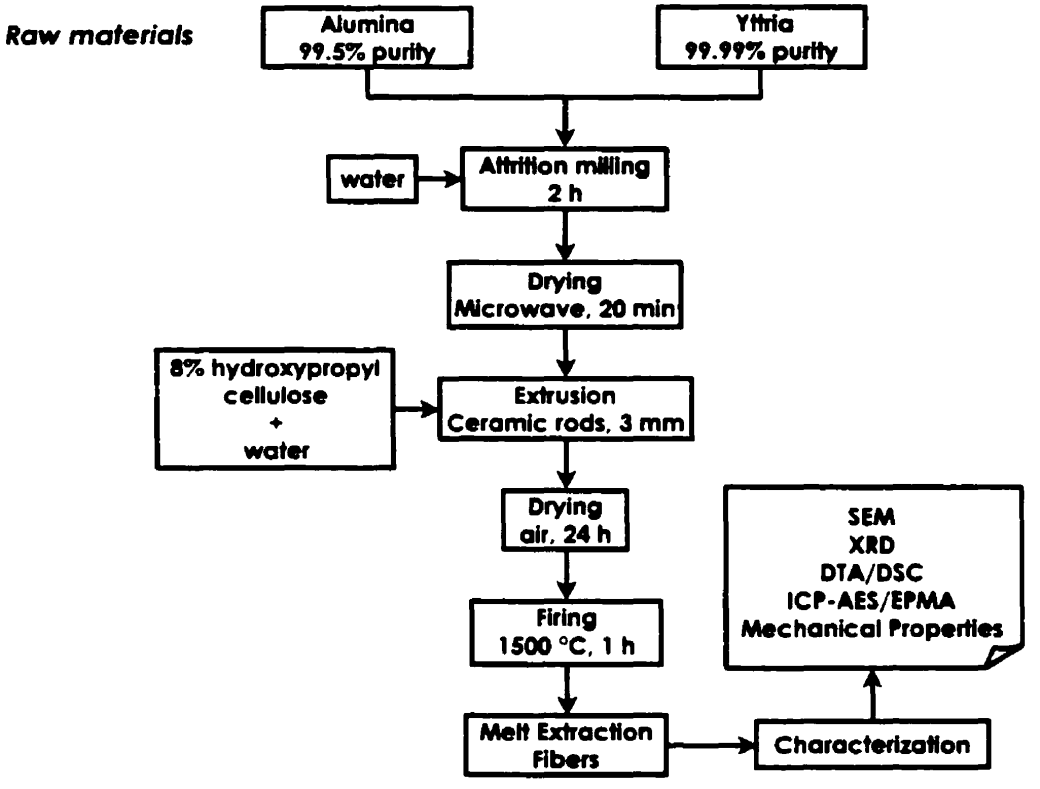

Figure 3.3 Fiber processing flowchart.

3.3 Fiber Extraction

Fabrication of fine oxide ceramic fibers using a melt extraction system is a novel technique developed at McGill University [90-92]. This system is a combination of the Crucible Melt Extraction and Pendant Drop Melt Extraction processes that makes it feasible to melt and extract a small volume of high melting temperature, inviscid oxide ceramic in a controlled and reproducible fashion.

The schematic of the melt extraction system is shown in Figure 3.4. The extraction wheel is a sharpened 14.5-cm-diameter copper-beryllium-alloy disk (alloy C17510). Copper was chosen because of its high thermal conductivity necessary to extract the heat from the liquid and to promote rapid solidification. The oxy-acetylene torch was used as a heat source and boron nitride only acted as a guide for the ceramic rods since the molten drop is self-contained by surface tension.

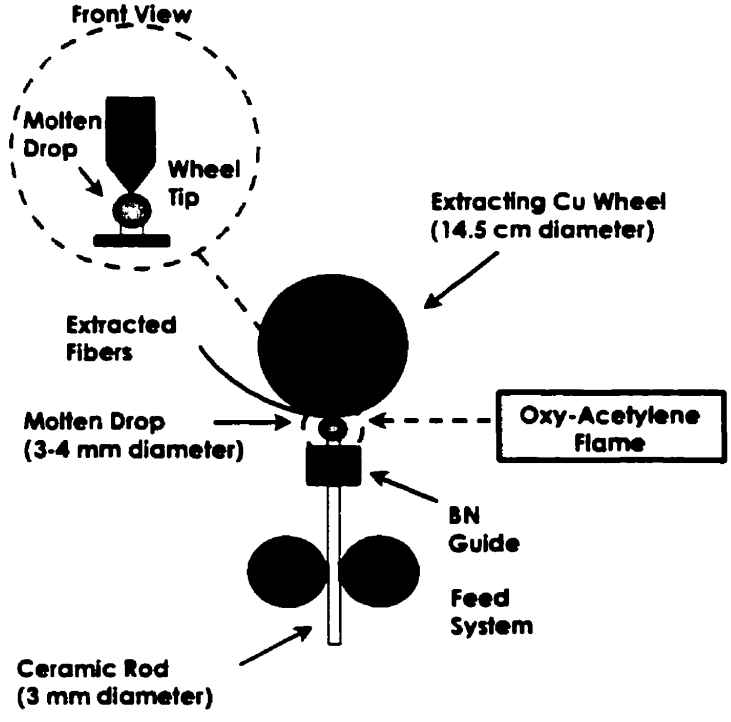

Figure 3.4 Schematic diagram of the melt extraction system.

Prior to the extraction, a ceramic rod is melted with the oxyacetylene flame to form a small drop just beneath the wheel tip. Using the oxyacetylene heating, the temperature of the molten drop is ~ 2000 °C. The droplet is then slowly pushed towards the rotating wheel to

provide a fine contact between the wheel tip and molten drop. Upon contact with the wheel, the fibers form and rapidly solidify.

The sharp tip is an essential feature of the method and permits continuous casting of high quality fibers below 30 μm diameter. The molten drop is generally quite stable once accessed by the wheel, and the rod may be steadily fed onto the wheel to replace the material being extracted. For melt extraction of ceramics, a thin feed rod is used so that surface tension alone provides a sufficiently fine droplet. The rate of feed and the tangential velocity of the wheel determine, within the limits, the diameter of the fiber. It should be stressed that, although the fabrication process is continuous, the fibers as a rule are not. Small defects on the wheel, particles of oxide and other contaminants, vibration and other effects serve to break the fibers.

The extraction wheel should be made of a reasonably refractory material of good thermal conductivity that enable it to take and maintain a good edge and to withstand rapid and wide fluctuations in temperature. A Cu-Be alloy was chosen for this purpose, since this heat-treatable alloy offers high hardness and therefore good edge retention once the wheel tip is sharpened.

The range of metal and ceramics that may be cast by this process is limited only by the constraints of sufficient wetting of the wheel and reasonably low viscosity, ideally below 0.1 $Pa \cdot s$. Liquid metals offer few problems and almost all may be extracted into fibers.

With ceramics the situation is slightly less favorable; wetting of the metal wheel may be poor and viscosity, especially for ceramics containing silica, may be high. Ceramics that have been successfully extracted include mixtures of Al_2O_3, ZrO_2, TiO_2 and CaO, as well as a wide range of ferrites, and yttrium and bismuth-based high T_c superconductivity oxides [22, 93, 94].

Finally, it should be emphasized one great advantage of this technique over most liquid quenching methods, namely that the process is containerless, the melt being supported by the same material in the solid state. This allows fibers to be made from highly reactive metals, such as Zr and Ti, and from high temperature ceramics, such as Al_2O_3 for which finding a crucible is challenging.

3.4 Fiber Characterization Methods

3.4.1 X-Ray Powder Diffraction Analysis

The degree of crystallinity and the identification of the phases developed after crystallization were examined by x-ray diffraction analysis of crushed fibers. XRD patterns were registered on a Phillips APD 1700 X-ray Diffractometer (Cu-K_α radiation, λ = 1.54178 Å), at an accelerating voltage of 40 kV and a beam current of 20 mA, 0.02° of 2θ steps and counting times of 0.5 s/step. Specimens were scanned through angles of 2θ ranging from 10° to 90°.

Any diffraction pattern is characterized by a set of *line positions*, 2θ, and a set of relative *line intensities*, *I*. The angular positions of the lines depend on the wavelength used, and more a fundamental quantity is the *d* spacing of the lattice planes forming each line. Each pattern is described by listing the *d* and *I* values of its diffraction lines, and to arrange the known patterns in decreasing values of *d* for the strongest line in the pattern. This arrangement made possible a search procedure which would quickly locate the desired pattern. The identification of the phases was carried out by comparing and matching the plane spacing (*d* values, described in the Bragg Law) of the strongest lines of the measured data and the reference patterns in the JCPDS database using the PC-APD program.

3.4.2 Microscopy

Fibers were characterized using a scanning electron microscopy (SEM JEOL JSM 840A) that was operating at 15 keV. SEM samples were prepared by mounting fibers (~5 mm in length) on an aluminum stub using conductive carbon tape. The fibers were sputter coated (Hummer VI, Anatech, Ltd., USA) with Au/Pd to improve the conductivity.

Method of Preparation of Fiber Cross Sections

The goal of this step is to impregnate fibers with a cold-curing low-viscosity epoxy (Epo-Thin, Buehler, Ltd.) to produce a sample with a high fiber volume fraction. Fiber tows were saturated with epoxy and then fed into a 2-mm-diameter disposable glass pipette tip. The fiber-filled pipettes were placed directly into an oven at 32-38 °C to cure the epoxy within 3-4 hours or at room temperature to cure the epoxy within 18-20 hours. To obtain the

fiber cross sections, the epoxy-impregnated tows of 1 cm lengths were mounted in a conventional metallographic mounting medium (Epomet, Buehler, Ltd.) to increase stability during grinding and polishing. The specimens were ground using silicon carbide paper and polished with a polishing cloth and a polycrystalline diamond suspension of 1 μm and 0.25 μm (Metadi Supreme, Buehler, Ltd.) to produce a flat, scratch-free cross-section.

Fiber diameters were measured on cross sections using image analysis (LECO 2005 Image Analysis System) at a magnification of x500. The feature measurements were the *Feret Average*, *Roundness* and *Area*. Ferets are straight line measurements made between tangents at various angles. The system has three modes or groups of ferets available: 8, 16 and 32. The 8 ferets, which was used, has the following ferrets: 0, 22.5, 45, 67.5, 90, 112.5, 135 and 157.5° (see Figure 3.5). The *Feret Average* is the average of all the ferets.

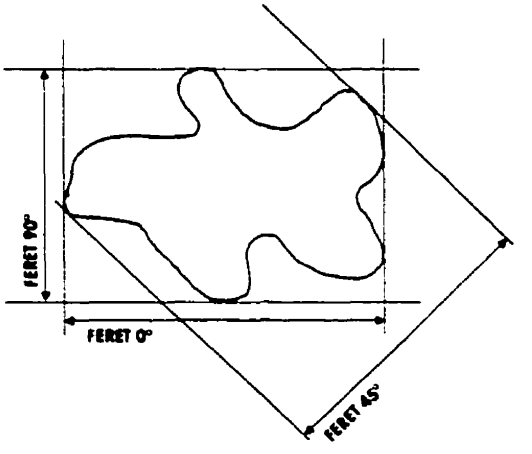

Figure 3.5 Schematic showing the measurement of ferets at 0°, 45°, and 90°.

Roundness is defines as follows:

$$\frac{4\pi A}{p^2} * 100 \tag{3.1}$$

where A is the area and p the perimeter. For a perfect circle, roundness = 100. It is impossible to obtain exactly 100 with an image analyzer because of the square matrix created by the pixels. The best circle will usually have a roundness of approximately 95 (Figure 3.6).

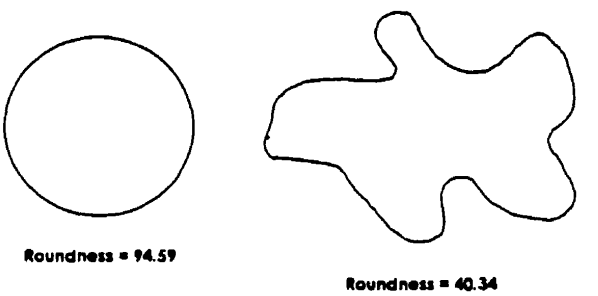

Figure 3.6 Comparison of the roundness of two objects.

Area of an element is the sum of pixels present in that feature (Figure 3.7).

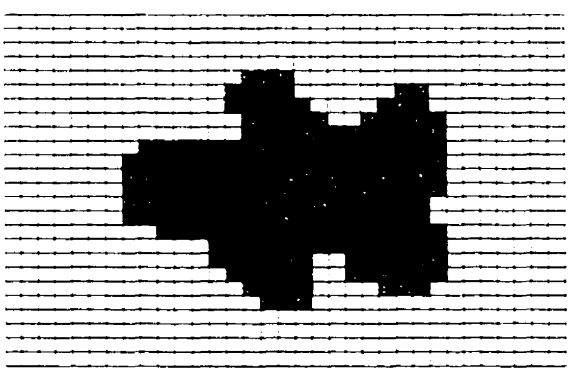

Figure 3.7 Schematic showing the measurement of the area of an object.

Electron probe microanalysis (EPMA JEOL–8900 electron microprobe) was used to evaluate the chemical composition on carbon-coated fiber cross-sections. EPMA data were based on Y and Al analyses using Al_2O_3 and $Fe_5Y_3O_{12}$ as standards.

3.4.3 Thermal Analysis

To determine the crystallization and glass transition temperatures of the amorphous fibers and the change in phase assemblage, differential scanning calorimetry analysis (Netzsch DSC 404) was performed on crushed samples loaded into a platinum crucible and heated to 1400 °C at a rate of 10 °C/min. The resulting samples were x-rayed to detect and identify phases formed upon devitrification. Figure 3.8 shows a schematic diagram of the Netzsch High-Temperature DSC 404.

Differential thermal analysis (DTA7 Perkin-Elmer) was used to study the crystallization phenomena of Y_2O_3-Al_2O_3 fibers and calculate the activation energy of crystallization. The DTA measurements were performed using a constant weight of 40 mg of short fibers in an alumina crucible under argon atmosphere with various heating rates of 3-100 °C/min from 750 to 1400 °C. Alumina powder was used as a reference material. Prior to measurement, the temperatures of the DTA were calibrated using aluminum (Al-99.9 +%, MP = 660.10 °C) and gold (Au-99.9 +%, MP = 1063 °C) standards. Figure 3.9 shows a schematic of the DTA.

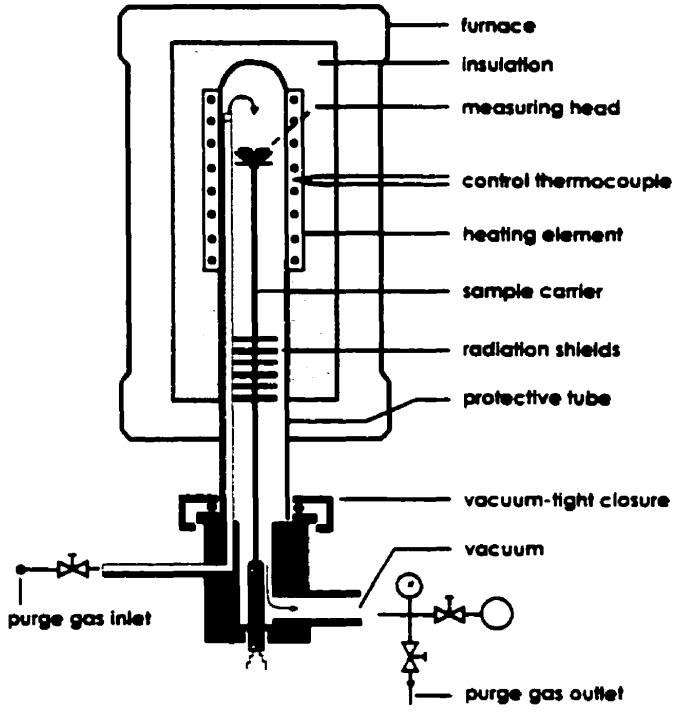

Figure 3.8 Schematic diagram of the Netzsch High-Temperature DSC 404.

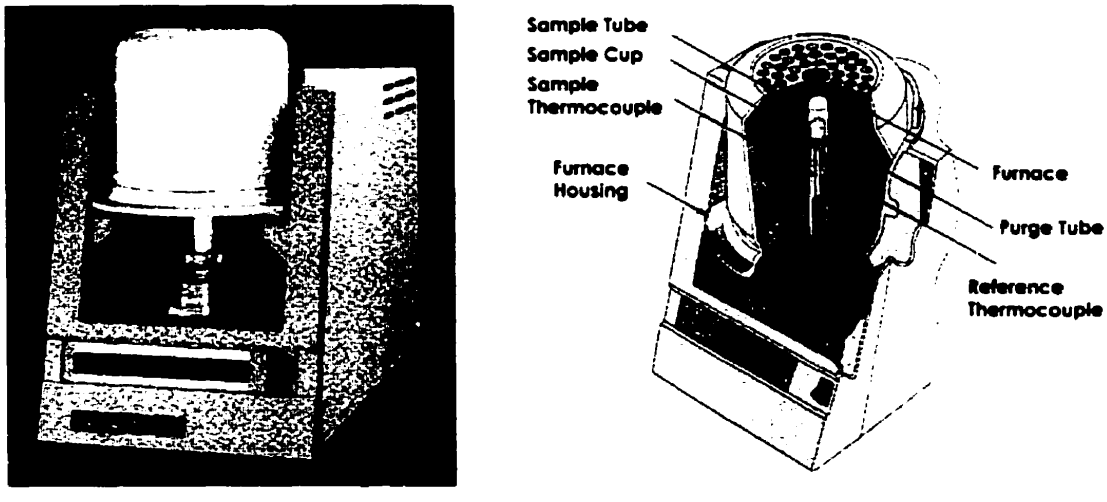

Figure 3.9 Schematic diagram of the DTA7 Perkin-Elmer.

Figure 3.10 shows the parameters analyzed on a DTA peak: $(\delta T)_p$ is the maximum height of the DTA peak, T_p the temperature at $(\delta T)_p$, and $(\Delta T)_p$ the width at half-peak maximum (peak width).

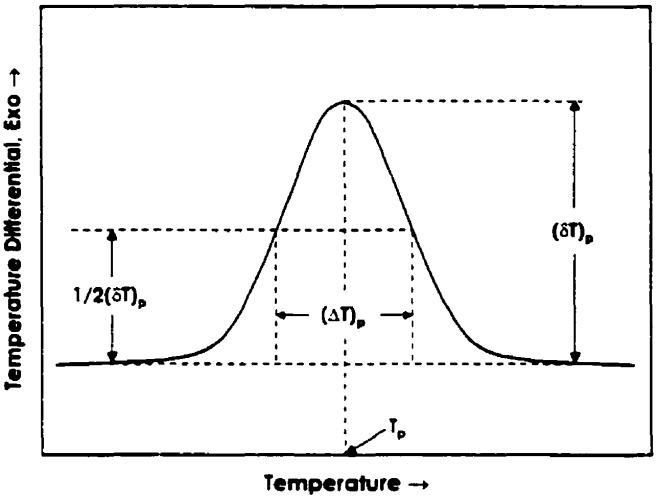

Figure 3.10 Schematic of a DTA crystallization peak, showing the parameters for analyzing the DTA results.

3.4.4 Heat Treatments

Crystallization of the fibers has a significant effect on fiber morphologies and properties. These effects were studied on crushed fibers placed in Al_2O_3 boats and heated in air at a rate of 10 °C/min to selected temperatures (800-1500 °C), followed by a holding period of 1 to 8 h and then furnace cooling. Heat treating experiments at temperatures > 1200 °C were conducted in a furnace (1700 °C Box Furnace, Lindberg-Blue M) that was equipped with a programmable temperature controller. Heat-treating experiments at temperatures < 1200 °C were conducted in another furnace (1200 °C Box Furnace, Lindberg-Blue M) equipped with a controller.

3.4.5 Nucleation Experiments

The crushed glass fibers placed in Al_2O_3 boats were nucleated first in a furnace (1200 °C Box Furnace, Lindberg-Blue M) for 2 hours at temperatures between 600 to 850 °C and then heated in the DTA apparatus at 20 °C/min until crystallization was complete. A constant sample weight of 40 mg was used for all measurements.

3.4.6 Bulk Chemical Analysis

The bulk chemical composition of the as-extracted fibers was analyzed (ICP-AES Trace Scan, Thermo Jarrell Ash) in order to check the compositional homogeneity and establish whether material losses were encountered due to the melting process.

Atomic emission spectrometry, using the inductively coupled plasma source is a technique for multi-element analysis at trace levels. In the ICP, the sample is introduced to a region where the gas temperature approaches 7000 K, thus ensuring a high degree of ionization.

The high sensitivity of ICP-AES and the wide range of trace elements which are incorporated into most analytical protocols, require that great care must be taken to avoid contamination during sample preparation. Many materials must be ground and homogenized prior to digestion, to ensure that a representative portion of the bulk sample is analyzed. It is commonly accepted that a maximum grain size of 200-mesh (75 μm) is required to assure sample homogeneity. Fibers were ground and digested with hydrochloric acid, then diluted

with distilled water. Procedural blanks should always be prepared for each batch of samples. In preparing a blank, the entire chemical treatment used on the sample is duplicated but no sample is added. The final reading is the blank reading, which simultaneously corrects for background and any contribution to the analyte signal from the reagent used.

3.4.7 Mechanical Properties Evaluation

Tensile strength of glass fibers was measured using an Instron material testing machine operated under computer control. The fiber diameters were about 30 μm, the gauge length was fixed at 30 mm, approximately 1000 times that of the fiber diameter. Test fibers were bonded into a specially designed paper frame with epoxy adhesive (Figure 3.11). The measurement technique and interpretation was consistent with ASTM standard D3379-75 [95]. A random selection of single filaments is made from the material to be tested. The filaments are center-line mounted on special slotted tabs. The tabs are gripped so that the test specimen is aligned axially in the jaws of a constant-speed movable-crosshead test machine. The paper of the mounting tabs was then cut away. The filaments are then stressed to failure at a constant strain rate of 2mm/min at room temperature. A high sensitivity load cell of 10 N was used to measure the load (Figure 3.12). A computer was used to record the load and displacement as a function of time. For this method, filament cross-sectional areas are determined by planimeter measurement of a representative number of filament cross sections as displayed on highly magnified photomicrographs. Tensile strength and Young's modulus are calculated from the load-elongation records and the cross-sectional area measurements. The fracture cross section of the broken fiber was then assessed by SEM.

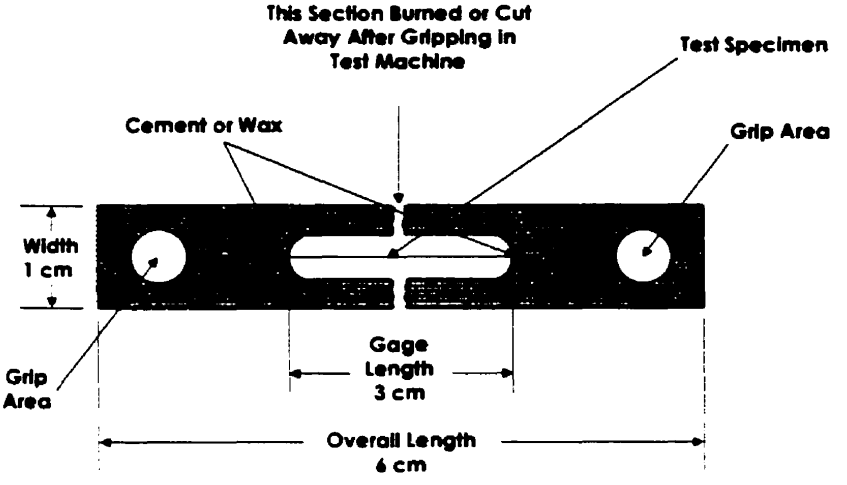

Figure 3.11 Typical specimen mounting method.

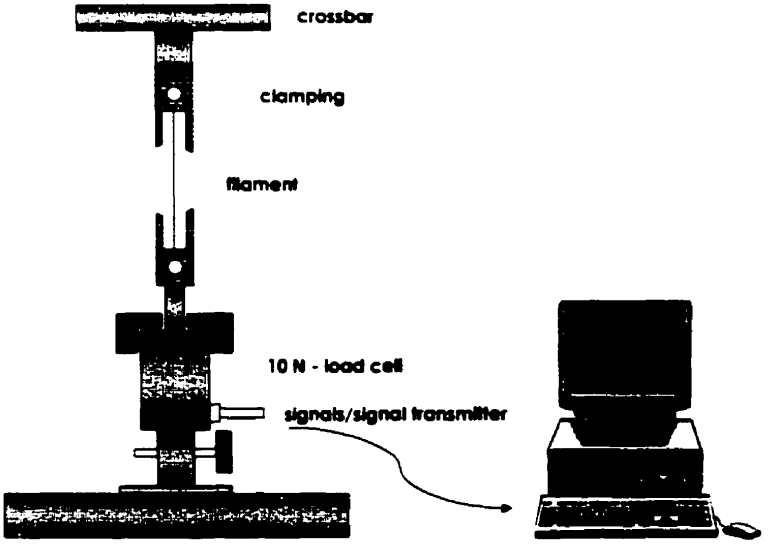

Figure 3.12 Schematic of the universal test machine.

CHAPTER 4

FIBER PRODUCTION AND CHARACTERIZATION

The objective of this chapter is to present the results in relation to the characterization of the ceramic fibers produced by melt extraction process. The properties of the extracted fibers are comprised of morphology, crystallinity, and chemical composition. Mechanical properties such as tensile strength and Young's modulus in addition to a Weibull statistics will also be presented.

4.1 Fiber Characterization

4.1.1 Morphology and Surface Characteristics of Extracted Fibers

The selected yttria-alumina compositions could be melt-extracted and Figure 4.1 shows SEM micrographs of fibers extracted at different wheel velocities. Generally two types of fibers were obtained: uniform diameter fibers at wheel speeds < 3 m/s and fibers exhibiting waves at higher velocities. The fibers produced at speeds < 3 m/s had almost

circular cross sections, except at the point of contact with the wheel, and were uniform in diameter.

For this range (wheel velocity < 3 m/s), the extracted layer was thin enough to be rapidly solidified by the wheel tip. Under these conditions, no instability occurred within the liquid layer, and uniform diameter fibers were produced with typical diameters of 20-30 μm (Figure 4.2(a)). However, at higher wheel velocities, waves formed on the fibers and the size uniformity decreased. The remaining liquid layer tended to form instabilities which spherodize because of the effect of surface tension attempting to minimize the surface area. Hence, the shape of the extracted fiber was no longer uniform. These fibers usually consisted of smooth thin sections of 20-30 μm diameter with periodic waves of diameters up to 60-70 μm (Figure 4.2(b)).

The above can be explained by taking into account that at higher velocity, more material is extracted, since the rapid extraction pulls a thicker stream of liquid ceramic from the molten drop, which cannot solidify rapidly (the wheel cannot remove heat fast enough). Therefore, the effects of surface tension come into play and waves are formed. The formation of waves has been reviewed in previous work [96]. This can be divided into three regions as follows: (1) the contact of the wheel tip with the molten drop; (2) the travel length or residence time on the wheel after exit from the molten drop; and (3) the region after separation from the wheel (Fig. 4.2(b)).

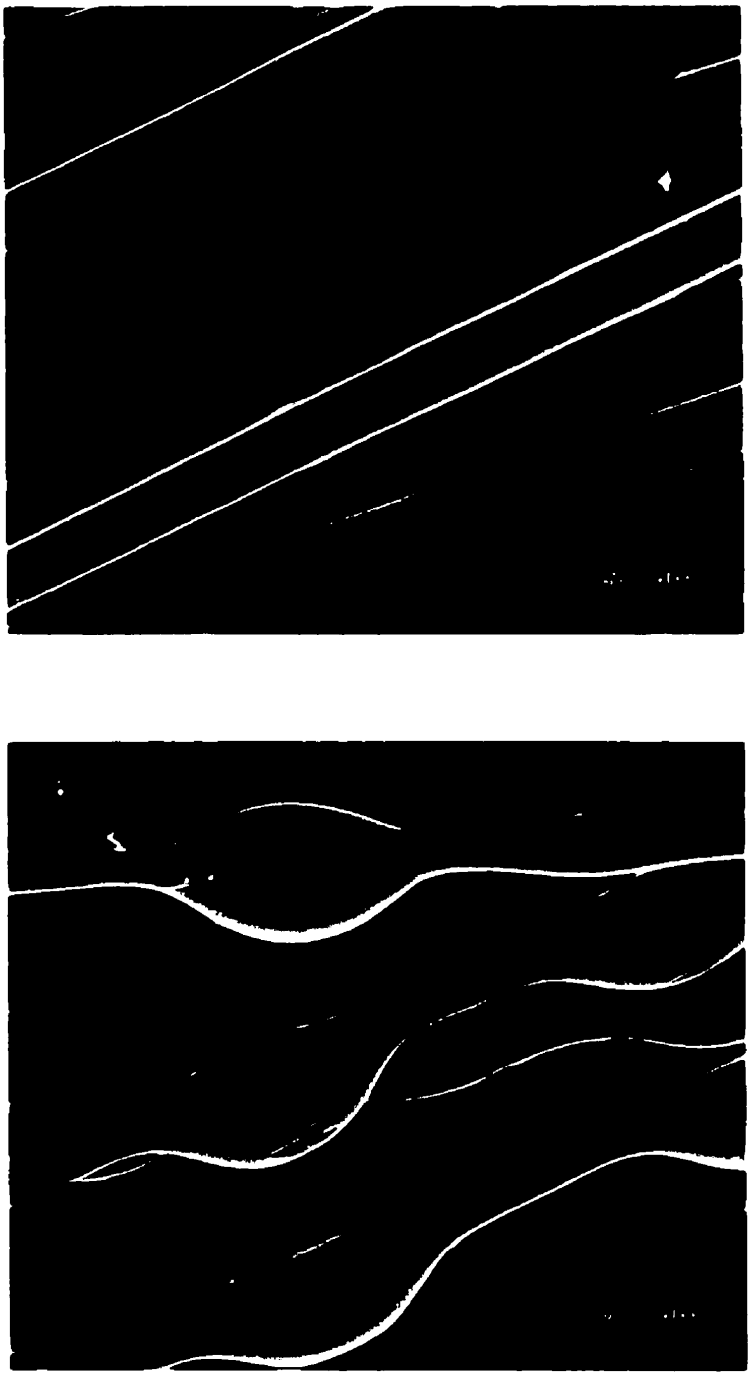

Figure 4.1 SEM micrographs of the melt-extracted Al_2O_3-Y_3A_5 eutectic fibers: (a) uniform cross-section fibers (1.5m/s), and (b) fibers exhibiting Rayleigh waves (3.5 m/s).

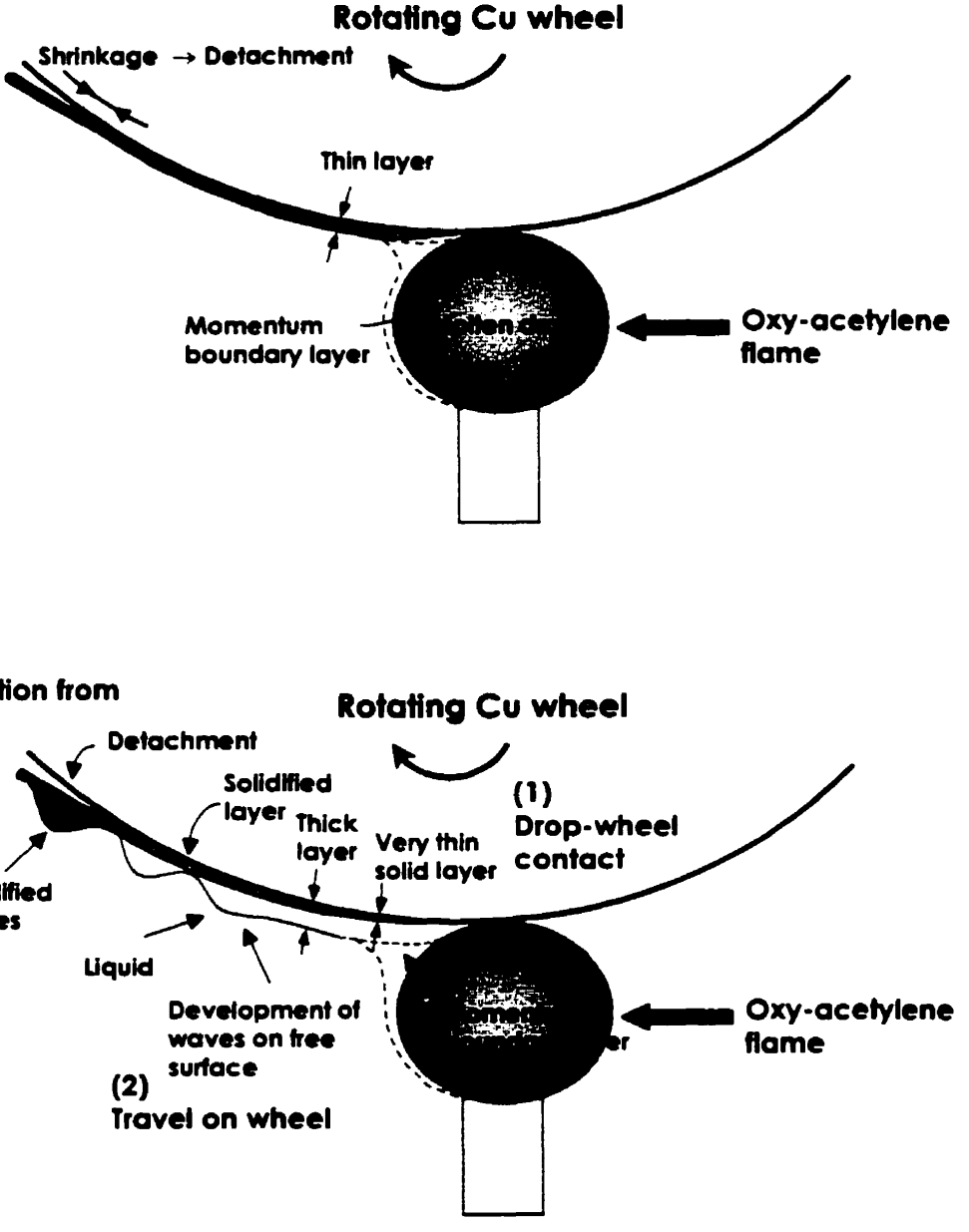

Figure 4.2 Schematic diagram of the formation of (a) uniform fibers (low wheel speed), and (b) fibers exhibiting waves (rapid wheel speed).

During the contact of the wheel tip with the molten drop (region 1), a very thin solid layer starts to form in the contact area, whereas the layer in which the liquid is in motion (i.e. the momentum layer) is much thicker. The extracted layer becomes rapidly thinner as it exits the drop, and reaches a thickness defined as the mean fiber diameter (i.e. the fiber dimension prior to the formation of waves). This layer is extremely thin (of the order of the fiber dimension) and is a mixture of liquid and solid as it travels further on the wheel. During this stage (region 2), the solidification front proceeds towards the free surface of the liquid fiber by conduction into the wheel tip. Meanwhile, the surface tension, which tends to reduce the surface area of the liquid layer, comes into effect, and waves form quickly on the free surface of the fiber.

Solidification shrinkage and cooling of the fiber build up large stresses along the contact area with the wheel tip, which cause separation of the fiber from the wheel. When the solidified fiber is airborne (final stage or region 3) it is cooled by radiation and convection since there is no longer contact with the wheel (i.e. no conductive cooling). This lowers the overall cooling rates of the fiber.

Effect of Process Variables

The effect of wheel velocity on the morphology of the extracted fibers was analyzed in the previous section. The wheel tip radius is also crucial to melt extraction and its radius determines the dimensions and shape of the extracted fibers, as well as their quality. For a sharp wheel tip, the contact area between the liquid drop and wheel tip decreases. Therefore,

the extracted fibers tend to be thinner and more flexible. Figure 4.3 shows the imprint of the tip of the copper wheel, in cross-section, used to extract fibers. It is observed that the wheel tip radius of about 20 μm and is in the order of the dimensions of the diameter in the melt extracted fibers.

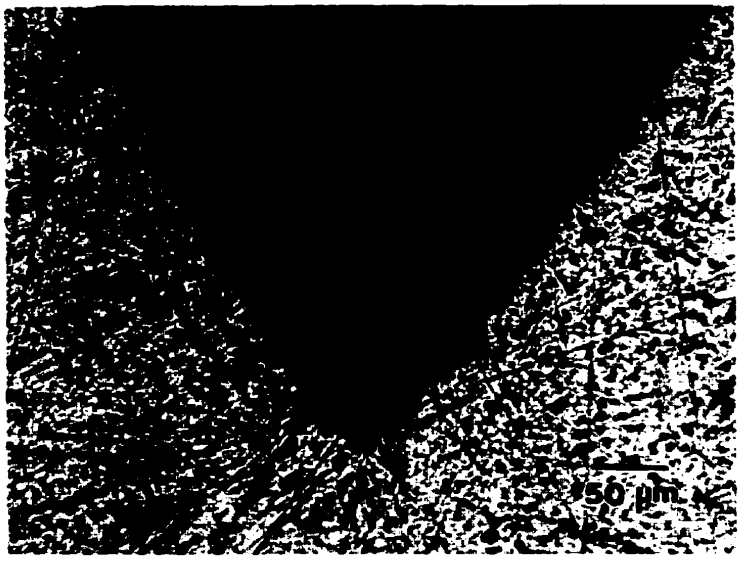

Figure 4.3 Actual profile of the wheel tip of the copper wheel used for melt extraction.

Another important parameter is the temperature of the liquid ceramic during extraction. The maximum temperature achievable by the oxy-acetylene torch is between 1900 and 2100 °C, and was obtained when the torch was kept quite close to the ceramic rod (5 mm). However, this caused instability of the small molten droplet due to the high pressure of the torch gas (35 kPa). In general, controlling the system, so that a light contact with the melt is obtained, was extremely difficult. To this end, only under specific and controlled conditions, it is expected that the product would have a smooth fiber form. When the copper disk slightly contacts the molten ceramic, if the temperature is high enough or the viscosity is sufficiently low then fiber extraction was achieved. This was the case of Y_3A_5

whose viscosity near to and above the melting point is of the order of 0.05 $Pa \cdot s$ [97]. Furthermore, the composition also exhibited a good wetting behavior with respect to the copper wheel. The optimum feed rate and wheel velocity in order to extract smooth and circular-cross sections fibers, were 3 mm/min and 1.1 m/s, respectively.

4. 1.2 Evaluation of Crystallinity by XRD

Rapid solidification has become a widely used technique to generate materials with unusual amorphous and/or metastable crystalline phases. Quenching of high melting temperature, inviscid oxides at sufficient rates to form a glass is not an easy task and many conventional rapid solidification techniques cannot be used. However, containerless processing permits sufficient undercooling of molten yttria-alumina compositions to achieve a viscosity range conducive to fiber-pulling or melt extraction.

X-ray diffraction patterns for yttria-alumina fibers are shown in Figure 4.4. X-ray patterns suggest that the as-extracted fibers are non-crystalline as indicated by the presence of a broad peak in the position of the maximum intensity peak for the YAG and YAP phase. Furthermore, they were found to be optically transparent. The transparency of the glass fibers is a result of the complete absence of grain boundaries or inclusions which would cause scattering of light. The uniform diameter fibers experienced high cooling rates during extraction, therefore, they vitrified during solidification. Even the thicker fibers, exhibiting Rayleigh waves, were amorphous because of the good glass formability of yttria-alumina mixtures.

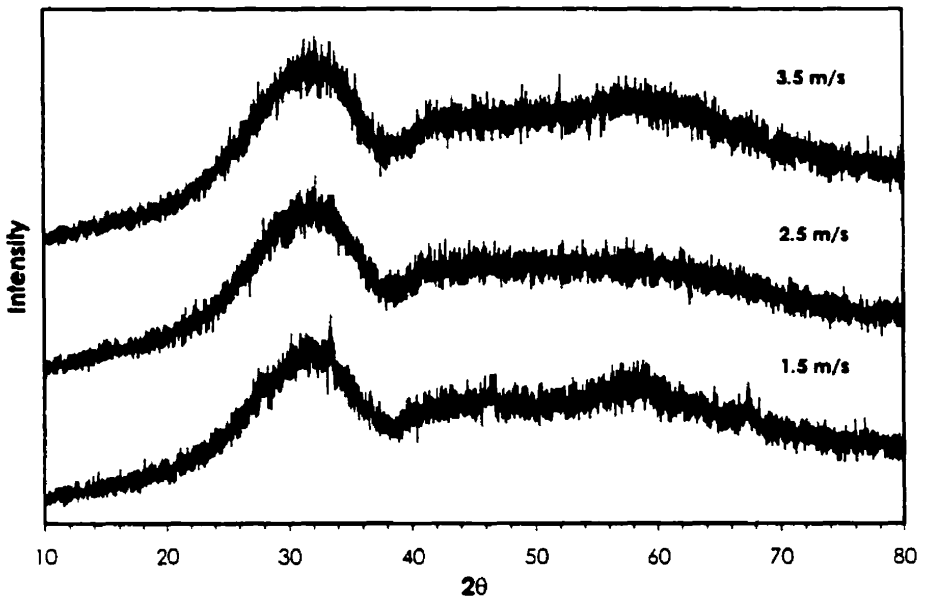

a)

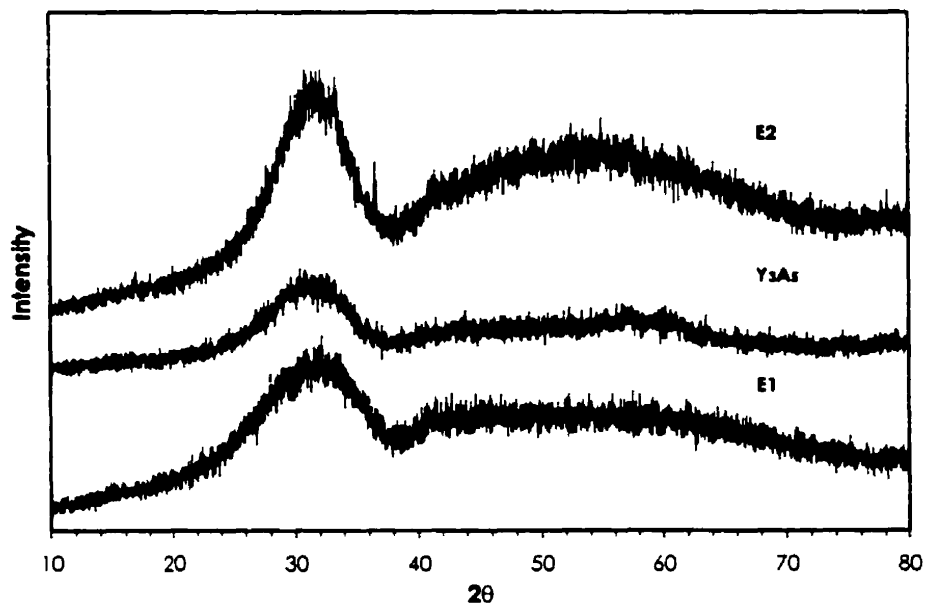

b)

Figure 4.4 XRD patterns of Y_2O_3-Al_2O_3 fibers. (a) E1 fibers extracted at 1.5, 2.5 and 3.5 m/s, and (b) E1, Y_3A_5 and E2 fibers extracted at 1.5 m/s.

In the yttria-alumina system, glass can be easily formed for a range of compositions. Compounds containing 30-35wt% Y_2O_3 are easy glass formers and, depending on cooling rate, the glass formation region can be extended to 70-75 wt% [98]. The limit values of glass formation in the Y_2O_3-Al_2O_3 system by rapid melt quenching at cooling rates of 10^7-10^8 K/s are shown in Table 4.1. The cooling rate of the melt extraction process was estimated previously to be in the order of 10^5 K/s for a 10 μm diameter ceramic fiber [93, 94]. It is noticeable that the cooling rate depends upon various parameters such as the wheel velocity, thickness of the fibers and adhesion to the wheel tip.

Table 4.1 Limit of glass formation in the Y_2O_3-Al_2O_3 system [98].

Limit of Glass Formation, Y_2O_3			
Lower		**Upper**	
mol%	**wt%**	**mol%**	**wt%**
15	28	60	77

Splat-cooling and Verneuil techniques. Cooling rate 10^7-10^8 K/s.

Usually in binary and ternary systems, the best glass forming compositions are found at or near the eutectic compositions. Indeed, the formation of glasses by rapid solidification is easier for compositions lying near a deep eutectic. Such compositions require relatively small undercooling below the melting point to reach the glass transition

temperature. In the current study, the selection of eutectic compounds enhanced the glass formability of the yttria-alumina compounds under the high cooling rates of the extraction system.

4.1.3 Composition Analysis by EPMA and Fiber Diameter Measurements on Fiber Cross Sections

Electron probe microanalysis were performed at the core and the edge of the fiber cross sections to establish any compositional variation. The results by EPMA, which are based on the average value of five analyses, are summarized in Table 4.2. No significant difference was observed between the core and the edge of the fiber, and hence, the extracted fibers were chemically homogeneous. In addition they were very close to their theoretical stoichiometry.

Fiber diameters were measured on the polished cross sections of a bundle embedded in an epoxy resin using image analysis. From Figure 4.5, it can be clearly seen that the track of the extraction wheel gives the fiber a distinctive kidney shape. This is more obvious in fibers with larger diameters, and tends to decrease the roundness of the fiber. Moreover there is a noticeable range of fiber sizes. Fifty to seventy five individual sections were measured for each fiber composition; the results are given in Table 4.3. According to the relative standard deviation or coefficient or variation, δ_D, it is possible to consider that the diameter varies from one fiber to another. Therefore the fiber diameter is found to vary as a

function of composition, with Y_3A_5 and E1 fibers having the smallest and largest diameters, respectively.

Table 4.2 Compositional distribution in Y_2O_3-Al_2O_3 fibers by EPMA.

Area for EDS		***Nominal wt%***			***Oxide wt%***	
		Al	**Y**	**O**	**Al_2O_3**	**Y_2O_3**
E1 ***Theoretical stoichiometry***					**62.9**	**37.1**
Core	Ave.	33.9	28.3	37.8	64.1	35.9
	SD	*0.16*	*0.23*	*0.14*	*0.30*	*0.29*
Edge	Ave.	33.9	28.6	37.9	64.1	36.3
	SD	*0.31*	*0.29*	*0.36*	*0.60*	*0.36*
Y_3A_5 ***Theoretical stoichiometry***					**43.0**	**57.0**
Core	Ave.	24.0	43.4	33.0	45.3	55.1
	SD	*0.36*	*0.40*	*0.22*	*0.69*	*0.50*
Edge	Ave.	24.1	43.6	33.2	45.5	54.4
	SD	*0.26*	*0.14*	*0.20*	*0.50*	*1.91*
E2 ***Theoretical stoichiometry***					**37.9**	**62.1**
Core	Ave.	20.8	48.3	31.6	39.4	61.3
	SD	*0.21*	*0.57*	*0.14*	*0.40*	*0.72*
Edge	Ave.	20.91	48.7	31.8	39.5	61.9
	SD	*0.17*	*0.43*	*0.20*	*0.33*	*0.55*

where: SD is the standard deviation.

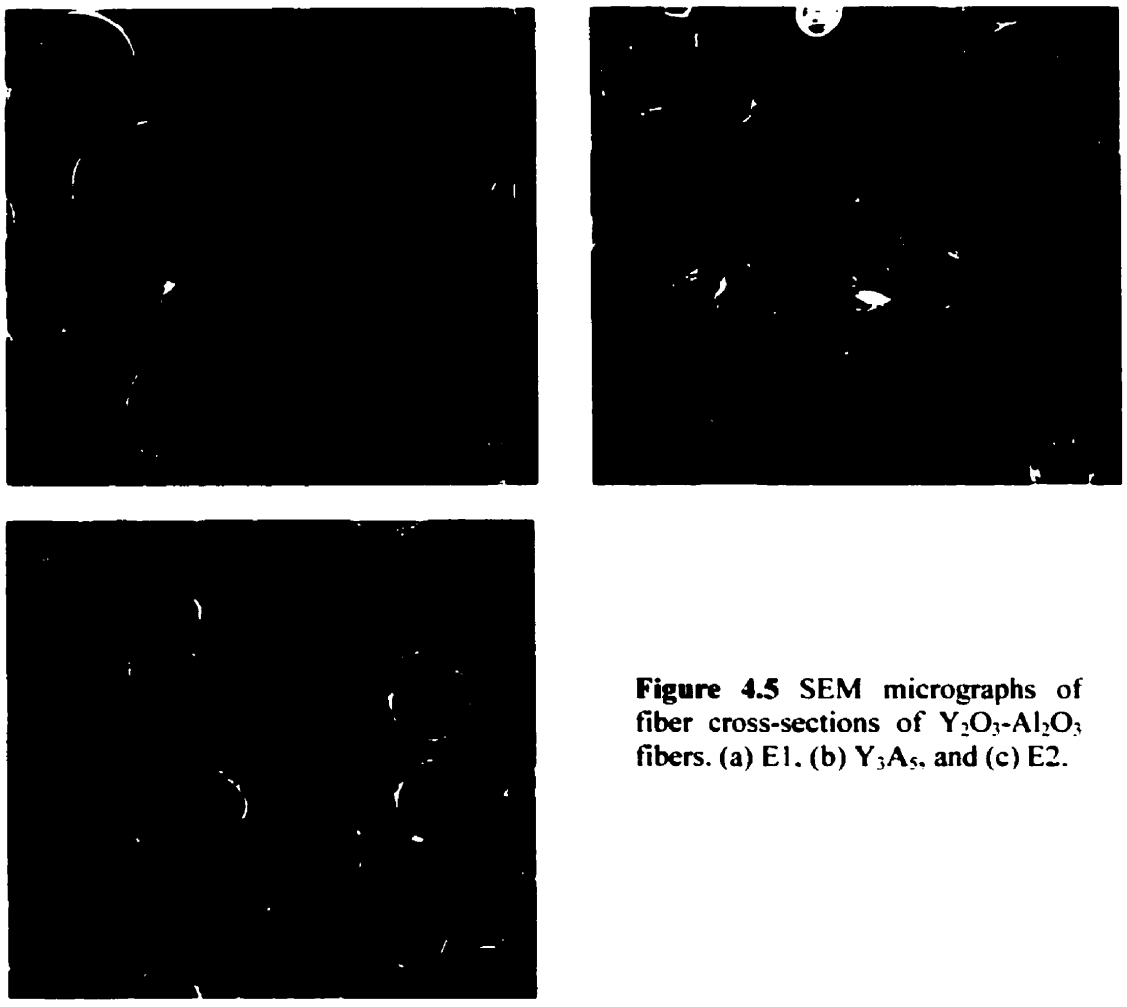

Figure 4.5 SEM micrographs of fiber cross-sections of Y_2O_3-Al_2O_3 fibers. (a) E1, (b) Y_3A_5, and (c) E2.

Table 4.3 Fiber cross-section measurements of the yttria-alumina fibers.

Fiber	$\overline{D}$ (μm)	*SD*(*D*) (μm)	δ_D (%)	$\bar{A}$ (μm^2)	Roundness
E1	29.9	7.9	26.4	699.3	76.6
Y_3A_5	23.0	4.9	21.3	387.2	69.6
E2	24.8	6.9	27.8	458.2	69.1

where: $\overline{D}$ is the mean diameter. *SD*(*D*) is the standard deviation. δ_D is the relative standard deviation, and $\bar{A}$ is the mean area.

4.1.4 Bulk Chemical Analysis

The bulk chemical composition of the as-extracted fibers was analyzed by ICP-AES (Inductively Coupled Plasma-Atomic Emission Spectrometer) in order to check the compositional homogeneity and establish whether material losses were encountered due to the melting process. Results are shown in Table 4.4. In general, fibers extracted from rods of E1, Y_3A_5 and E2 compositions retained their stoichiometry. In all cases, a slight decrease in the alumina content may have been caused by vaporization of Al_2O_3 during melting and extraction of the fibers.

Table 4.4 Chemical composition (wt%) of as-extracted fibers analyzed by ICP-AES.

Composition	Al_2O_3	Y_2O_3
E1	62.1	37.9
Y_3A_5	42.3	57.7
E2	36.7	63.3

4.2 Differential Scanning Calorimetry Analysis

The thermal transformation of glass fibers was followed by means of DSC and XRD identification of the resulting phases. The DSC curves at a heating rate of 10 °C/min in Figure 4.6 shows a small endothermic peak that occurs prior to crystallization and is due to the glass transition (T_g) temperature. The DSC curve for E1 fibers indicates two independent exothermic peaks at 949 and 1040 °C. The DSC trace of composition

Y_3A_5 exhibits a sharp exothermic peak around 942 °C. Y_3A_5 fibers prepared by other processes such as the sol-gel route and chemical precursor route (yttrium and aluminum nitrates) also showed a similar peak around 900-950 °C in the DSC trace [16, 20]. Composition E2 exhibited a single narrow exothermic peak at 939 °C.

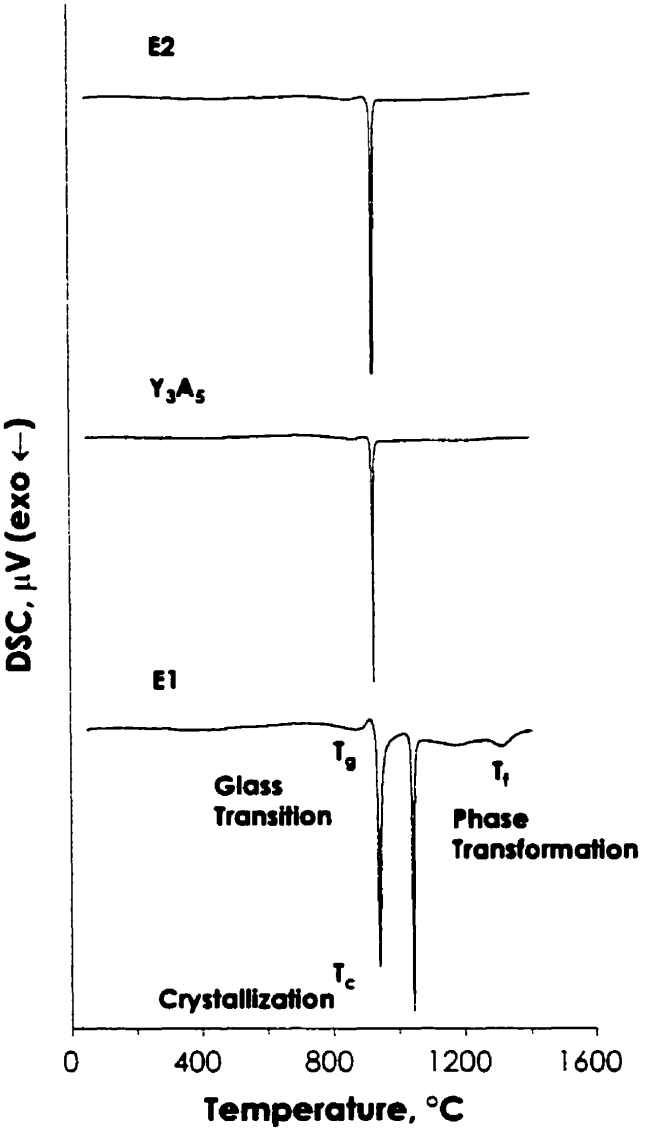

Figure 4.6 DSC thermograms of as-extracted Y_2O_3-Al_2O_3 fibers.

In order to identify the crystalline phases developed during the DSC treatment, samples were allowed to reach a predetermined temperature associated with the exothermic peak and quenched to room temperature prior to examination by XRD techniques. Silicon was added to the samples as an internal standard for XRD analysis. The phases found after each DSC peak for E1 composition were YAG (event 1) and δ-Al_2O_3 (event 2), as illustrated in Figure 4.7. A third small exothermic peak (event 3) was observed around 1300 °C corresponding to the phase transformation of δ-Al_2O_3 to α-Al_2O_3. From the thermogram, it can be seen that the heat evolution for the two crystallization peaks are equivalent, and according to the XRD pattern, relatively small amount of δ-Al_2O_3 phase is formed. Consequently, it is assumed that a metastable YAG phase is crystallized with the YAG structure but not with the YAG stoichiometry, that is with an excess of Al_2O_3.

Single YAG and cubic YAP were identified at the end of the DSC treatment for Y_3A_5 and E2 compositions, respectively, as can be seen in the XRD pattern show in Figure 4.8. These phases are in complete agreement with Y_2O_3-Al_2O_3 phase diagram, except for E2 in which YAG and YAP were expected after heat treatment. However, the phase development in the E2 composition occurs gradually during heating, forming a sequence of intermediate phases. These can be followed through the x-ray diffraction patterns taken from short fibers heated for 1 hour at various temperatures. The x-ray diffraction pattern for E2 fibers heat-treated at 1500 °C for 1h indicates the presence of

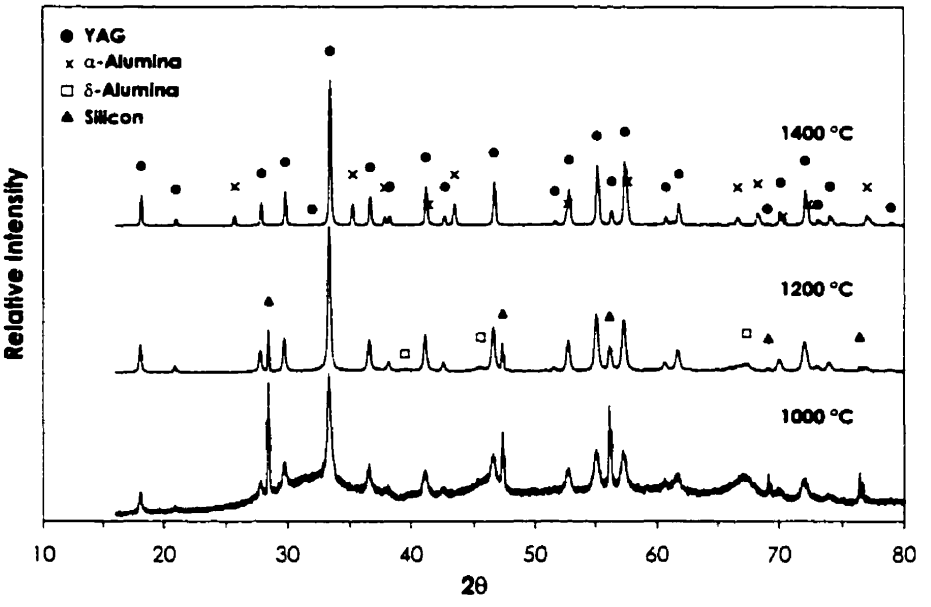

Figure 4.7 XRD pattern of Al_2O_3-Y_3A_5 eutectic fibers after DSC heat treatment. YAG peaks indexed by JCPDS card 33-40, α-alumina peaks by JCPDS card 10-173, δ-alumina peaks by JCPDS card 16-394 and silicon peaks by JCPDS 27-1402.

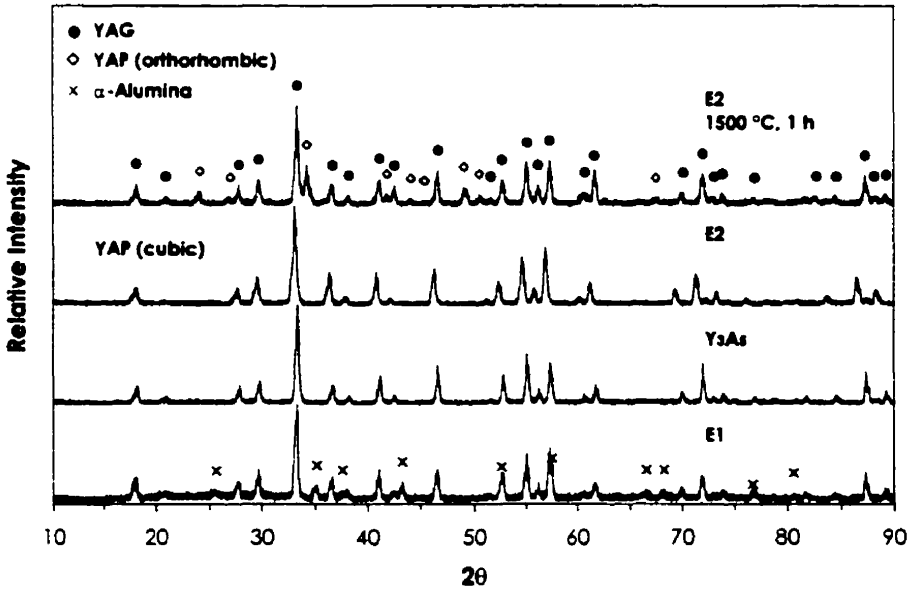

Figure 4.8 XRD pattern of Y_2O_3-Al_2O_3 fibers after DSC heat treatment. Cubic YAP peaks indexed by JCPDS card 38-222 and orthorhombic YAP peaks by JCPDS 33-41.

YAG and orthorhombic YAP as coexisting phases. However, there was no evidence of this transformation in the DTA scan because the transformation from cubic to orthorhombic is a difussionless process with no apparently detectable enthalpy (see section 5.4).

4. 3 Tensile Testing

Tensile strength tests of glass fibers were performed at room temperature in an Instron tensile machine. The actual diameters, obtained by microscopic examination of the fractured fibers, were used in the calculation of strength values and are presented in Figure 4.9 and Table 4.5.

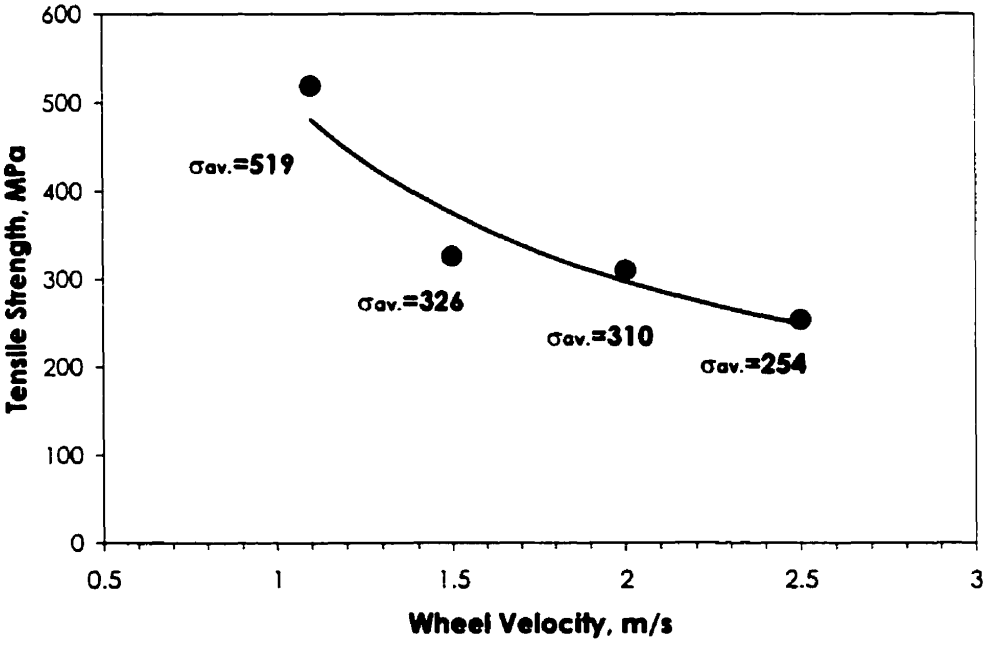

Figure 4.9 Tensile strengths of as-extracted E1 fibers as a function of extraction wheel velocity.

It is observed, from Figure 4.9 that as the wheel velocity increases the tensile strength decreases and this can be attributed to the discontinuities along the fiber. As wheel velocity increases, the morphology of the fibers tends to change from uniform circular cross section to those exhibiting waves, which introduce defects and stress raisers into the fibers.

Table 4.5 Tensile strength and elastic moduli data of as-extracted Y_2O_3-Al_2O_3 fibers.

Fiber	Tensile Strength MPa	Elastic Modulus GPa
E1	681	116
Y_3A_5	776	121
E2	606	95

The tensile strengths of the uniform fibers are moderate with values ranging from 606 to 776 MPa. Note that the tip of the Cu wheel cannot be perfectly rounded and smooth, therefore, any surface irregularities on the wheel tip are replicated onto the fibers, resulting in the possibility of a defective fiber surface. The main defect is the wheel track as can be seen in Figures 4.10 and 4.11, also fibers have shrinkage (ridges) which are secondary defects (Figure 4.10 (a)), and inhomogeneity in fiber diameter, i.e. thin and thick sections along the fiber length. Obviously, these defects can significantly affect the tensile strengths of the fibers, and can lead to the large scatter of fiber strengths. Normally, the quality of the wheel tip and its homogeneity throughout the wheel

circumference is extremely important with respect to obtain good mechanical properties of the fibers. Another source of scatter may also result from handling damage after processing. On the other hand, Y_3A_5 fiber composition showed the highest tensile strength, 776 MPa, and it was shown in previous section that this fiber had the smallest average diameter, 23 μm, therefore the flaw population and defect size in the fibers could be smaller. The inherent strength of a fiber increases as the fiber diameter is decreased. And, not only does tensile strength increase with decreasing fiber diameter, but modulus values usually increase as well. The generally accepted explanation for these phenomena is that there are fewer imperfections and faults as the fiber diameter is reduced.

An analysis of the fracture surfaces by SEM revealed the cause of fracture during mechanical testing. Fig. 4.10 shows the fracture surface after tensile testing of as-extracted fibers at room temperature. All the fibers exhibited brittle failure and always initiated from flaws on the fiber surface caused by the extraction process and related to the wheel track. This is especially clear in Figure 4.10(b), where it seems that the edge of the fiber which form first, along the wheel edge, is more susceptible to imperfections. The fracture origin in brittle ceramics normally consists of some irregularity or singularity in the material (flaws) which acts as a stress concentrator. Flaws in a ceramic concentrate the stress, fracture occurs when the stress at the flaw reaches a critical value sufficient to initiate and extend a crack [99, 100].

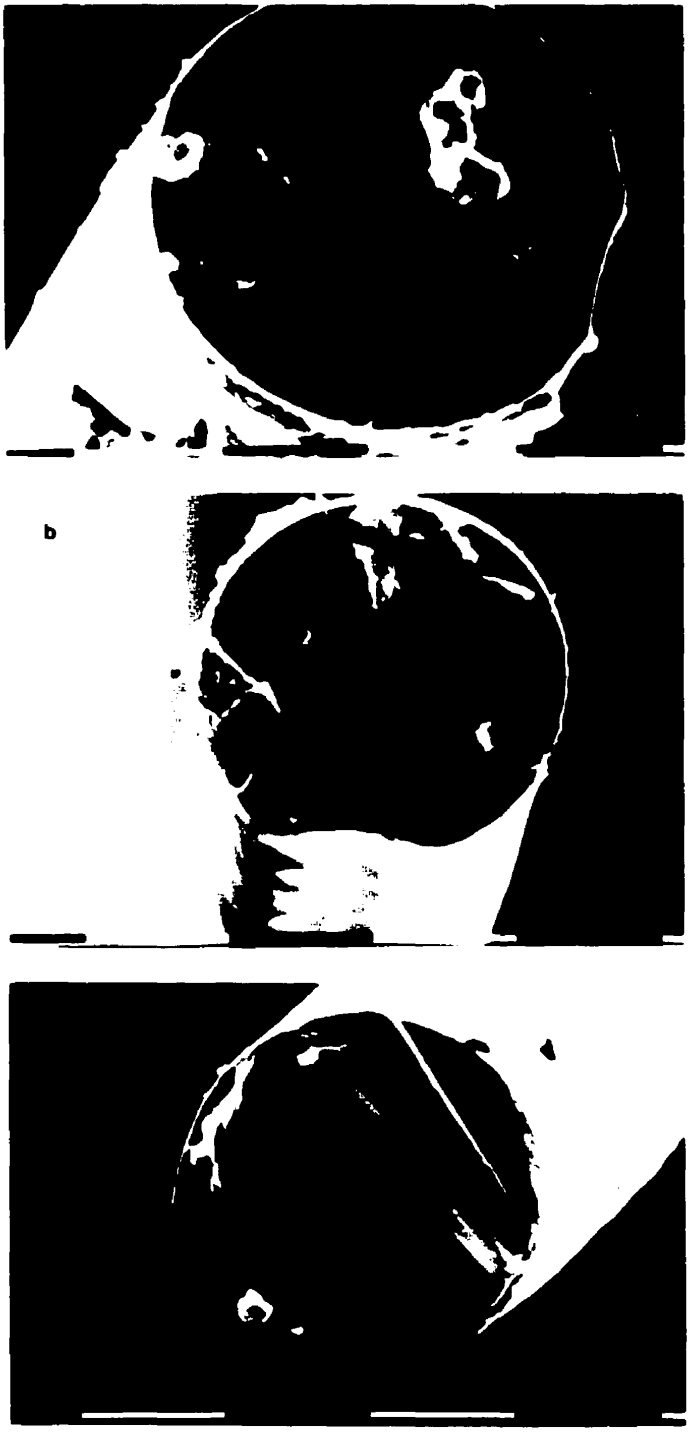

Figure 4.10 SEM micrographs of fracture surfaces of as-extracted Y_2O_3-Al_2O_3 fibers after tensile strength tests. (a) E1, (b) Y_3A_5, and (c) E2.

Figure 4.11 depicts a schematic and SEM micrograph of a fracture surface in a ceramic fiber which failed in a brittle manner. The flat and smooth 'mirror' is bounded by the region containing small radial ridges know as 'mist'. The mist is bounded in turn by 'hackle' containing larger radial ridges.

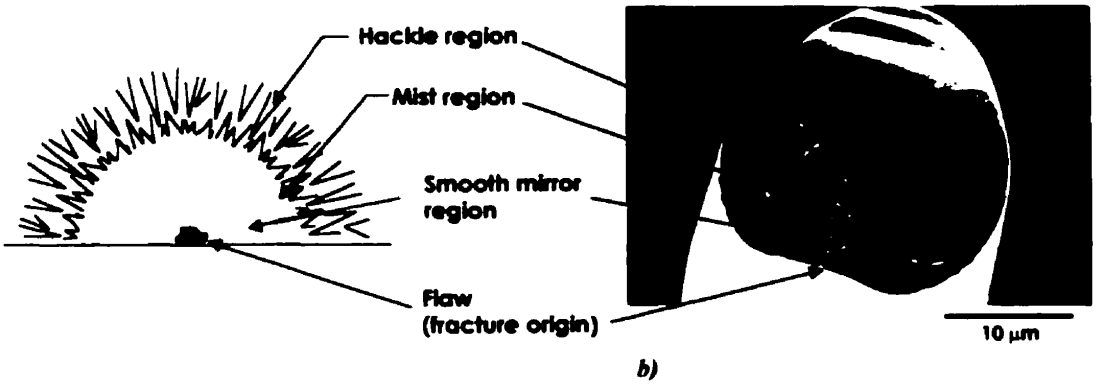

Figure 4.11 Fracture surface of a ceramic fiber, which failed in a brittle manner. (a) A schematic of a flaw located at the surface; (b) A SEM micrograph of a surface-located flaw in a E2 glass fiber fractured in a tensile strength test.

The modulus of elasticity for amorphous fibers were calculated from Hooke's law, knowing the fracture load and elongation at fracture of the fibers and using the equation $E = \sigma/\varepsilon = (\sigma \cdot L_o)/\Delta L$, where σ is the fracture stress, L_o is the gauge length (initial length) and ΔL is the deformation. The average elastic moduli (calculated from at least 30 measurements) are listed in Table 4.5. The Y_3A_5 and E2 fiber compositions showed the highest and the lowest values of modulus, respectively. These moderated values of modulus of elasticity are attributed to the amorphous nature of the fibers. The magnitude of the elastic modulus is determined by the strength of the atomic bonds in the material. The stronger the atomic bonding, the greater the stress required to increase the

interatomic spacing, and thus the greater the value of the modulus of elasticity. The more open structure, weaker bonding and lower co-ordination number of an amorphous structure result in moderate to low elastic modulus [100].

However, the moderate elastic modulus of the fibers can be enhanced by a partial and controlled crystallization of the fibers. The crystallization of amorphous materials leads to higher elastic modulus, however, the strength of the resulting materials is usually compromised. Nevertheless, a controlled crystallization procedure could be developed to improve the overall properties of the fibers by balancing a higher elastic modulus at the expense of lower strengths. Note that a controlled heating or crystallization of these fibers may result in nanocrystalline materials which offer the potential for improving the overall mechanical properties.

4.3.1. Weibull Statistics

Tensile test were performed at room temperature using a constant gauge length (30 mm) at a constant displacement rate. Thirty individual fibers were tested. This number of tests was required in order to obtain reliable statistical parameters [101, 102].

Weibull modulus was calculated using the two-parameter Weibull plot or strength distribution method (Equation 4.1), for a constant tested volume (gauge length for fibers) (see Appendix A).

$$\ln\left[\ln\left(\frac{1}{1-P}\right)\right] = m\cdot\ln(\sigma) - m\ln\sigma_0 \qquad (4.1)$$

where σ is the applied stress, σ_0 is a scale parameter (often selected as the characteristic stress, at which probability of failure is 0.632), and m is the Weibull modulus, which describes the flaw size distribution (and thus the data scatter).

The estimators of the Weibull modulus are obtained by the following procedure. Each test strength is assigned a ranking (i) in order of increasing failure strength. The failure probability was calculated for each ranking with the formula

$$P_i = \frac{(i-0.5)}{n} \tag{4.2}$$

where n is the total number of fibers tested. This is the most accurate estimator for small sample sizes ($\leq$ 50 specimens) [102-104]. The estimator of the Weibull modulus is obtained from a least-squares linear regression fit of a line to the failure probability/strength data on a plot of $\ln[\ln(1/1-P)]$ vs $\ln(\sigma)$ where $1-P$ is the probability of survival and σ is the strength. The slope of the line fitted to the data is the estimator for the Weibull modulus. The assumption is made that only a single flaw causes failure.

Tensile testing of filaments is tedious and time-consuming. A significant amount of labour is invested in the measurement of the diameter for each filament. If the average filament diameter of a sample of filaments is assumed to be representative of all of the filaments of that filament type from the same lot, then an average diameter could be employed to derive the tensile strength and the Weibull modulus for filaments. It has been found that the strength obtained using an average filament diameter for a set of

specimens is in good agreement with the strength found using measured filament diameters. Furthermore, the estimator of the Weibull modulus derived using an average filament diameter is a good approximation of the estimator of the Weibull modulus derived from measured filament diameters [105]. In practice, the determination of an average diameter for a particular type of filaments should be necessary only once, provided that the filaments from which the average diameter was obtained are representative of all filaments from the same lot. Verification of the average diameter for different lots would be prudent. In conclusion, proper use of an average filament diameter is a valid procedure that will facilitate finding the tensile strengths and Weibull moduli of filaments in an efficient manner.

Figure 4.12 shows the distribution of single filament strength for the three Y_2O_3-Al_2O_3 fibers. The data has a slightly sinusoidal form, as expected. Weibull plots for the three Y_2O_3-Al_2O_3 fibers are shown in Figure 4.13. The data was fitted using the least squares method: the two-parameter Weibull equation fit the data fairly well, although some deviation from the best-fit line occurred at the high and low strengths. The calculated Weibull moduli, as well as characteristic stress and correlation coefficients are given in Table 4.6. The Weibull modulus for the as-extracted yttria-alumina fibers ranges from 2.3 to 2.8. Among the fibers tested in the present study, Y_3A_5 fibers exhibited a slightly higher Weibull modulus than the others since this fiber had the smallest average fiber diameter and diameter variability, as shown in Table 4.3. It is not well understood

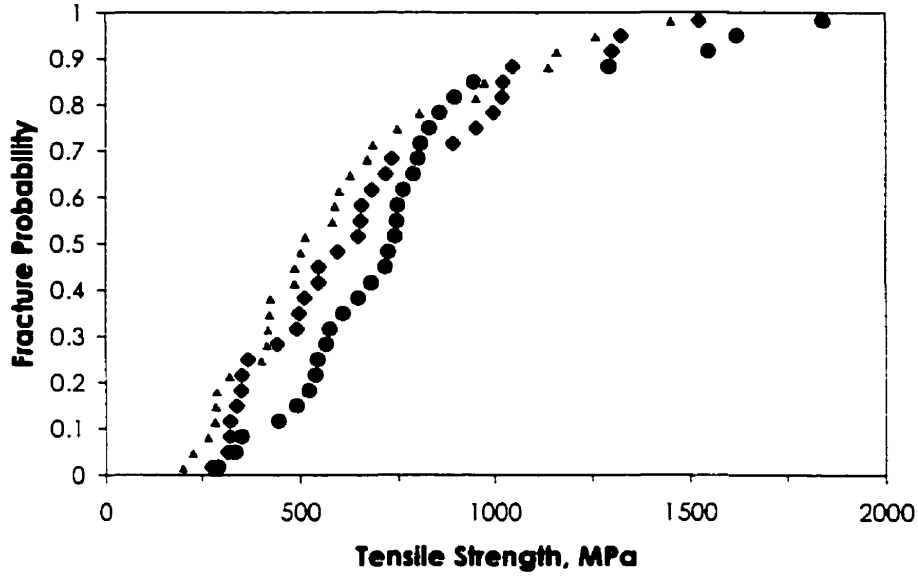

Figure 4.12 Fracture probability plot of as-extracted Y_2O_3-Al_2O_3 fibers. (◆) E1, (●) Y_3A_5, and (▲) E2.

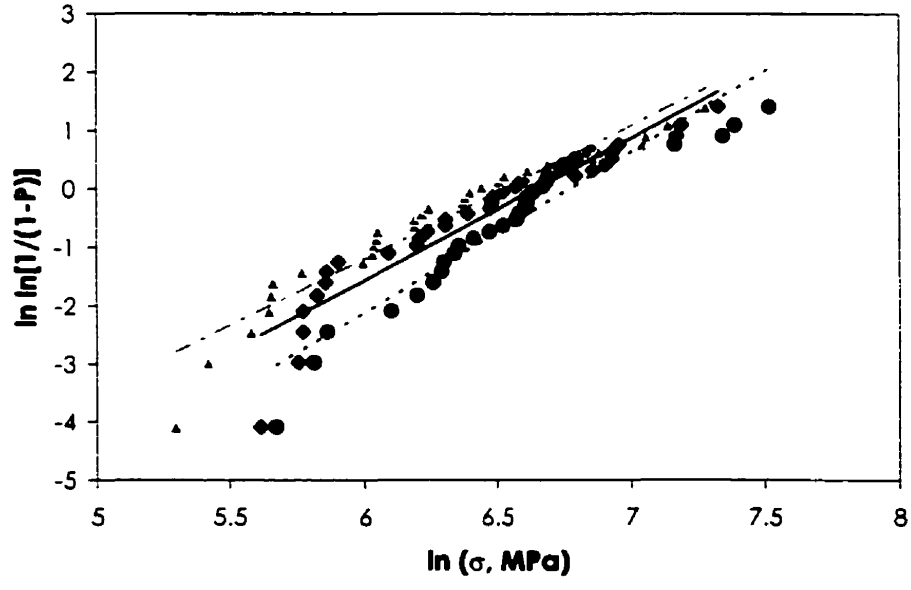

Figure 4.13 Weibull plot of as-extracted Y_2O_3-Al_2O_3 fibers. (◆ ——) E1, (● ·····) Y_3A_5, and (▲ – · –) E2.

that fiber diameter variability will have an effect on measured Weibull modulus. Weibull theory predicts that fibers with larger diameter should, on average, have a greater chance to contain larger flaws, and will therefore be weaker than smaller fibers. Therefore, for fiber strength testing, it has special relevance.

Table 4.6 Results of the Weibull statistics for Y_2O_3-Al_2O_3 fibers.

Fiber	*m*	σ_0 (MPa)	r^2
E1	2.4 ± 0.16	767	0.8909
Y_3A_5	2.8 ± 0.17	868	0.9051
E2	2.3 ± 0.12	679	0.9230

These values seem to be low if they are compared with available Weibull moduli for some commercial fibers: Nicalon 3-4 [106-108], Fiber FP 4-6 [107-111], Altex 4-6 [112 113], carbon fibers 3-8 [114-117], Nextel 610 and 720 below 10 [118]. However, it has to be taken into account that these are experimental fibers and process development will certainly help eliminate large flaws and increase the tensile strength, as well as the Weibull modulus. This is not surprising, since eliminating large flaws from a population of defects will leave only the small flaws behind. This would narrow the flaw size distribution, resulting in an increased Weibull modulus and tensile strength. The Weibull modulus is an important parameter as far as the description of filament strength is concerned, and is not a material constant. The Weibull modulus can be increased through

the elimination of large flaws during processing of the fibers, which will increase the tensile strength. A high Weibull modulus corresponds to a high σ_0 value and indicates limited scatter in the fracture strength data. In general, this means that weak filaments are absent. Consequently, the average fracture stress increases and hence so does σ_0. It follows that if the average fracture stress approaches the theoretical strength, then the Weibull modulus should become very high. The Weibull modulus determined from the statistics of fracture at one gauge length cannot be used to determine strength at other gauge lengths or for fibers with a different diameter.

In order to improve the mechanical properties of the fibers produced by melt extraction, it is necessary to reduce or eliminate the flaws that are introduced during processing. First at all, the heat source should be modified from oxyacetylene to laser heating to provide a reproducible and controllable temperature and eliminate the gas pressure of the torch that causes instability of the small molten drop. The sharpness of the extracting wheel is another parameter that affects the quality of the fibers. Since a sharp wheel extracts a thinner layer of the ceramic liquid, this would yield smaller diameter fibers with higher strengths, it is necessary to ensure that the edge of the wheel is sharp before extraction experiments, however the copper wheel loses its sharpness very easily. This can be solved by making the extracting wheel in a different material like molybdenum that would keep its sharpness for longer time because of its better wear resistance, but at higher cost. On the other hand, molten yttria-alumina material has shown to have better glass forming tendency by addition of additives or dopants and in

argon atmosphere [119], therefore, the extraction of yttria-alumina fibers under those conditions would enhance the quality of the extracted fibers and their mechanical properties.

4.4 Applications of the Fibers

In general, the melt extracted amorphous and uniform diameter fibers are strong and flexible. However, in the case of crystallized fibers due to rapid grain growth, shrinkage and formation of porosity, the mechanical properties of these fibers drop significantly upon crystallization. Thus, yttria-alumina fibers can only be used for reinforcing glass-ceramic and metal matrices which can be processed and utilized at relatively low temperature (< 940 °C). Some glass-ceramics, such as β-spodumene containing B_2O_3 and TiO_2, can be processed at temperatures lower than 940 °C by using sintering and crystallization heat treatments [120]. Processing of MMCs by reinforcing aluminum alloys are normally done at temperatures lower than 940-950 °C. For example, 4032 [121] and 7075 aluminum [122] alloys have been reinforced with inviscid melt-spun calcia-alumina fiber to produce a MMC using a melt infiltration technique at temperatures of 700 and 927 °C, respectively. The physical properties of the IMS calcia-alumina fibers are: tensile strength of 519 MPa, Young's Modulus of 100 GPa, glass transition temperature of ~ 850 °C, crystallization peak temperature of ~ 980 °C [121, 122]. All the foregoing properties are similar to the yttria-alumina fibers produced by melt extraction in the present study.

Since the amorphous yttria-alumina fibers fabricated by melt extraction were optically transparent, a proposed alternative is in optical applications. It is known that optical fibers doped with lanthanide or transition-metal elements can serve as in-line lasers and amplifiers for fiber-optic telecommunications systems. In general, most current fiber lasers use conventional silica-glass fibers doped with erbium or neodymium. But SiO_2 absorbs strongly in the infrared for wavelengths greater than 4 μm, limiting the infrared range over which such lasers can operate. Some other oxide materials do not absorb significantly until longer wavelengths–the absorption coefficient of crystalline silica at 4 μm is equal to that of yttrium oxide at 7.1 μm and of sapphire at 5.1 μm [123]. Glass fibers made from these materials would therefore expand the range of fiber lasers into the mid-infrared range. But molten oxides that do not contain silica typically have a viscosity that is too low to support fiber-pulling processes. However, melt extraction permits the production of thin ceramic oxides and metallic fibers whose melts are inviscid (low viscosity), such as the yttria-alumina system. The process has been shown to be particularly effective if the molten material of stoichiometric YAG composition is doped with Nd_2O_3 in place of Y_2O_3, with excess Al_2O_3, or from a melt doped with Er_2O_3 in the presence of excess Al_2O_3; and it should also work with several other dopants, because molten oxides are good solvents for these elements. These fibers have the potential to extend the operating range of oxide glass-fiber lasers in photonic applications [119].

CHAPTER 5

CRYSTALLIZATION BEHAVIOR AND KINETICS

This chapter describes the crystallization of the amorphous melt extracted fibers, and focuses on the phase and microstructural development as a function of temperature after heat treatment.

5.1 Study of Phase Development

The extracted fibers were crushed and heated, at 10 °C/min to various temperatures, namely: 800, 850, 900, 1000, 1300, 1400 and 1500 °C for 1 h.

XRD patterns of E1 fibers heat-treated below 1000 °C (Figure 5.1) displayed no devitrification. The crystallinity of YAG and α-alumina became obvious as the temperature was raised to 1300 °C and the fibers show only minor changes at higher temperature.

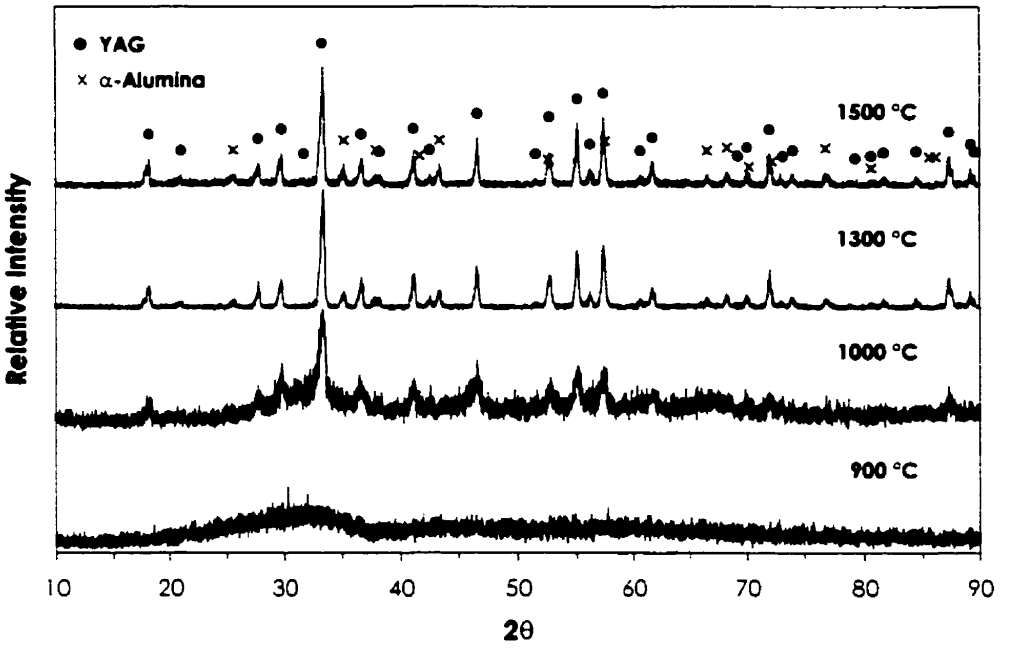

Figure 5.1 XRD patterns of E1 fibers heat-treated for 1 h at different temperatures. YAG peaks indexed by JCPDS card 33-40 and α-alumina peaks by JCPDS card 10-173.

X-ray analysis of the fibers of the Y_3A_5 composition after heat treatment revealed that they remained amorphous to x-rays up to 800°C, and the crystallization of the pure garnet phase, YAG, begins above this temperature (Figure 5.2) and at 900 °C, it transforms directly to YAG with no intermediate phases. X-ray diffraction studies show that crystallization occurs over a narrow temperature range. At 800 °C a broad peak is observed, indicating that the sample is still amorphous. However, after only 60 minutes at 850 °C the YAG phase begins to appear and is fully crystallized by 900 °C. Further heating of the fibers up to 1500 °C showed no change in phase composition except for an increase in the intensity of the peaks. XRD results also indicated no second phase in Y_3A_5 fibers. It has been reported that YAG is the most stable phase in the Y_2O_3-Al_2O_3 system.

Single crystals and both fused and sintered samples are stable during cooling, in use at room temperature and on annealing at temperatures below the melting point [74].

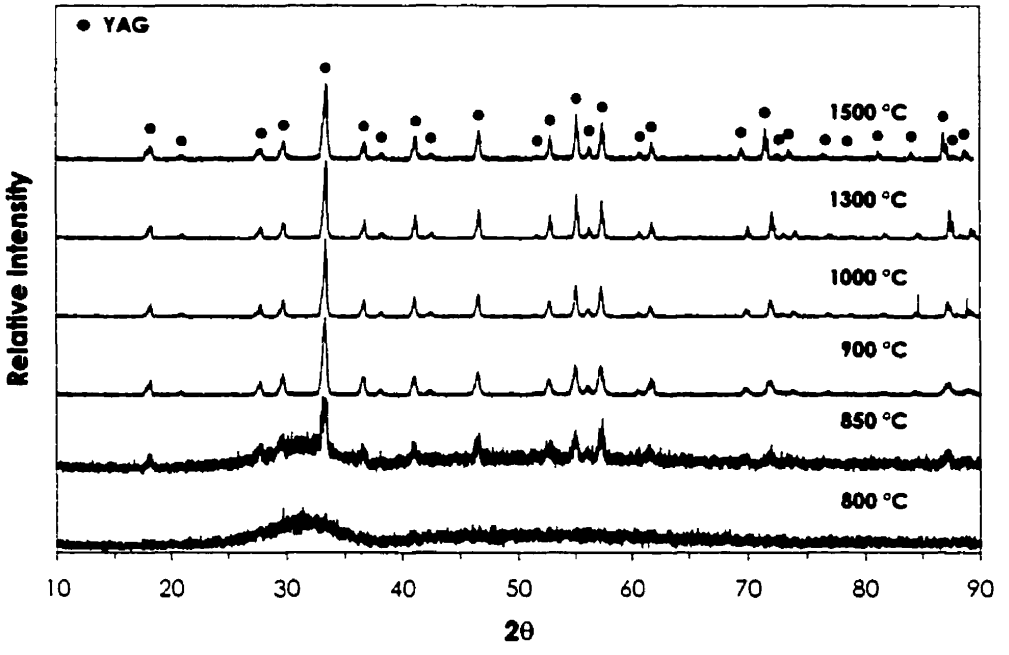

Figure 5.2 XRD patterns of Y_3A_5 fibers heat-treated for 1 h at different temperatures.

The phase development of E2 fibers, as shown in Figure 5.3, occurs gradually during heating. The crystallization of cubic YAP began at 850 °C, and the appearance of orthorhombic YAP phase is evident at 1400 °C. Moreover both phases, YAP orthorhombic and YAG, coexisted as a major phases at 1500 °C. In addition, there was a color change in the E2 fibers from white to yellowish with the formation of YAP orthorhombic.

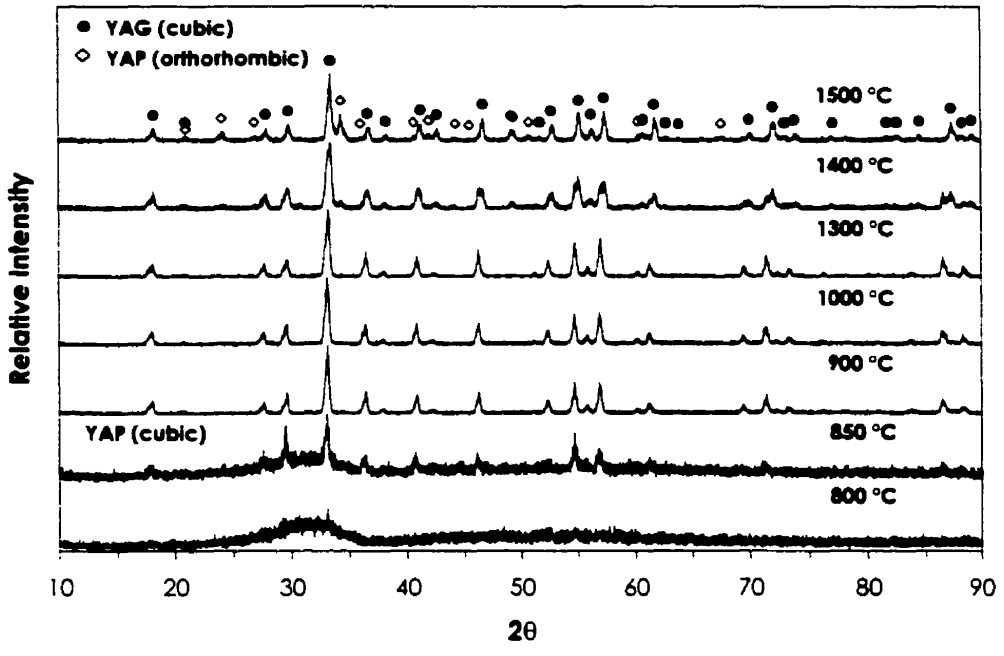

a)

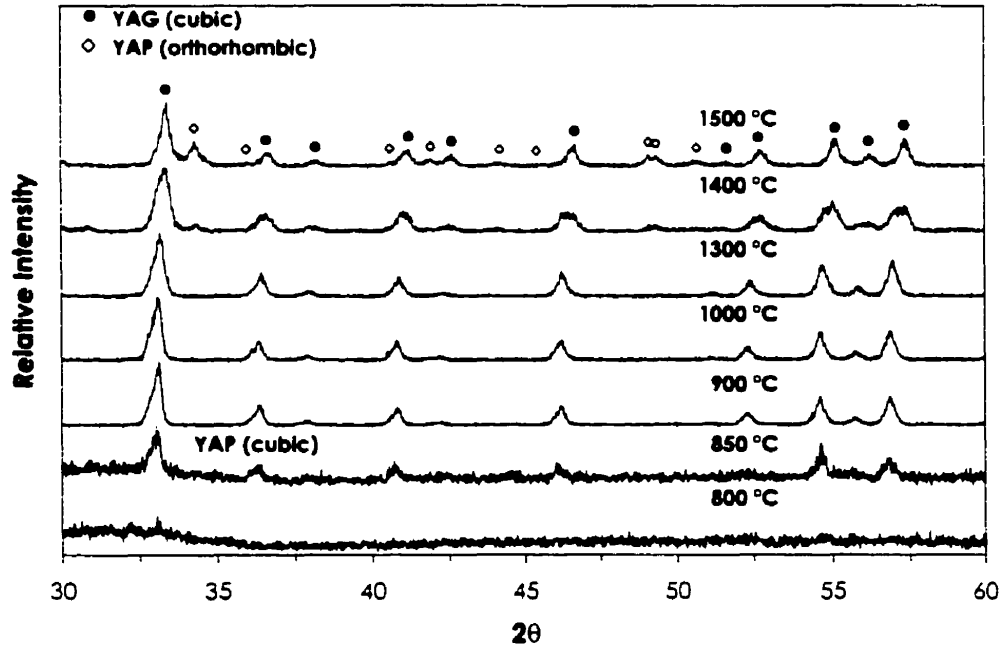

b)

Figure 5.3 XRD patterns of E2 fibers heat-treated for 1 h at different temperatures. Cubic YAP peaks indexed by JCPDS card 38-222 and orthorhombic YAP peaks by JCPDS 33-41.

5.2 Microstructure of Crystallized Fibers

In determining the grain growth at high temperature, the yttria-alumina fibers were placed in alumina crucibles and heat-treated at 1500 °C for 1, 2, 4 and 8 h. The microstructural development and morphology of the heat-treated glass fibers was then observed by scanning electron microscopy to examine the grain growth behavior. Figures 5.4-5.6 show SEM micrographs of the thermally etched surface of the Al_2O_3-Y_3A_5 eutectic, Y_3A_5 and Y_3A_5-YA eutectic fibers, respectively. From the photomicrographs, it can be seen that there is an increase in grain size with heat treatment time. An obvious change brought about by heat treatment is the conversion of the transparent glass fiber to an opaque polycrystalline material. The opacity of the crystallized fibers is due to light scattering at interfaces between adjacent crystals and any residual glass phase as a result of the differences in refractive indices of the phases. In addition to the obvious change in appearance, there is another change, which is only apparent when the materials are examined at high magnifications. Clearly, heat treatment produces a generally undulating surface made up of rounded crystals boundaries and occasionally there are angular crystals, which project above the mean surface level. Examination by SEM reveals that fiber surfaces are no longer smooth compared with the parent glass fibers. Figure 5.7 shows the yttria-alumina fibers crystallized at 1500 °C for 8 hours. It can be clearly seen that they are nanocrystalline with a grain size in the order of 100-500 nm, except in the case of E2 fibers, which have a grain size of 1-2 μm. Moreover the phases formed for each composition are according to the equilibrium phase diagram.

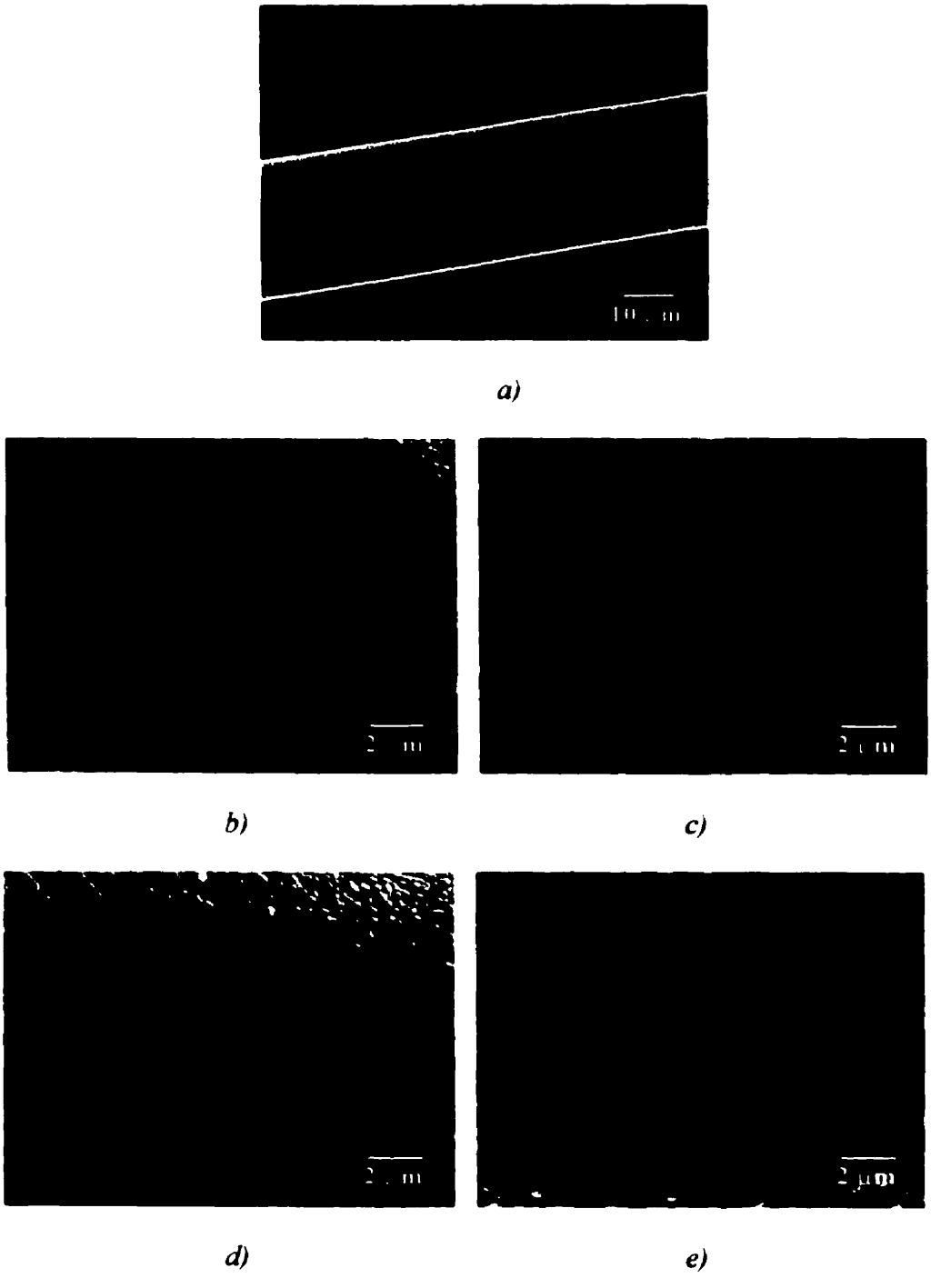

Figure 5.4 The SEM micrographs of the Al_2O_3-Y_3A_5 eutectic glass fibers: (a) morphology of the fibers before heat treatment: (b), (c), (d), (e) grain growth of thermally treated fibers at 1500 °C for 1, 2, 4 and 8 h, respectively.

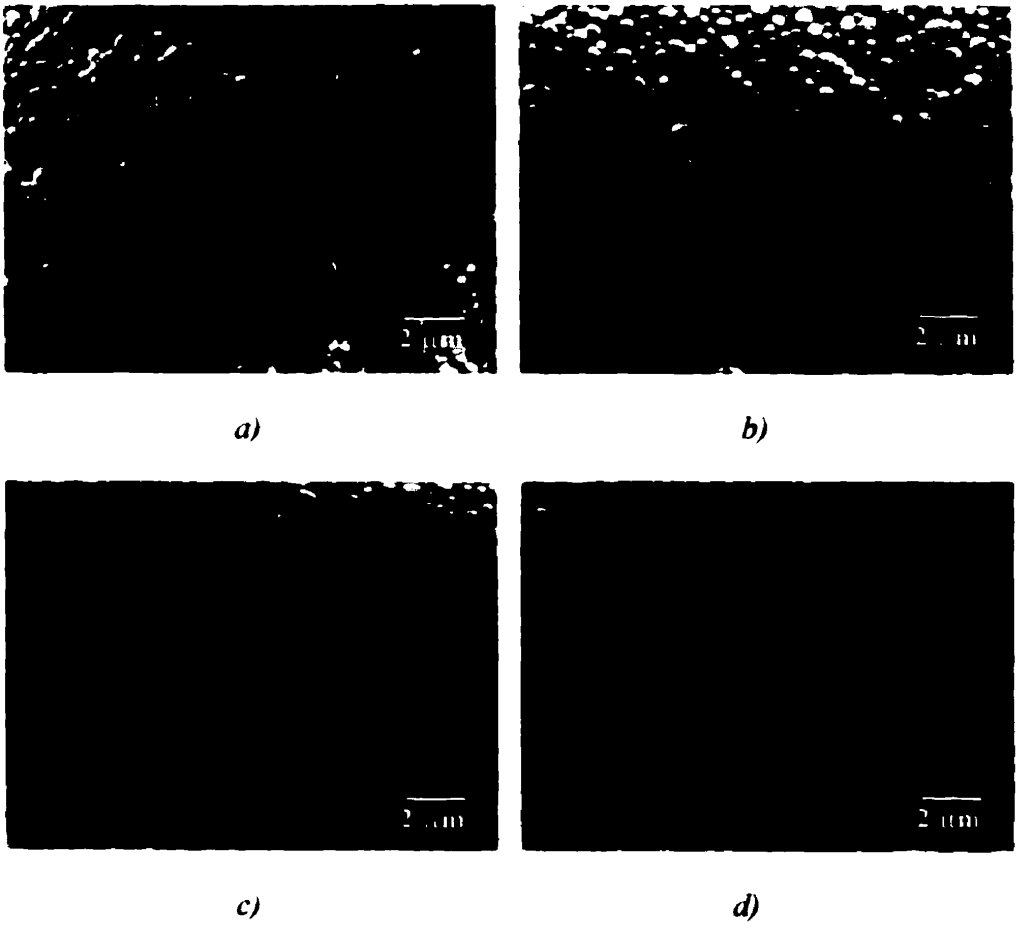

a) *b)*

c) *d)*

Figure 5.5 The SEM micrographs of the Y_3A_5 glass fibers: (a), (b), (c), (d) grain growth of thermally treated fibers at 1500 °C for 1, 2, 4 and 8 h, respectively.

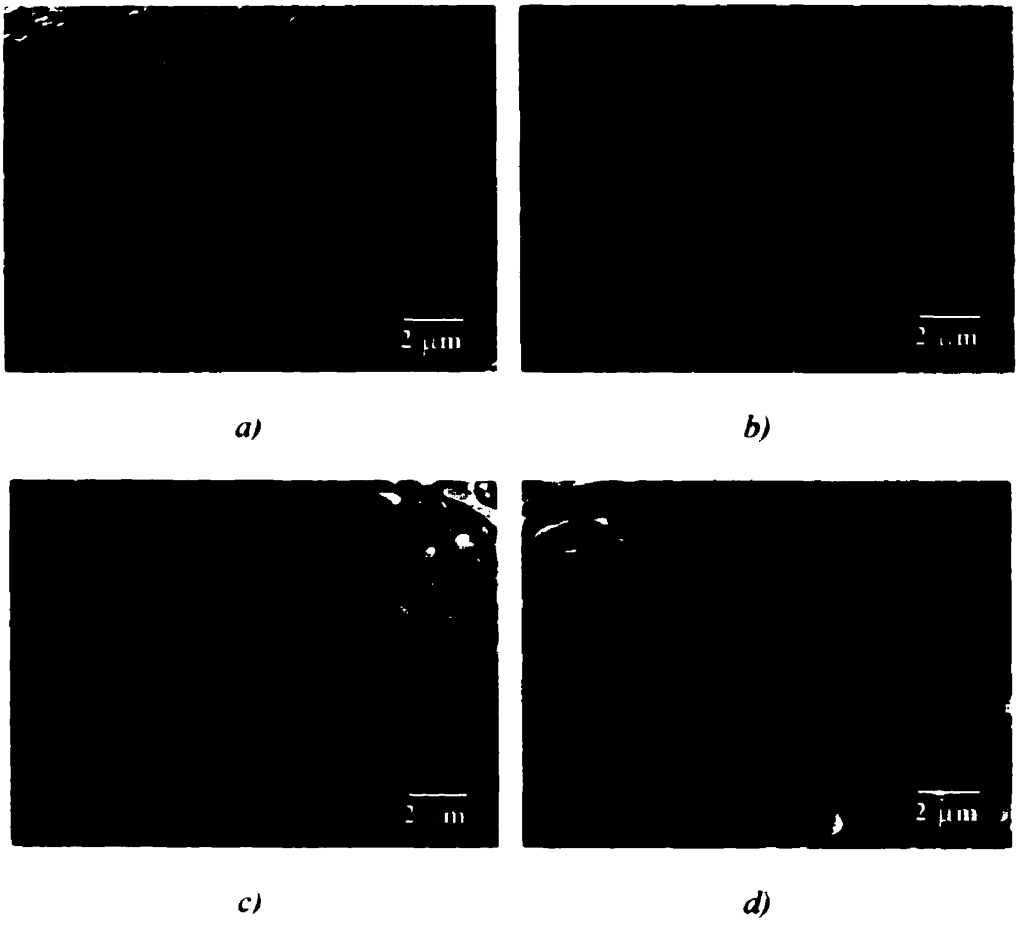

Figure 5.6 The SEM micrographs of the Y_3A_5-YA eutectic glass fibers: (a), (b), (c), (d) grain growth of thermally treated fibers at 1500 °C for 1, 2, 4 and 8 h, respectively.

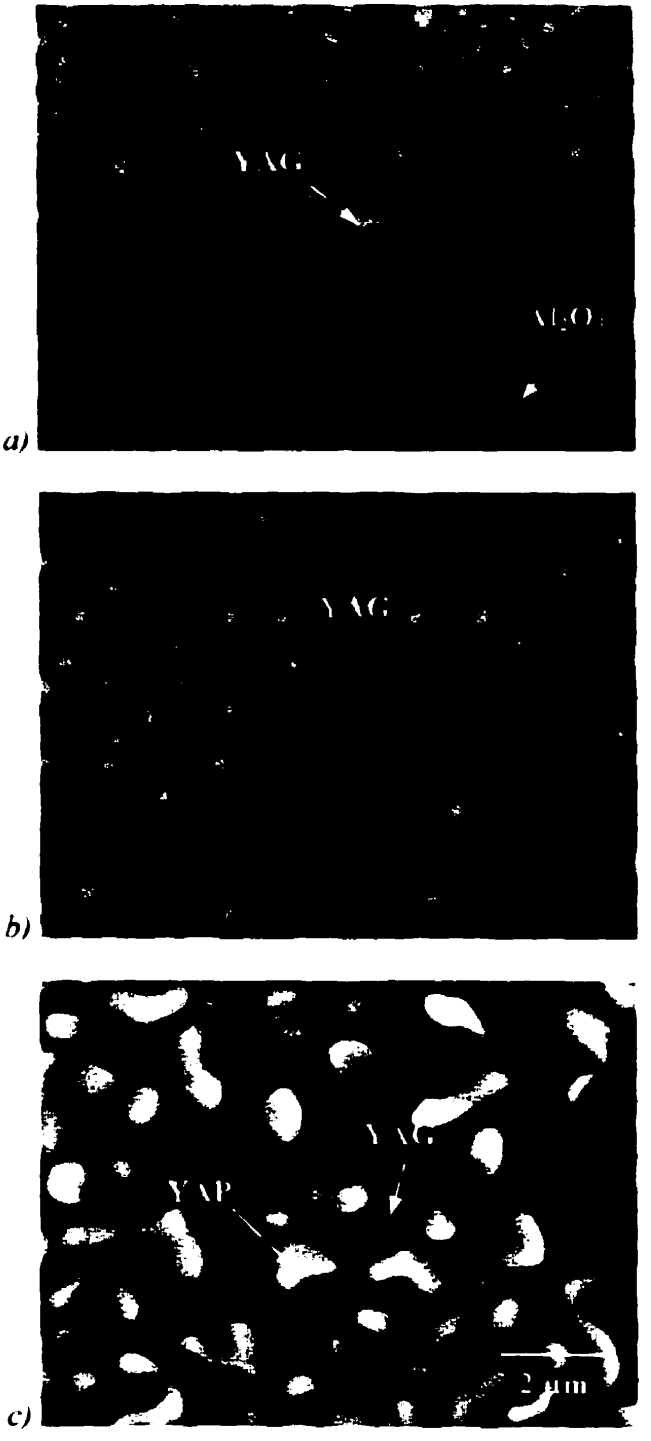

Figure 5.7 SEM micrographs of crystallized yttria-alumina fibers fired at 1500 °C for 8 hours. (a) E1. (b) Y_3A_5 and (c) E2.

5.3 Lattice Parameter Measurement

Lattice parameters of YAG, cubic YAP and orthorhombic YAP phases developed during heat treatment of yttria-alumina fibers were determined by Cohen's method [124]. An extensive explanation of the Cohen's Method is presented in Appendix B.

Table 5.1 Lattice parameters calculated by Cohen's method for the phases developed in glass fibers after heat treatment.

Compound	Lattice Parameter, Å	JCPDS card
YAG		**# 33-40**
E1 (1500 °C, 1h)	12.0130	12.0089 (3)
Y_3A_5	12.0054	
E2	12.0197	
Cubic YAP		**# 38-222**
E2 (900 °C, 1h)	12.0545	12.107
Orthorhombic YAP		**# 33-41**
E2 (1500 °C, 1h)	a = 5.3917	a = 5.3286 (4)
	b = 7.4652	b = 7.3706 (5)
	c = 5.2481	c = 5.1796 (3)
YA (1500 °C, 2h)	a = 5.2864	
	b = 7.3351	
	c = 5.1627	

Table 5.1 shows the calculated values of lattice parameters for the YAG phase formed after 1h heat treatment at 1500 °C for E1, Y_3A_5, and E2; cubic YAP phase

crystallized after 1h heat treatment at 900 °C in E2; and this is finally transformed to orthorhombic YAP phase after 1h heat treatment at 1500 °C in the case of E2. These values are in good agreement with the values reported in the literature, and this confirmed the existence of the phases identified in the XRD patterns.

5.4 Discussion of Devitrification Behaviour of As-Extracted Fibers

Devitrification of yttria-alumina glasses is of both scientific and practical interest. Crystallization of these glasses could plausibly yield a small grain size, pore-free, fracture resistant material with a high degree of chemical and microstructural homogeneity.

The DSC results revealed devitrification of the amorphous fibers in the range of 939-949 °C. When the glass transition and crystallization temperatures for Y_3A_5 fibers are compared with those of the E1 and E2, it seems that excess of Al_2O_3 slightly increases T_g and T_c, whereas these two temperatures were lowered by the presence of excess of Y_2O_3. It appears that the Y_2O_3 in the amorphous yttria-alumina fibers enhances crystallization, therefore, the glass transition and crystallization of the E2 fibers are both accelerated in comparison with the same transformations for E1 fibers. In addition, extensive grain growth occurred for the E2 fibers during heat treatment, as it can be seen in Figure 5.7 for a heat treatment at 1500 °C for 8 hours, and this is another indication of the effect of Y_2O_3 on the acceleration of devitrification.

Furthermore, devitrification causes a volume change, which can be associated with the formation of porosity and other defects, as illustrated in Figure 5.5(a) for the Y_3A_5 fiber. Such fibers become very brittle, and exhibit lower tensile strengths, which makes handling and further processing more difficult.

The Al_2O_3-Y_3A_5 eutectic glass (E1) is stable over a wide range of temperatures. Upon heating, crystallization occurs first by the emergence of YAG at 949 °C. One may make plausible suggestions as to the possible crystallographic phases of Al_2O_3, which may nucleate from this glass composition based on the results of rapid solidification studies of pure Al_2O_3, for which several metastable phases have been reported. In plasma sprayed Al_2O_3, δ, γ, and θ phases have all been found [125], and splat-quench has yielded the δ, γ and α phases [126]. For sol-gel processing of Al_2O_3, heating the gels results in the successive appearance of $\gamma \rightarrow \delta \rightarrow \theta \rightarrow \alpha$ polymorphs [127]. Annealed amorphous alumina films obtained by direct vaporization of Al_2O_3 onto a glass substrate yielded γ- and δ-alumina as the principal intermediate forms before the appearance of α-Al_2O_3. However, θ-Al_2O_3 was encountered as a minor constituent [128].

The first Al_2O_3 phase to appear is δ-Al_2O_3 which is a well-ordered super spinel structure. This was the only metastable Al_2O_3 phase detected. γ-Al_2O_3 is a disordered spinel and is stable over a lower temperature range than the δ-phase. Since the γ-phase was never observed upon crystallization, it is likely that this phase only forms for quenched-in material rather than being nucleated from a glass. The θ-phase is another

cubic polymorph, which has been reported for rapidly quenched Al_2O_3. The θ-phase is stable between the δ and α phases upon heating. Rooksby [129] reports that well crystallized δ-Al_2O_3 converts directly to α-Al_2O_3 upon heating instead of passing through the θ-phase. The δ-phase is not as dense as the equilibrium α-Al_2O_3 structure and could possibly accommodate more impurity atoms.

The crystallization of Y_3A_5 fiber composition occurred at 942 °C yielded pure YAG with no intermediate phases according to the DSC scan, and was stable up to 1500 °C. This temperature is low compared with the temperature of formation of YAG phase by other processes such as mixed ceramic powders (1650 °C) and sol-gel (1200 °C) techniques [16], respectively, and it can be attributed to the homogeneity achieved during melting and extraction of the glass fiber. Solid-state diffusion of Y^{3+} and Al^{3+} is necessary for nucleation and growth of YAG phase. The effective diffusion distance required for this process depends upon the spatial scale of homogeneity. The greater the diffusion distance between the reacting species, the larger the diffusivity must be for rapid transformation to single YAG, thus requiring higher temperature. The scale-of-mixing argument is based on the effect of the relative size and distribution of the aluminum and yttrium on diffusional processes. The crystallization temperature and degree of reaction should vary continuously with diffusion distance. As it was pointed out previously, the compositional analysis performed by EPMA and ICP-AES on the extracted fibers showed that they were homogeneous between the core and edge, and the actual composition was very close to the values of the starting powder mixtures.

In the crystallization sequence of Y_3A_5-YA eutectic glass (E2), the material was found to be amorphous up to 800 °C for 1 h. The first crystalline phase to appear is cubic YAP at 939 °C, introducing the only identifiable exothermic peak in the DSC. Then, cubic YAP transforms to orthorhombic YAP and YAG at 1400 °C. The presence of these phases was confirmed by XRD and measuring the lattice parameters of the phases formed after heat treatment, and these are in good agreement with literature values. Furthermore, there was a color change in the E2 fibers from white at 900 °C and 1 h heat treatment to yellowish at 1400 °C and 1 h heat treatment, which is due to the development of orthorhombic YAP phase. According to the JCPDS index cards of cubic YAP and orthorhombic YAP (38-222 and 33-41, respectively), cubic YAP was produced by heating at 1060 °C and quenched; whereas orthorhombic YAP was obtained by heating at higher temperatures of 1675 °C. This means that cubic YAP is stable up to relatively low temperature whereas orthorhombic YAP is stable a higher temperatures.

Various metastable phases for YAP have been reported in the literature. Abell *et al.* [74] studied powdered YAP annealed at temperatures above 1300 °C. They noted a slow decomposition of the surface into two phases, one being the garnet phase, YAG, and the other remained unidentified but there is strong evidence that it was a unknown phase from the pseudo-binary system. The deduction ensued that the surface decomposition must be associated with the loss of one or more elements which moved the composition away form the pseudo-binary axis. Oxygen loss seemed an obvious mechanism but attempts to cause decomposition by the use of vacuum or a reducing atmosphere proved

to be ineffective, although remelting decomposed material in an oxygen atmosphere regenerated the YAP phase. The presence of X along with YAG, was only observed in melts with compositions Y_2O_3:Al_2O_3 = 45:55, YA (1:1) and Y_2A (2:1).

Yamaguchi *et al.* [130] identified an hexagonal YAP polymorph from Y_2O_3:Al_2O_3 = 1:1 starting powder that crystallized at 870-900 °C; and was only observed up to 1000 °C. Whereupon it was transformed to the cubic form between 1000 and 1060 °C. A specimen heated at 1060 °C showed the presence of the cubic form having a garnet structure whose ideal formula is $Y_3Al_5O_{12}$ ($Y_3Al_2(AlO_4)_3$). Keith and Roy [131] reported that an equimolar mixture of Y_2O_3 and Al_2O_3 produced a phase with the same structure at 1600 and 1700 °C and suggested that this indicates a solid solution of the type $Y_3AlY(AlO_4)_3$ = $YAlO_3$. Besides, the results suggested that the garnet structure is tolerant not only to Al^{3+} in both six-fold and four-fold coordination [132] but also to replacement of half of the six-coordinated aluminum by yttrium, as represented by the formula $Y_3AlY(AlO_4)_3$. According to the data of Keith and Roy [131] the cubic form transforms into the orthorhombic modification after heating for 2 h at 1800 °C. The cubic form decomposed into YAM and YAG at 1080-1200 °C. After completion of the decomposition, the orthorhombic modification was formed by solid-state reaction between both compounds. Single-phase orthorhombic YAP was obtained by heating for 1 h at 1650 C. The hexagonal YAP solid solutions were formed between 50 and 62.5 mol% Al_2O_3.

The perovskite structure is a close-packed lattice with the general formula ABX_3. Almost all the known rare earth perovskites are oxides with the rare earth ion occupying the A sites. Since most of the rare earth ions are stable only in the trivalent state, the valence relationship is $A^{3+}B^{3+}O_3$. The truly cubic structure is referred to as "ideal perovskite". In this structure the B (Al^{3+}) ion is in octahedral coordination and the A cation (Y^{3+}) in twelvefold coordination with the oxygen ions. The simple cubic structure is shown in Figure 5.8(a). Alternatively, the A cation may be thought of as being in the body center position and the B cation at the corners, in which case oxygens would occupy the center of the edges of the cube, as shown in Figure 5.8(b). The basic building blocks of the perovskite structure are the oxygen octahedra. When these octahedra share corners

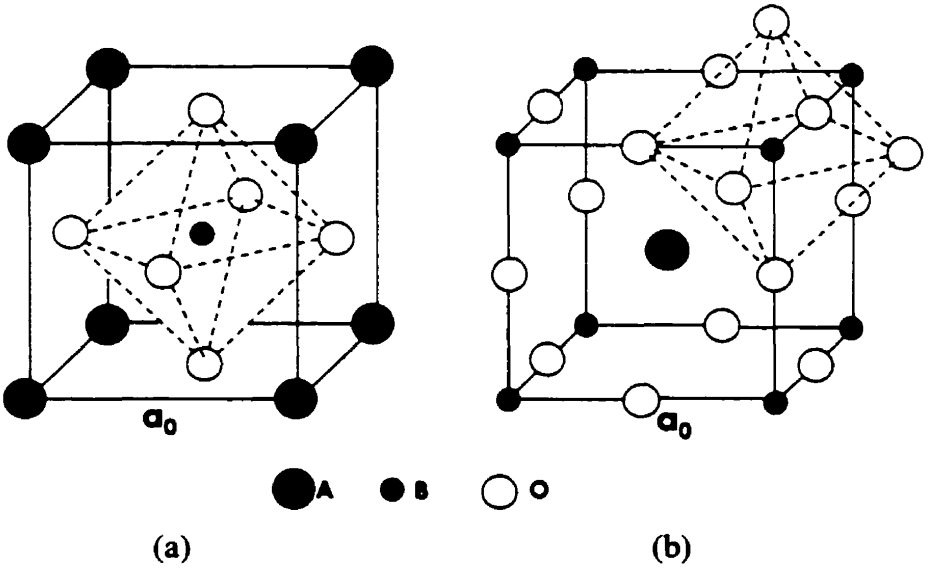

Figure 5.8 Two methods of representation of an ideal perovskite structure. The octahedral symmetry of the B ions is shown.

cubic stacking is obtained, while the sharing of faces leads to hexagonal stacking. Thus the prerequisites for a perovskite structure are corner-shared octahedra containing a small B cation in octahedral coordination with a relatively large A cation in the interstices of the framework of the octahedron.

Distortions from the ideal ABO_3 cubic symmetry occur frequently, especially in rare earth perovskite oxides, and structures with tetragonal, orthorhombic, rhombohedral, monoclinic and triclinic symmetry are known. The number of compounds reported to have tetragonal, monoclinic or triclinic structures is few and detailed structural characterizations have not been carried out in most cases. On the other hand, examples of the orthorhombic and rhombohedral structures are numerous.

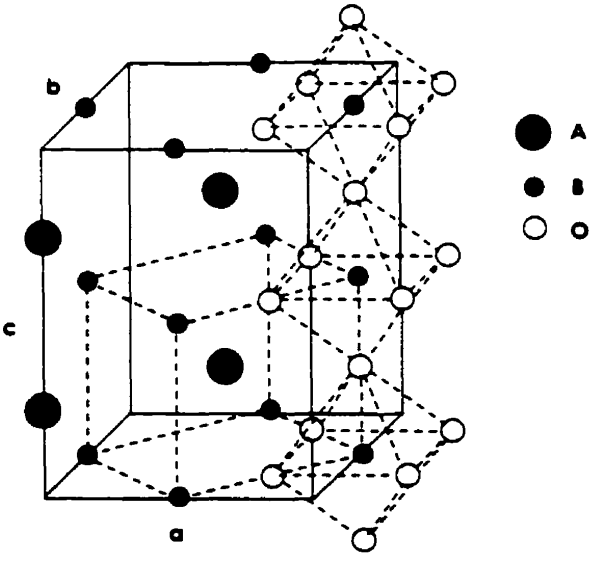

Figure 5.9 Orthorhombic distortion of the perovskite structure where the relationship to the ideal structure is shown.

In the rare earth perovskites, compounds with an orthorhombic distortion are the most common. This distorted perovskite form, shown in Figure 5.9, is obtained by tilting of the oxygen octahedra in such a way that the A atoms are displaced along $\langle 1\bar{1}0 \rangle$ pseudocubic directions, or $\langle 010 \rangle$ directions in the orthorhombic cell [133].

5.5 Determination of the Nucleation Rate

Knowing the nucleation rate at different temperatures for glass-forming melts has both scientific and technological importance, especially, the temperature where the nucleation rate is a maximum. These data are important to understanding the stability of a glass for practical applications where the formation of nuclei and their subsequent growth to crystals must be avoided (such as in optical fibers, laser glasses, optical switching glasses), as well as to preparing glass-ceramics with desired microstructures by controlled nucleation and crystallization.

The technique commonly used to determine the nucleation rate is to heat the glass at a certain temperature for a selected period of time, thereby developing nuclei within the glass. The glass is then heated to a higher temperature for a short time where detectable crystals grow on the nuclei. If it is assumed that each crystal grows from a single nucleus and no new nuclei are formed or dissolved during crystal growth, the number of nuclei per unit volume of glass can be determine by counting the number of crystals in a given volume. The nucleation rate is determined at different temperatures by repeating this same procedure at various temperatures and times.

However, there is a method for determining the temperature of maximum nucleation, which is much faster than the method described previously. The analysis uses a different parameter, namely, the height of the DTA crystallization peak, which is believed to better represent the concentration of nuclei present in a glass.

It is well known that the nucleation rate (number of nuclei formed per unit volume per second) is a function of temperature and becomes maximum at a temperature near the middle of the temperature range where nucleation can occur (see Figure 2.21 in section 2.7.1 of the Literature Review). The number of nuclei developed in a particular volume of a glass at different temperatures will have a temperature dependence identical with that of the nucleation rate curve, provided the nucleating time at each temperature is the same. Consequently, the height of the DTA crystallization peak $(\delta T)_p$, which should be proportional to the concentration of nuclei in the glass, is expected to have a nucleation-rate-like shape when plotted as a function of nucleating temperature.

It has been recently demonstrated [134-136] that a properly designed non-isothermal DTA/DSC experimental procedure can be used to determine the temperature range for nucleation and the relative nucleation rate at different temperatures (including the temperature for maximum nucleation) for a glass. In this technique, either the inverse temperature for the DTA/DSC crystallization peak, $1/T_p$, or the height of the peak at T_p, $(\delta T)_p$, is plotted as a function of the nucleation temperature, T_p. The main value of this

technique is the rapidity whereby the nucleation rate curve of a glass can be determined from non-isothermal DTA/DSC.

Figures 5.10 and 5.11 show how $(\delta T)_p$ varies for the yttria-alumina glass fibers when nucleated at the temperatures for 2 h. The temperature of the maximum for each curve is ~ 650 °C for first and second crystallization events in E1, and ~ 800 °C for Y_3A_5 and E2 fibers. As shown in Figure 5.10, no appreciable change in $(\delta T)_p$ occurs for this glass fibers after they are nucleated at ≥ 700 °C. This suggests that final concentration of nuclei present in the glass remains constant above 700 °C. The temperature range for nucleation were ~ 600-700 °C for both crystallization events in E1 fibers and ~ 700-850 °C for Y_3A_5 and E2 fibers. Although further investigation on nucleation has to be done in order to have more precise values.

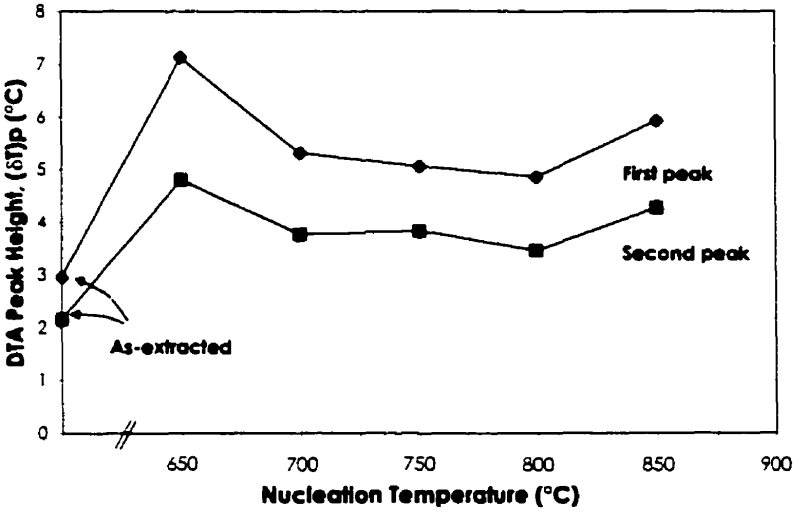

Figure 5.10 Height of the DTA crystallization peak, $(\delta T)_p$, for the Al_2O_3-Y_3A_5 eutectic glass fibers as a function of nucleating temperature for 2 h.

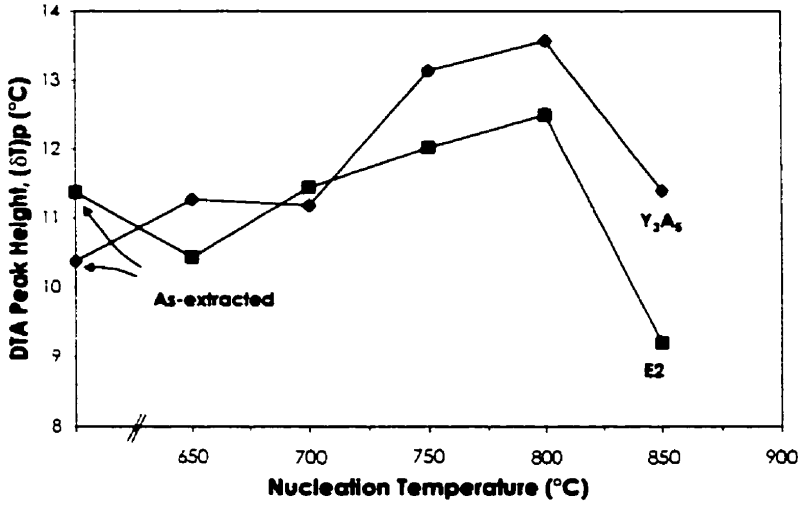

Figure 5.11 Height of the DTA crystallization peak, $(\delta T)_p$, for Y_3A_5 and Y_3A_5-YA eutectic glass fibers as a function of nucleating temperature for 2 h.

The DTA method provides a rapid way of determining the temperature corresponding to maximum nucleation for a glass. Since the change in the DTA peak height for glasses nucleated at different temperatures is assumed to change with the nuclei concentration, it is believed that a relationship can be established between $(\delta T)_p$ and the concentration of nuclei, and eventually the nucleation rate at different temperatures.

5.6 Kinetics of Crystallization

The crystallization of Y_2O_3-Al_2O_3 fibers was followed by differential thermal analysis (DTA). The usual method of obtaining kinetic data on glasses involves a series of experiments carried out under isothermal conditions at different temperatures. This

process is laborious and considerable interest exists in the study of reaction kinetics by a dynamic method such as DTA. The principle of the continuous heating method assumes that ΔT (the temperature difference between the sample and the standard) is proportional to the crystallization rate.

The activation energy values for crystallization were calculated using both the Kissinger [137, 138], and Augis-Bennett [139] equations by measuring the variation of the peak temperature in the differential thermal patterns with heating rate. Kissinger demonstrated how activation energy and frequency factor could be calculated from DTA experiments for the case of homogeneous solid-state reactions following first order kinetics. For that, the decomposition of clay minerals of the kaolin group was used in the study of the relation of chemical kinetics and DTA. An extension of the Kissinger method, applicable to heterogeneous solid-state reactions and described by an Avrami expression, was derived by Augis-Bennett. This new method allowed the study of the kinetics of metallic reactions at higher temperature using DTA, such as the transformation kinetics of the metastable equiatomic tin-nickel alloys.

Figure 5.12 shows the DTA thermograms as a function of heating rate for the three ceramic oxide fiber compositions. It can be seen that the faster the scan speed, the higher the peak temperatures, T_p, and the larger the peak heights, $(\delta T)_p$, and the width at half-peak maximum (peak width), $(\Delta T)_p$, become. A high rate of heating will cause dH/dt to increase because more of the reaction will take place in the same interval of time, and

therefore the height or the apex, and the differential temperature, ΔT, will be greater. Since the return to the baseline is a time function, as well as a temperature-difference function, the return will occur and shift to a higher actual temperature with increasing heating rate (ϕ, °C/min) [140]. A shift in the peak temperatures is observed indicating the effect of heating rate on the crystallization kinetics. The area under a DTA peak (ΔT x time) is directly proportional to the heat of reaction. The peak area measured as ΔT *vs.* time is constant and independent of the heating rate. The heating rate affects only peak width and height as well as peak temperature. On the curve for temperature difference against time, slow heating rates give broad shallow peaks while fast rates give narrow sharp ones and peak areas are not affected (Figure 5.13). When plotting DTA curves in the usual manner, namely, ΔT *vs.* sample temperature, then the area will be proportional to the heating rate if this remains constant during the reaction. On these curves, the peaks vary considerably in area, and those obtained with slow heating rates are much smaller and sharper than those with fast heating rates (Figure 5.12) [141, 142].

Table 5.2 summarizes the crystallization peak temperatures as a function of heating rate for E1, Y_3A_5 and E2 fibers.

Therefore, Kissinger proposed the following relationship:

$$\ln\left(\frac{\phi}{T_p^2}\right) = -\frac{E_{ct}}{RT_p} + const. \qquad (5.1)$$

where E_{ck} is the activation energy for crystallization estimated by the Kissinger method (kJ/mol), T_p is the absolute crystallization peak temperature (K) and R is the gas constant. The constant in Equation 5.1 is equal to $\ln(Rk_0/E_{ck})$where E_{ck} and k_0 are constants and are properties of the material. The constant E_{ck}, called the activation energy, is often interpreted as the energy barrier opposing the reaction or transformation. The constant k_0, most often called the frequency factor, is a measure of the probability that a molecule having energy, E_{ck}, will participate in a reaction or transformation.

Table 5.2 Variation of the crystallization peak temperatures (T_p) of the as-extracted Y_2O_3-Al_2O_3 fibers according to the DTA scan rates.

Peak Temperatures, T_p (°C)				
ϕ, °C/min	**E1, first peak**	**E1, second peak**	**Y_3A_5**	**E2**
3	922.7	1018.9	-	-
5	928.0	1024.9	-	-
10	936.0	1031.2	-	-
20	948.6	1039.7	-	-
30	-	-	948.2	947.8
40	959.5	1047.3	955.8	952.4
60	-	-	970.3	963.2
80	975.9	1051.0	979.1	973.3
100	-	-	984.3	980.0

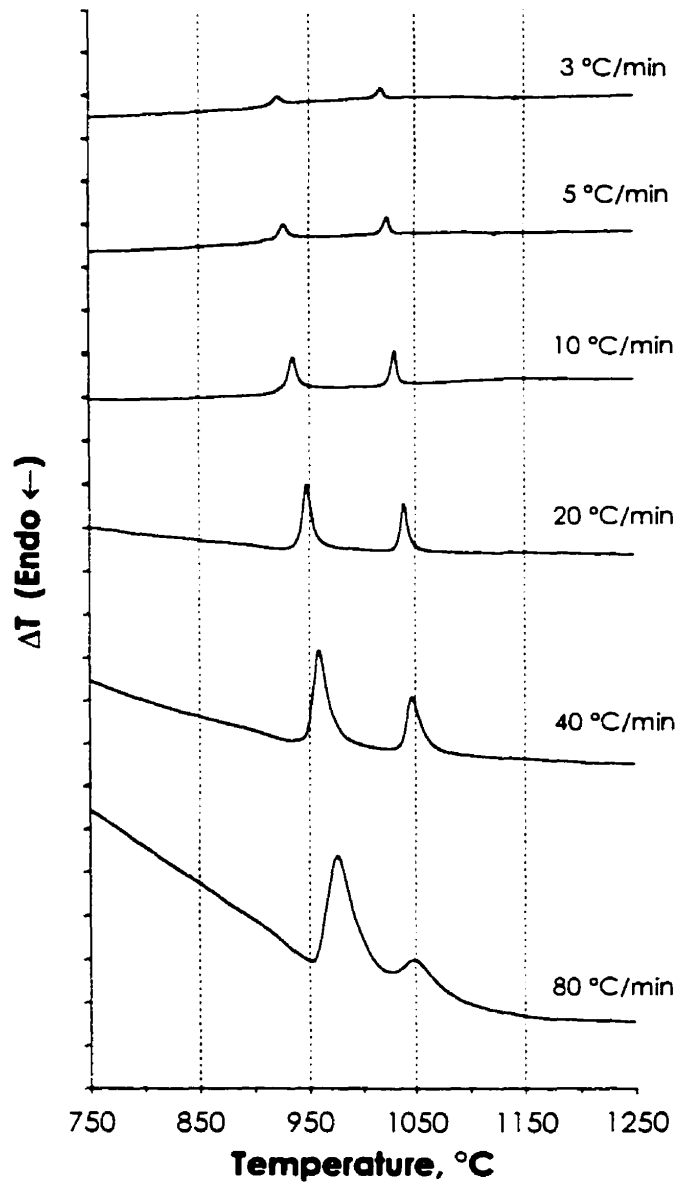

Figure 5.12(a) DTA curves for melt extracted E1 fibers at various heating rates.

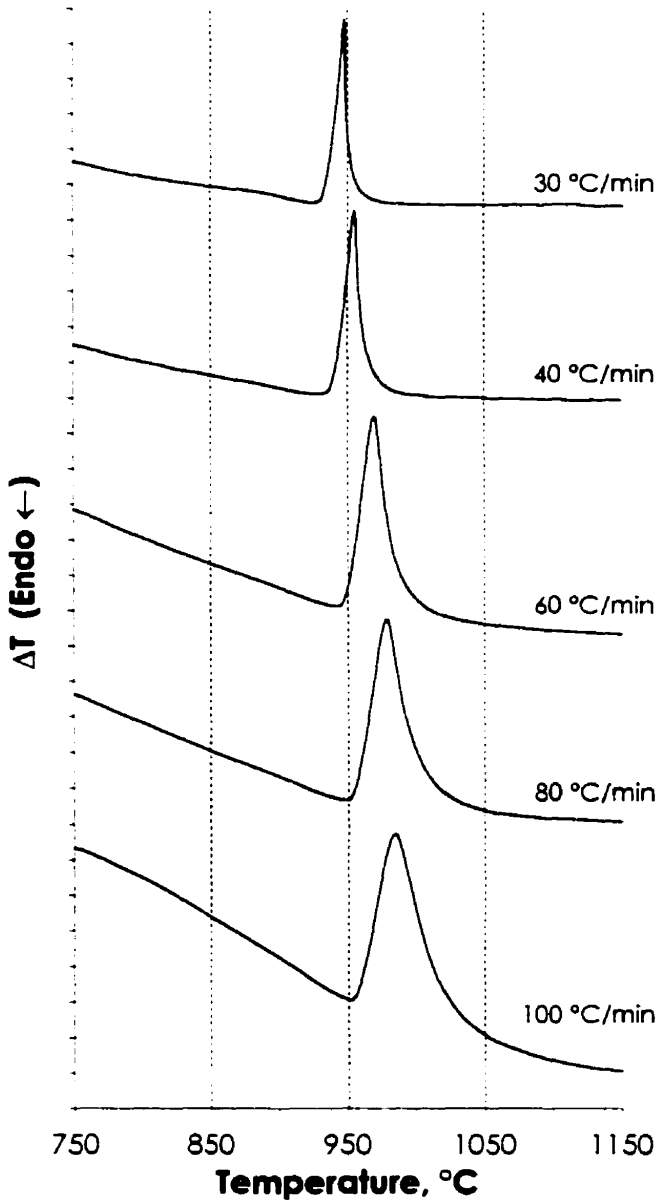

Figure 5.12(b) DTA curves for melt extracted Y_3A_5 fibers at various heating rates.

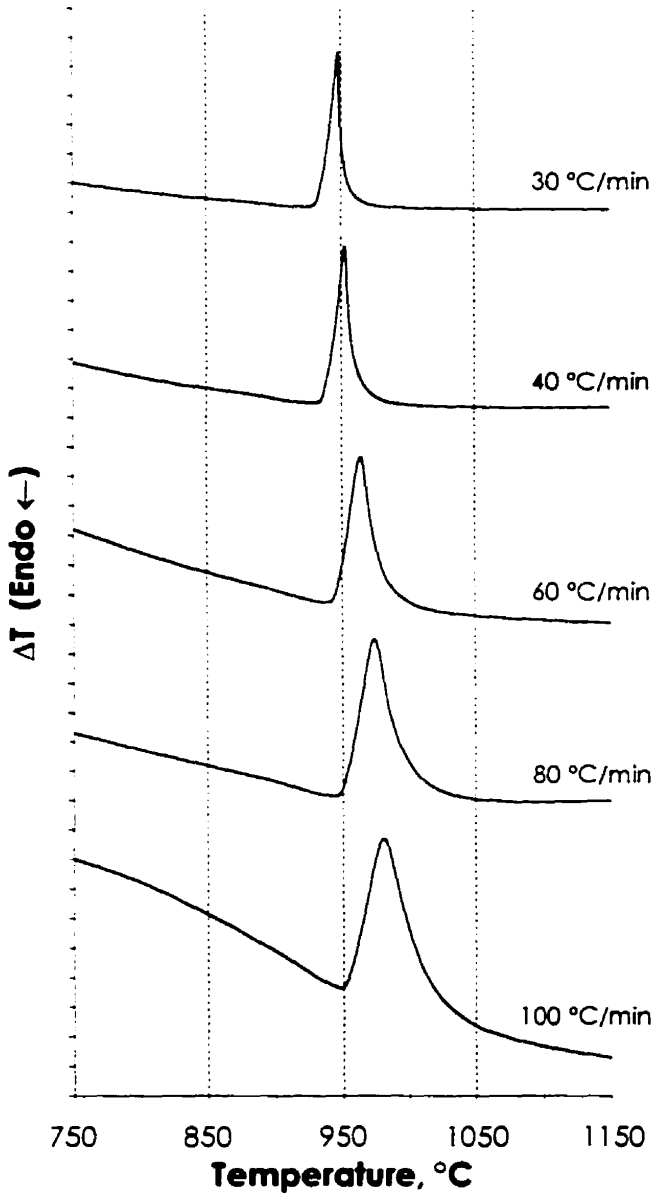

Figure 5.12(c) DTA curves for melt extracted E2 fibers at various heating rates.

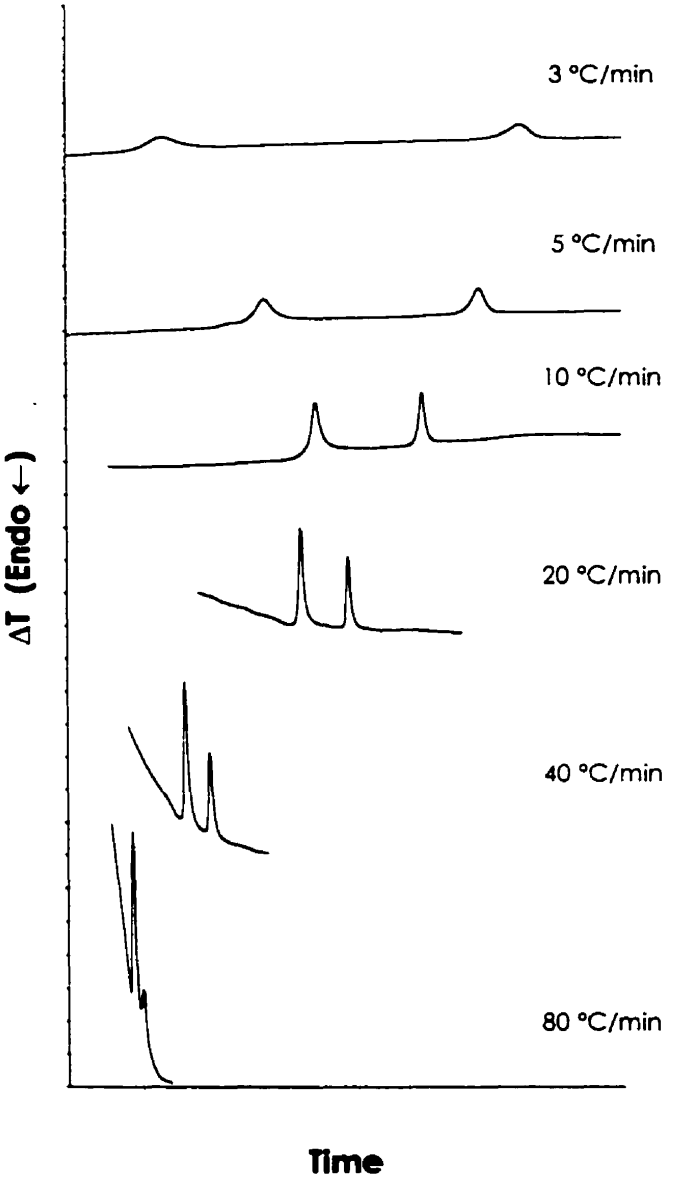

Figure 5.13 DTA scans as a function of time for E1 fibers at various heating rates.

From the slope of the plot of ln (ϕ/T_p^2) vs $1/T_p$, E_{ck} value was determined as 741 kJ/mol and 1374 kJ/mol for first and second crystallization events, respectively, in the Al_2O_3-Y_3A_5 eutectic fibers, and 390 kJ/mol and 438 kJ/mol for Y_3A_5 and Y_3A_5-YA eutectic fibers, respectively (Figure 5.14).

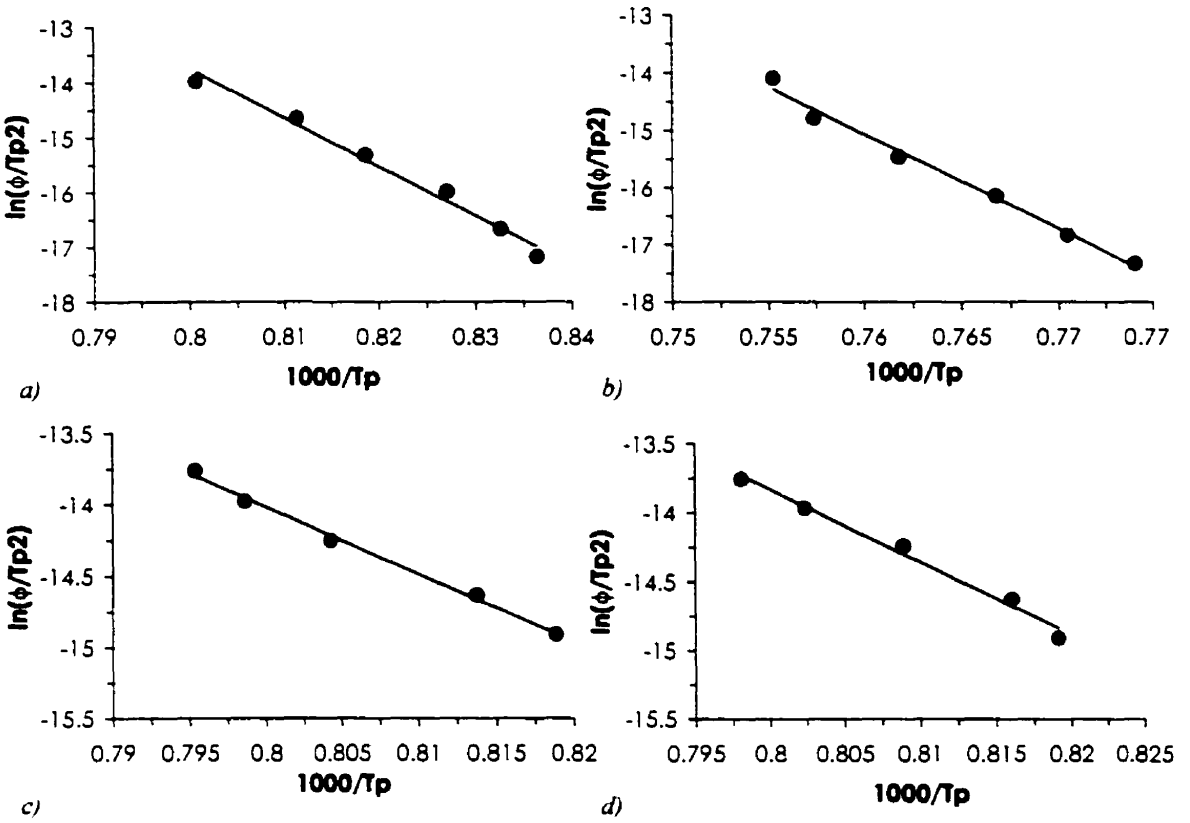

Figure 5.14 Kissinger plots for (a) E1 first crystallization event, (b) E1 second crystallization event, (c) Y_3A_5, and (d) E2.

The other method of analyzing DTA data proposed by Augis and Bennett is using the following relationship:

$$\ln\left[\frac{\phi}{(T_p - T_0)}\right] = -\frac{E_{cab}}{RT_p} + \ln k_0 \qquad (5.2)$$

where E_{cab} is the activation energy for crystallization estimated by the Augis-Bennett method (kJ/mol) and T_0 is the temperature from which the DTA scan starts (here, 1023 K).

The E_{cab} can be calculated from the slope of ln $[\phi/(T_p - T_0)]$ vs $1/T_p$ plot. The E_{cab} values for Al_2O_3-Y_3A_5 eutectic fibers were determined as 698 kJ/mol and 1346 kJ/mol for first and second crystallization events, respectively. The values of E_{cab} for Y_3A_5 and Y_3A_5-YA eutectic fibers are 352 kJ/mol and 399 kJ/mol, respectively (Figure 5.15).

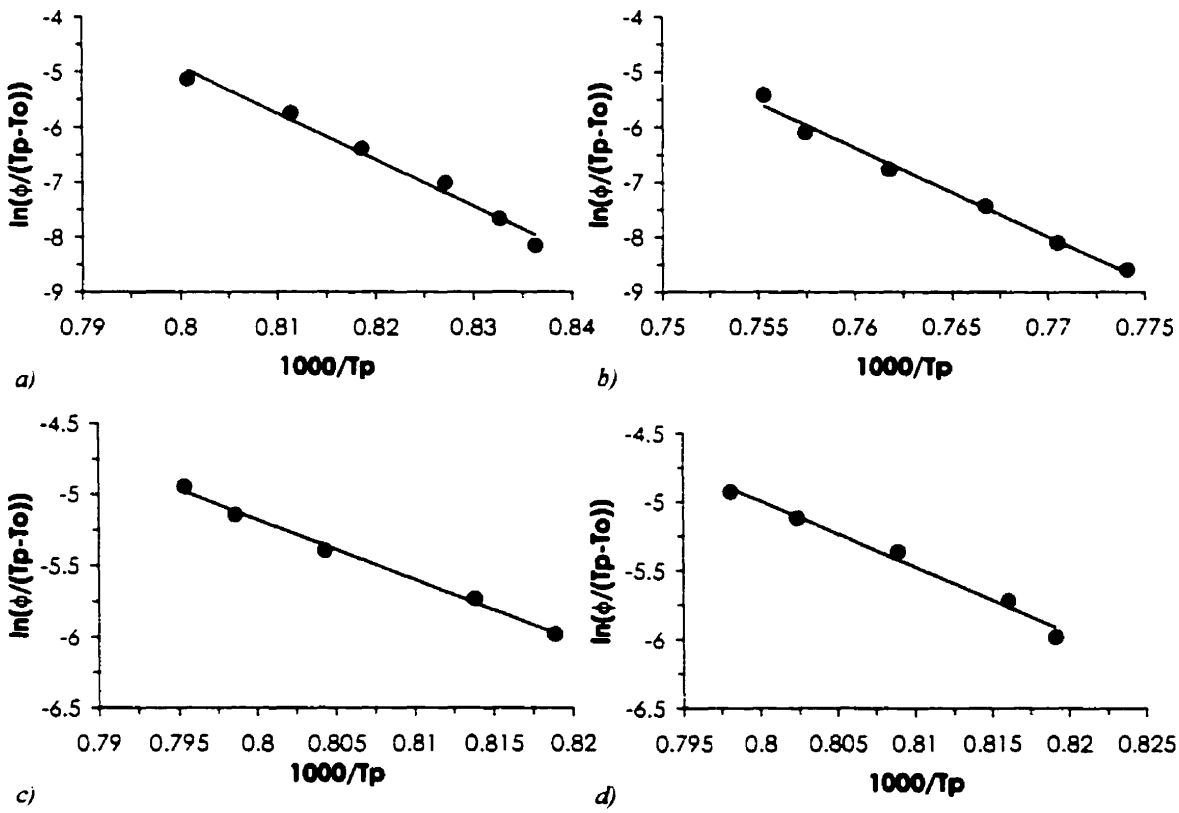

Figure 5.15 Augis-Bennett plots for (a) E1 first crystallization event, (b) E1 second crystallization event, (c) Y_3A_5, and (d) E2.

The crystallization mode can be identified by using the following Ozawa analysis (143, 144)

$$\ln[-\ln(1-x)] = -n\ln\phi + const. \tag{5.3}$$

where x is the volume fraction crystallized at a fixed temperature T when heated at ϕ, i.e., the ratio of the partial area at T to the total area of the crystallization exotherm. Here, the volume fraction crystallized was calculated at 960 °C and 1030 °C for first and second crystallization events in E1, respectively, and at 960 °C for Y_3A_5 and E2. The parameter n, is the Avrami parameter which indicates the mode of crystallization. When surface crystallization dominates, n = 1, and when bulk crystallization dominates, n = 3. When both surface and bulk crystallization occur n has a value between 1 and 3.

It is reasonable to consider that the crystallization process enthalpy is directly proportional to the area under the exothermic reaction peak of the DTA curve, and the volume fraction crystallized is directly proportional to the enthalpy. So the volume fraction crystallized at a certain temperature can be written in the following form:

$$x = \frac{A_T}{A} \tag{5.4}$$

where A_T is the area of the peak of the DTA curve at T, and A is the total area of the DTA curve peak. (Table 5.3).

In the Ozawa analysis, non-isothermal kinetics of the process of nucleation and its growth were derived by extending Avrami's equation to the non-isothermal situation. By

Table 5.3 Total area of the DTA peak, partial area of the DTA peak, and volume fraction crystallized at a fixed temperature T when heated at ϕ.

ϕ (°C/min)	A (°C x sec)	A_T	x (%)
E1, first DTA peak*, T = *960 °C			
3	129.90	129.00	99.31
5	155.17	147.49	95.05
10	145.20	131.96	90.19
20	103.13	90.15	87.41
40	118.18	38.74	32.78
80	99.93	1.04	1.04
E1, second DTA peak*, T = *1030 °C			
3	76.87	75.92	98.77
5	84.65	76.62	90.51
10	79.40	22.58	28.44
20	62.96	0.80	1.27
40	66.59	0.21	0.31
80	20.11	0.06	0.29
Y_3A_5*, T = *960 °C			
30	261.97	252.88	96.53
40	263.08	190.81	72.53
60	271.66	12.45	4.58
80	246.73	2.12	0.86
100	220.58	1.16	0.53
E2*, T = *960 °C			
30	279.88	269.13	96.16
40	266.83	225.68	84.58
60	244.95	33.19	13.55
80	257.03	7.73	3.01
100	233.22	3.39	1.46

substituting ϕ values and corresponding values of x into Equation 5.3, the Ozawa plots of the yttria-alumina fibers were created in Figures 5.16 and 5.17.

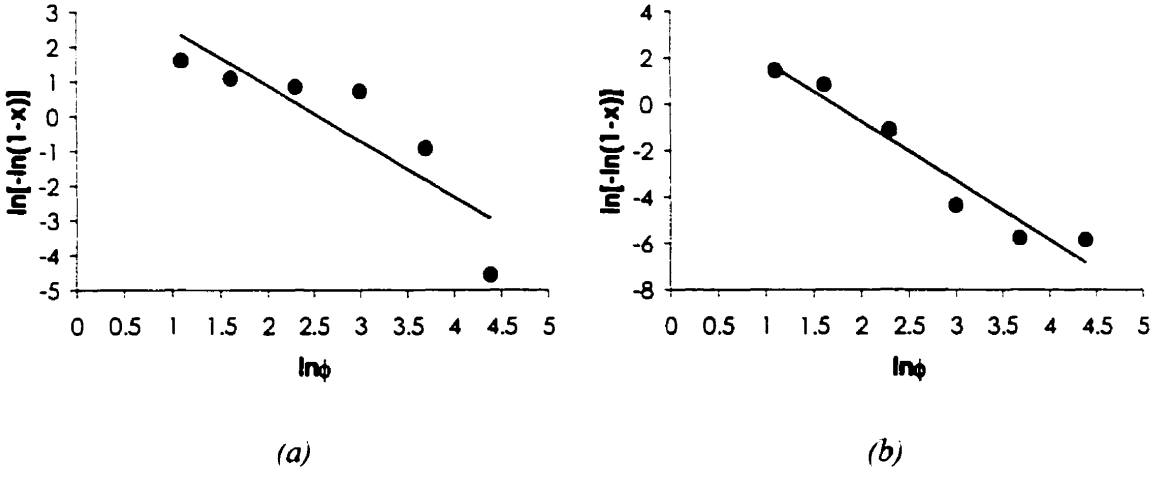

Figure 5.16 Ozawa plots of E1 fibers. The "x" indicates the volume fraction crystallized at 960 °C and 1030 °C for (a) first and (b) second crystallization events, respectively. From the slope of the curve the Avrami parameters (n) of the fibers were determined as 1.6 and 2.6. The correlation coefficients are 0.7572 and 0.9415, respectively.

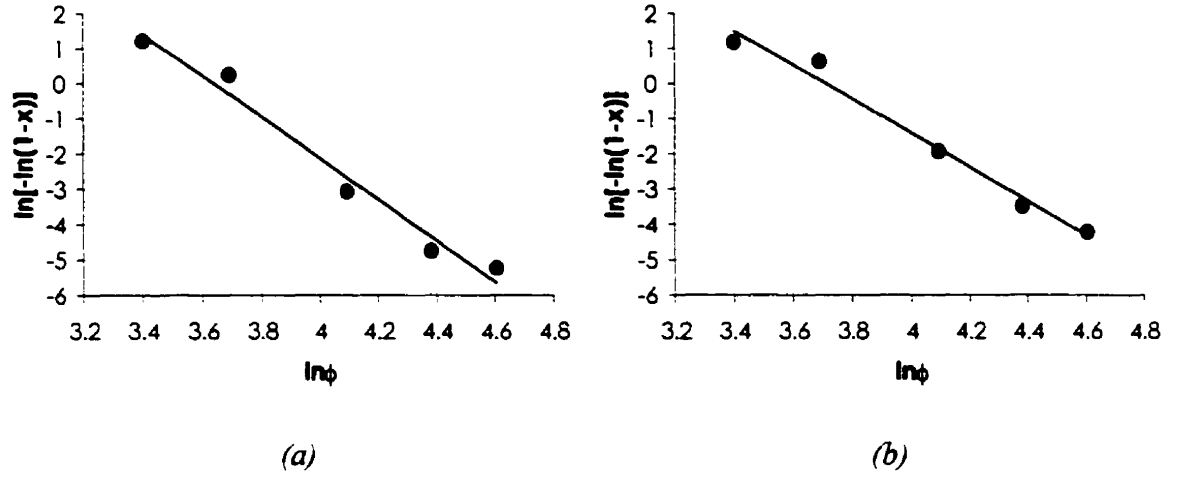

Figure 5.17 Ozawa plots of (a) Y_3A_5 and (b) E2 fibers. The "x" indicates the volume fraction crystallized at 960 °C. From the slope of the curve the Avrami parameters (n) of the fibers were determined as 5.9 and 4.8, respectively. The correlation coefficients are 0.9758 and 0.9809, respectively.

From the slope of the Ozawa plot the Avrami parameters of the yttria-alumina fibers were determined as 1.6 and 2.6 for E1 composition which implies both bulk and surface crystallization mode with diffusion controlled growth at zero nucleation rate (constant number of nuclei) and at constant nucleation rate, for first and second crystallization events, respectively [145-147]. Values of 5.9 and 4.8 were obtained for Y_3A_5 and E2 compositions, respectively, and are greater than 3, implying bulk crystallization with diffusion controlled growth with increasing nucleation rate [145-147]. Glasses generally crystallize by either surface or internal (volume) crystallization. Although both crystallization mechanisms can occur simultaneously and competitively, one mechanism usually dominates over the other in most cases. Table 5.4 recapitulates the kinetic parameters determined for yttria-alumina fibers. It can be noticed that values for activation energy and frequency factor determined by the two methods differ.

Table 5.4 Comparison of kinetic parameters determined by the two methods.

	Kissinger Method		***Augis-Bennett Method***		***n***
	E_{ck} **kJ/mol**	r^2	E_{cab} **kJ/mol**	r^2	
E1 First step	741 ± 47	0.9845	698 ± 46	0.9832	1.6 ± 0.5
E1 Second step	1374 ± 69	0.9902	1346 ± 69	0.9897	2.6 ± 0.3
Y_3A_5	390 ± 15	0.9955	352 ± 16	0.9944	5.9 ± 0.5
E2	438 ± 30	0.9867	399 ± 29	0.9844	4.8 ± 0.4

5.7 Interpretation of Kinetics Parameters

The activation energies for crystallization of yttria-alumina amorphous fibers were calculated by both the Kissinger and Augis Bennett methods. Most reactions in solid state phases are empirically described by the Avrami equation, where the amount of material, x, transformed at the time, t, is

$$x = 1 - \exp\left[-(kt)^n\right] \tag{5.5}$$

and where n is a dimensionless exponent called the reaction order or Avrami parameter, k is defined as the effective overall reaction rate constant. This is usually assigned an Arrhenius temperature dependence:

$$k = k_0 \exp\left(-\frac{E_c}{RT}\right) \tag{5.6}$$

where E_c is the effective activation energy describing the overall crystallization process, and k_0 is pre-exponential or frequency factor. The fundamental expression of Kissinger's method was derived by starting with the first order rate, $\frac{dx}{dt} = k(1-x)$, which corresponds to a special case of the Avrami equation where n = 1. Thus, equation 5.1 can only be used for solid-state reactions where n = 1, but unfortunately this is often not the case. In the present study the Avrami parameters were calculated by the Ozawa analysis, which is based in a non-isothermal kinetics of the process of nucleation and growth derived by extending Avrami's equation. The Avrami parameter values for the yttria-alumina fibers were 1.6 and 2.6 for first and second crystallization events in E1, respectively, and, 5.9 and 4.8 for Y_3A_5 and E2, respectively. All of these values are greater than 1, therefore the activation energies for crystallization calculated by Augis-Bennett method are more

reliable values. Augis-Bennett treatment utilizes the first and second derivatives of a general Avrami equation and is valid for any value of *n* and therefore is more applicable to solid-state reactions.

If mass transport of some species to the advancing interface controls the growth of the phases involved, we can perhaps get some idea of what those species are by comparing literature values for diffusion activation energies with those measured in the present study. The reaction (crystallization) can be controlled by diffusion of Al and O, Y and O, or Al-Y exchange. Some evidence suggests that yttrium is the slowest diffusing species in the alumina-yttria system [148, 149]. Therefore the slowest diffusing species of the Al, O pair would control the reaction rate. Tables 5.5-5.7 give literature values of activation energy of Al, O and Y diffusion in YAG and alumina.

Table 5.5 Activation energies of Al, O and Y diffusion in YAG and alumina.

	Activation Energy, kJ/mol	**Temperature range, °C**
O lattice diffusion in YAG single crystal [150]	325	1060-1550
Al lattice diffusion in alumina [151]	500 – 570	1500-1900
Y lattice difussion in α-alumina single crystal [152]	295	1150-1500

Table 5.6 Activation energies (kJ/mol) of oxygen diffusion in polycrystalline yttrium aluminum garnet (YAG) ceramics for a temperature range of 1100-1385 °C [153].

	Lattice diffusion	**Grain boundary diffusion**
2 % Y_2O_3	259.6	NA
1 % Y_2O_3	223.9	NA
Stoichiometry	304.1	393.8
0.5 % Al_2O_3	519.4	688.8

Table 5.7 Activation energies of aluminum and oxygen diffusion in α-alumina.

	Lattice diffusion	**Subboundary diffusion**	**Grain boundary diffusion**	**Temperature range, °C**
Al diffusion in undoped α-alumina single crystal [154]	510	850	NA	1540-1697
O diffusion in undoped α-alumina single crystal [155]	636	896	NA	1500-1720
O diffusion in Y-doped α-alumina single crystal [156]	590	980	NA	1110-1630
O diffusion in undoped α-alumina polycrystal [157]	NA	NA	921	1460-1720
O diffusion in Y-doped α-alumina polycrystal [157]	440	NA	800	1460-1720

NA: Not available.

The 352 kJ/mol value for the activation energy of Y_3A_5 crystallization is near 325 kJ/mol value reported for oxygen lattice diffusion in YAG single crystal and the 393.8 kJ/mol value reported for oxygen grain boundary diffusion in stoichiometric polycrystalline YAG. The activation energy for oxygen lattice diffusion in YAG single crystal is considered to be due to the migration of oxygen vacancies [150].

The activation energy for the first crystallization event in E1 of 698 kJ/mol is comparable to the activation energy of 688.8 kJ/mol reported for oxygen grain boundary diffusion in Al_2O_3-excess polycrystalline YAG. In the diffusion experiments carried out by Sakaguchi *et al.* [153], Y_2O_3-excess and Al_2O_3-excess specimens had different second phases: the silicon-rich second phase (YAP) in Y_2O_3-excess specimens and the Si segregant and Al_2O_3 precipitates at grain boundaries in Al_2O_3-excess specimens (200 ppm of Si, was doped in all powders to facilitate sintering). Aluminum-rich particles (alumina) and silicon segregation to the grain boundary were observed in Al_2O_3-excess specimens, and the grain growth of second phase did not result in silicon transfer toward the second phase. However, the activation energy of grain boundary diffusion in Al_2O_3-excess specimens was larger than that of the stoichiometric specimen by a factor of two, as in the case of the activation energy of Y_3A_5 and first crystallization event in E1. This difference was considered to be due to the second phase in the grain boundary.

The activation energy for crystallization of the second event in E1 fibers is relatively high, 1346 kJ/mol. Besides thermally activated nucleation, the activation

energy includes contributions from interface reactions (i.e., dissolution of yttria and alumina species) and diffusional processes. This can explain the high value in the calculated activation energy for crystallization in the second event for E1 fibers. Among the diffusion activation energies of Al, Y, and O species reported to date in the literature, the closest are 980 and 921 kJ/mol which are the activation energy for oxygen subboundary diffusion in a Y-doped, α-alumina single crystal and oxygen grain boundary diffusion in an undoped α-alumina polycrystal, respectively. Subboundary and grain boundary diffusion are characterized by an activation energy greater than the activation energy for lattice diffusion on account of segregation phenomena. They correspond to the sum of a term of migration enthalpy and a term of interaction between the diffusing species and the segregated impurities [154-157].

From the above, it seems that oxygen mass transfer, either by lattice, subboundary or grain boundary diffusion is the predominant mechanism that controls the crystallization process.

Differential thermal analysis has been used to study the kinetics of rate-controlled processes such as the kinetics of crystallization in glass-forming systems. By applying the Kissinger method to the DTA scan data, the activation energy values for crystallization were determined to be 569 and 546 kJ/mol, respectively for the as-spun and fully nucleated calcium aluminate glass fibers [144]. Both methods have been applied in the crystallization of inviscid melt spun calcia-alumina eutectic fibers [158]. The activation

energies for crystallization were determined as 490 and 477 kJ/mol by Kissinger and Augis-Bennett methods, respectively. The activation energy for crystallization of YAG sol-gel-derived powder was estimated at about 289 kJ/mol by the isothermal process fitted with Johnson-Mehl-Avrami equation, and about 930 kJ/mol by the continuous heating method fitted to the Kissinger method. The difference in activation energies calculated by the two methods was pointed out to be mainly due to the complicated crystallization behavior of YAG [159]. The activation energy for crystallization for aluminum silicate glass fibers was 888 kJ/mol by the Kissinger method [160]. The crystallization kinetics of mullite in Al_2O_3-SiO_2 glass fibers has been investigated isothermally [161]. The activation energies for nucleation were 860-980 kJ/mol, and for nucleation-growth 1099-1195 kJ/mol. These values are of the order reported for activation energies during the crystallization of the yttria-alumina fibers.

CHAPTER 6

CONCLUSIONS

This chapter contains conclusions that have been drawn from the above production and characterization of yttria-alumina fibers, and their subsequent devitrification.

1. It has been demonstrated that various yttria-alumina compositions can be extracted from the molten state by melt extraction technique. In addition, the examined method of production of fibers from oxides makes it possible to produce, efficiently, fibers of not only pure oxides but also synthesis complex compounds.

2. The fiber morphology and diameter were markedly influenced by the wheel velocity and the wheel tip geometry. Uniform fibers with almost circular cross-sections could be obtained at wheel velocities < 3 m/s. These fibers are fine with a diameter range size of 20-30 μm. However, at higher velocities, irregularities and instabilities, such as Rayleigh waves, could be observed. On the other hand, a sharp wheel tip produced thinner and

more flexible fibers with a smaller wheel tip track on the surface than a blunt wheel tip. This wheel tip track gave to the fiber a characteristic kidney shape when they are observed in cross-section.

3. Regardless of the chemical composition and wheel velocity, all extracted fibers were X-ray amorphous and transparent due to the rapid cooling of the extraction system. This revealed the good glass-forming characteristics of the molten yttria-alumina material under rapid solidification conditions. Furthermore, fibers in the as-produced state had uniform compositional distribution along their length and between the edge and the core of the fibers and they approximated the theoretical stoichiometry.

4. The fiber melt extraction process created uniform property fibers with smooth surfaces, which were defined by surface tension of the liquid acting in the region where the fiber was extracted from the molten liquid. The fibers contained minimal flaws and exhibited brittle fracture with moderate values of tensile strength (606-776 MPa), Young's modulus (95-121 GPa), and Weibull modulus (2.3-2.8).

5. Heating the amorphous fibers initiated crystallization in the range of 939-949 °C. Granular and nanocrystalline (grain size 100-500 nm, in the case of E1) structures developed on the surface of the heat-treated fibers due to the nucleation and grain growth of various phases accompanied by a conversion of the transparent glass fiber to an opaque polycrystalline material. Tensile strength tests of heat-treated fibers confirmed that the mechanical properties deteriorated after crystallization. This makes the fibers

suitable for reinforcing matrices to produce composites materials that can be processed and utilized at temperatures that do not exceed 939 °C.

6. Several metastable crystal phases were observed during crystallization of amorphous fibers. δ-Al_2O_3 was observed to crystallize prior to the equilibrium α-Al_2O_3 structure in E1 fibers. Cubic YAP phase preceded the formation of the stable orthorhombic YAP and YAG phases in E2 fibers. YAG phase crystallized directly from the Y_3A_5 fiber with no intermediate phases at 850 °C, revealing the stability of this phase at temperatures as high as 1500 °C. This method, combined with annealing, can be used to produce oxide fibers with the required chemical phase composition.

7. Nonisothermal DTA data were used to determine the nucleation rate-type curve for the yttria-alumina glass fibers. From these curves, the temperature range for nucleation and that for maximum nucleation rate were obtained as 600-700 °C and 650 °C for both crystallization events in E1 fibers, respectively, and 700-850 °C and 800 °C for Y_3A_5 and E2 fibers, respectively.

8. Crystallization of amorphous fibers was estimated as being oxygen diffusion controlled in lattice, subboundary, or grain boundary, according with the calculated activation energies. The mode of crystallization was found to be both bulk and surface crystallization for E1 fibers with diffusion controlled growth at zero rate nucleation (constant number of nuclei) and at constant nucleation rate for first and second events of crystallization, respectively, and solely bulk crystallization for Y_3A_5 and E2 fibers with

diffusion controlled growth at increasing nucleation rate, according with the calculated Avrami parameters.

RECOMMENDATIONS FOR FUTURE WORK

Certainly, all experimental work performed are restricted by the available time, funding and technology. As a result of what has been learned in this research, I can make the following recommendations for future work.

- The process of forming glass fibers from melts using the melt extraction technique, greatly expands the range of materials, which can be made into fibers, it is inherently fast and it can provide a source of materials for high temperature structural applications. The glass fibers can be produced with a uniform distribution of additives and dopants. Any continuing work should emphasize the study of additives and dopants effects, and control of the thermal processing on the macrostructure and properties of the crystalline fibers. Addition of excess alumina or substitution of neodymium oxide for yttrium oxide in the YAG-composition has been shown to enhance glass formation and improve the quality of fibers pulled from undercooled melts [119]. Moreover, the use of dopants that reduce diffusion rates to minimize grain growth kinetics during crystallization should be investigated as a way of improving the mechanical properties of the fibers.

- Molten alumina-yttria materials have shown a greater glass-forming tendency in an argon atmosphere than in oxygen [119]. Hence, the production of fibers by melt extraction

in different atmosphere other than air would yield better quality fibers with more outstanding physical and mechanical properties.

- The fiber making process also allows control of fiber diameter through changes in the fiber extracting conditions. These fibers are thus considered to be suitable precursors for investigating the production of ceramic oxide fibers by controlled crystallization of the glass in order to retain their tensile strength or improve it by promoting grain growth along the fiber axis. This includes the evaluation of mechanical properties at high temperatures.

- Study of interfacial wetting and interface formation with some potential matrices, such as metals or glass-ceramics, to be reinforced in order to produce composite materials, identifying the crystalline phases in the interface of these composites.

- Application of doped amorphous fibers for photonic applications.

- Implementation of process developments such as the used of a laser heat-source in the melt extraction system.

STATEMENT OF ORIGINALITY AND CONTRIBUTIONS TO KNOWLEDGE

- This thesis has been the first work to investigate the feasibility of making fine (20-30 μm) ceramic fibers in the system Y_2O_3-Al_2O_3 from the molten state by melt extraction.

- A complete characterization of the melt extracted fibers including morphology and surface characteristics related to the process variables, compositional distribution, measurement of tensile strength and a study of statistical distribution of strengths. This allowed to determine potential applications of the fibers.

- The first investigation of devitrification behavior of Y_2O_3-Al_2O_3 fibers, including determination of glass transition, crystallization, and phase transformation points, in addition to a study of phase development and microstructural evolution.

- Characterization of the oxide fibers with glassy and metastable phases (δ-alumina and cubic YAP) were identified as intermediate phases in the devitrification of yttria-alumina fibers as well as nanocrystalline microstructures produced from the starting oxide compounds.

- Differential thermal analysis (DTA) went far beyond the conventional measurements of some characteristics points such as glass transition, crystallization, and phase decomposition and transformation points, and was used to provide important information for fundamental phenomena such as nucleation and crystallization of yttria-alumina glass fibers. This dynamic method is faster and requires smaller samples.

- First nucleation study with this type of glass including the calculation of the temperature range for nucleation along with the temperature for maximum nucleation rate. These are important factors to understanding the stability of a glass for practical applications and controlling parameters (temperature, time) for preparing glass-ceramics.

- The quantitative analysis of crystallization is considered to be a major contribution because it was attempted for the first time with glass fibers in the system yttria-alumina. This analysis includes the calculation of kinetic parameters, namely activation energy and order of the reaction (also known as Avrami parameter) that is related to the dimensionality of crystal growth.

REFERENCES

1. K. K. Chawla, Composites Materials: Science and Engineering, Second Edition, Springer-Verlag, New York, 1998.

2. R. W. Cahn, P. Haasen and E. J. Kramer, Materials Science and Technology, Volume 13: Structure and Properties of Composites, Edited by Tsu-Wei Chou, VCH, 1991.

3. J. A. DiCarlo, "Fibers for Structurally Reliable Metal and Ceramics Composites", *Journal of Metals*, pp. 44-49 (1995).

4. S. V. Nair and K. Jakus, Editors, High Temperature Mechanical Behavior of Ceramic Composites, Butterworth-Heinemann, Boston 1995.

5. A. Ikesue, T. Kinoshita, K. Kamata and K. Yoshida, "Fabrication and Optical Properties of High-Performance Polycrystalline Nd:YAG Ceramics for Solid-State Lasers", *Journal of the American Ceramic Society*, 78 [4], pp. 1033-1040 (1995).

6. K. Keller, T. Mah and T. A. Parthasarathy, "Processing and Mechanical Properties of Polycrystalline $Y_3Al_5O_{12}$ (Yttrium Aluminum Garnet)", *Ceramic Engineering and Science Proceedings*, 11 [7-8], pp. 1122-1133 (1990).

7. T. Mah, T. A. Parthasarathy and L. E. Matson, "Processing and Mechanical Properties of $Al_2O_3/Y_3Al_5O_{12}$ (YAG) Eutectic Composite", *Ceramic Engineering and Science Proceedings*, 11 [9-10], pp. 1617-1627 (1990).

8. T. A. Parthasarathy, T. Mah and L. E. Matson, "Creep Behavior of $Al_2O_3/Y_3Al_5O_{12}$ Eutectic Composite", *Ceramic Engineering and Science Proceedings*, 11 [9-10], pp. 1628-1638 (1990).

9. T. A. Parthasarathy, T. Mah and K. Keller, "High-Temperature Deformation Behavior of Polycrystalline Yttrium Aluminum Garnet (YAG)", *Ceramic Engineering and Science Proceedings*, 12 [9-10], pp. 1767-1773 (1991).

10. T. A. Parthasarathy, T. Mah and K. Keller, "Creep Mechanism of Polycrystalline Yttrium Aluminum Garnet", *Journal of the American Ceramic Society*, 75 [7], pp. 1756-1759 (1992).

11. T. A. Parthasarathy, T. Mah and L. E. Matson, "Deformation Behavior of an Al_2O_3-$Y_3Al_5O_{12}$ Eutectic Composite in Comparison with Sapphire and YAG", *Journal of the American Ceramic Society*, 76 [1], pp. 29-32 (1993).

12. T. Mah, T. A. Parthasarathy, M. D. Petry and L. E. Matson, "Processing, Microstructure, and Properties of Al_2O_3-$Y_3Al_5O_{12}$ (YAG) Eutectic Fibers", *Ceramic Engineering and Science Proceedings*, 14 [7-8], pp. 622-638 (1993).

13. S. C. Farmer, A. Sayir, P. O. Dickerson and S. L. Draper, "Microstructural Stability and Strength Retention in Directionally Solidified Al_2O_3-YAG Eutectic Fibers", *Ceramic Engineering and Science Proceedings*, 16 [5], pp. 969-976 (1995).

14. P. A. Doleman and E. G. Butler, "The Growth of Alumina/YAG Eutectic Fibers by the Laser Heated Floating Zone Process", *Key Engineering Materials*, 127-131, pp. 193-202 (1997).

15. G. N. Morscher, K. C. Chen and K. S. Mazdiyasni, "Creep-Resistance of Developmental Polycrystalline Yttrium-Aluminum Garnet Fibers", *Ceramic Engineering and Science Proceedings*, 15 [4], pp. 181-188 (1994).

16. B. H. King, Y. Liu, R. M. Laine and J. W. Halloran, "Fabrication of Yttrium Aluminate Fibers", *Ceramic Engineering and Science Proceedings*, 14 [7-8], pp. 639-650 (1993).

17. B. H. King and J. W. Halloran, "Polycrystalline Yttrium Aluminum Garnet Fibers from Colloidal Sols", *Journal of the American Ceramic Society*, 78 [8], pp. 2141-2148 (1995).

18. W. Glaubitt, W. Watzka, H. Scholz and D. Sporn, "Sol-Gel Processing of Functional and Structural Ceramic Oxide Fibers", *Journal of Sol-Gel Science and Technology*, 8 [1-3], pp. 29-33 (1997).

19. R. C. Pullar, M. D. Taylor and A. K. Bhattacharya, "The Manufacture of Yttrium Aluminum Garnet (YAG) Fibres by Blow Spinning from a Sol-Gel Precursor", *Journal of the European Ceramic Society*, 18 [12], pp. 1759-1764 (1998).

20. D. Popovich, J. Lombardi and B. H. King, "Fabrication and Mechanical Properties of Polymer Melt Spun Yttrium Aluminum Garnet (YAG) Fiber", *Ceramic Engineering and Science Proceedings*, 18 [3], pp. 65-72 (1997).

21. D. Zhu, M. H. Jilavi and W. M. Kriven, "Synthesis and Characterization of Mullite and YAG Fibers Grown from Deeply Undercooled Melts", *Ceramic Engineering and Science Proceedings*, 18 [3], pp. 31-38 (1997).

22. M. Allahverdi, Ph. Thesis, "Melt Extraction of Oxide Ceramic Fibers", Dept. of Mining and Metallurgical Engineering, McGill, Montreal, Quebec, Canada, 1991.

23. T. F. Cooke, "Inorganic Fibers – A Literature Review", *Journal of the American Ceramic Society*, 74 [12], pp. 2959-2978 (1991).

24. K. K. Chawla, Fibrous Materials, Cambridge University Press, 1998.

25. T. J. Reinhart, Engineered Materials Handbook, Volume 1: Composites, ASM International, Metals Park, Ohio 44073, 1987.

26. A. G. Evans and D. B. Marshall, "The Mechanical Behavior of Ceramic Matrix Composites", *Acta Metallurgica*, 37 [10], pp. 2567-2583 (1989).

27. R..J. Kerans, R. S. Hay, N. J. Pagano and T. A. Parthasarathy, "The Role of the Fiber-Matrix Interface in Ceramic Composites", *American Ceramic Society Bulletin*, 68 [2], pp. 429-442 (1989).

28. V. Ya. Varxhavskii, "Chemistry and Technology of Chemical Fibers. Ceramic Fibers. A Review", *Fibre Chemistry*, 25 [1], pp. 1-6 (1993).

29. F. T. Wallenberger, Editor, Advanced Inorganic Fibers: Processes, Structures, Properties, Applications, Kluwer Academic Publishers, 2000.

30. A. R. Bunsell and M. H. Berger, "Ceramic Fibre Development and Characterization", *Key Engineering Materials*, 127-131 [2], pp. 15-26 (1997).

31. A. R. Bunsell and M. H. Berger, "Inorganic Fibers for Composite Materials", *Composite Science and Technology*, 51, pp. 127-133 (1994).

32. A. R. Bunsell, "High Temperature Fibres", *Materiaux et Techniques*, 82 [4-5], pp. 3-6 (1994).

33. K. R. Venkatachari, L. T. Moeti, M. D. Sacks and J. H. Simmons, "Preparation of Mullite-Based Fibers by Sol-Gel Processing", *Ceramic Engineering Science Proceedings*, 11 [9-10], pp. 1512-1525 (1990).

34. A. Towata, H. J. Hwang, M. Yasuoka, M. Sando and K. Niihara, "Fabrication of Fine YAG-Particulate-Dispersed Alumina Fiber", *Journal of the American Ceramic Society*, 81 [9], pp. 2469-2472 (1998).

35. Q.-G. Chen and T. J. Davies, "Sol-Gel Processing of Refractory Compounds in Alumina-Baria System", *British Ceramic Transactions*, 96 [4], pp. 170-174 (1997).

36. R. L. AshBrook, "Directionally Solidified Ceramic Eutectics", *Journal of the American Ceramic Society*, 60 [9-10], pp. 428-435 (1977).

37. H. E. Bates, "EFG Growth of Alumina-Zirconia Eutectic Fiber", *Ceramic Engineering Science Proceedings*, 13 [7-8], pp. 190-197 (1992).

38. J. S. Haggerty and K. C. Wills, "Growth and Properties of Single Crystal Oxide Fibers", *Ceramic Engineering Science Proceedings*, 12 [9-10], pp. 1785-1801 (1991).

39. J. Sigalovsky, J. S. Haggerty and J. E. Sheehan, "Growth of Spinel Single Crystal Fibers by the Laser-Heated Floating-Zone Technique and Their Characterization as High Temperature Reinforcements", *Journal of Crystal Growth*, 134, pp. 313-324 (1993).

40. J. E. Sheehan, J. Sigalovsky, J. S. Haggerty and J. R. Porter, "Mechanical Properties of $MgAl_2O_4$ Single Crystal Fibers", *Ceramic Engineering Science Proceedings*, 14 [7-8], pp. 660-670 (1993).

41. K. J. McClellan, H. Sayir, A. H. Heuer, A. Sayir, J. S. Haggerty and J. Sigalovsky, "High Strength, Creep-Resistant Y_2O_3-stabilized Cubic ZrO_2 Single Crystal Fibers", *Ceramic Engineering Science Proceedings*, 14 [7-8], pp. 651-659 (1993).

42. E. L. Courtright, J. S. Haggerty and J. Sigalovsky, "Controlling Microstructure in $ZrO_2(Y_2O_3)$-Al_2O_3 Eutectic Fibers", *Ceramic Engineering Science Proceedings*, 14 [7-8], 671-81 (1993).

43. H. Sayir, A. Sayir and K. P. D. Lagerlöf, "Temperature Dependent Brittle Fracture of Undoped and Impurity Doped Sapphire Fibers", *Ceramic Engineering Science Proceedings*, 14 [7-8], pp. 581-589 (1993).

44. J.-M. Yang, S. M. Jeng and S. Chang, "Fracture Behavior of Directionally Solidified $Y_3Al_5O_{12}/Al_2O_3$ Eutectic Fiber", *Journal of the American Ceramic Society*, 79 [5], pp. 1218-1222 (1996).

45. F. T. Wallenberger, N. E. Weston, K. Motzfeldt and D. G. Swartzfager, "Inviscid Melt Spinning of Alumina Fibers: Chemical Jet Stabilization", *Journal of the American Ceramic Society*, 75 [3], pp. 629-636 (1992).

46. F. T. Wallenberger, N. E. Weston and K. Motzfeldt, "Inviscid Melt Spinning of Alumina Fibers: Jet Stabilization Mechanism", *Ceramic Engineering Science Proceedings*, 12 [7-8], pp. 1039-1047 (1991).

47. Y.-M. Sung and J.-H. Sung, "Inviscid Melt Spun (IMS) Alumina Short Fibres Showing Frozen Rayleigh Waves", *Journal of Materials Science Letters*, 17 [9], pp. 705-708 (1998).

48. Y.-M. Sung and S. A. Dunn, "Phase Transformation of Calcia-Alumina-Magnesia Fibres Produced by Inviscid Melt Spinning", *Journal of Materials Science*, 31 [18], pp. 4741-4744 (1996).

49. Y.-M. Sung and S. A. Dunn, "Inviscid Melt-Spun High-Temperature Alumina-Magnesia Fibres", *Journal of Materials Science*, 31 [18], pp. 3657-3660 (1996).

50. Y.-M. Sung, S. A. Dunn and J. A. Koutsky, "Phase Transformation of Inviscid Melt Spun (IMS) Alumina-Zirconia Eutectic Fibres", *Journal of Materials Science*, 30 [23], pp. 3995-3998 (1995).

51. S. J. Savage and F. H. Froes, "Production of Rapidly Solidified Metals and Alloys", *Journal of Metals*, 36 [4], pp. 20-33 (1984).

52. R. E. Maringer and C. E. Mobley, "Casting of Metallic Filament and Fiber", *Journal of Vacuum Science and Technology*, 11 [6], pp. 1067-1071 (1974).

53. R. E. Maringer and C. E. Mobley, "Advances in Melt Extraction", in Rapidly Quenched Metals III, edited by B. Cantor, The Metals Society, London, UK, 1, pp. 49-56 (1978).

54. B. Cockayne, "The Uses and Enigmas of the Al_2O_3-Y_2O_3 Phase System", *Journal of the Less-Common Metals*, 114 [1], pp. 199-206 (1985).

55. D. I. Martkin, in B. Cockayne and D. W. Jones, Editors, Modern Oxide Materials, Academic Press, London, 1972.

56. A. K. Levine and F. C. Pallila, International Symposium on Luminescence, Thiemig, München, pp. 317 (1965).

57. T. H. Maiman, "Simulated Optical Radiation in Ruby", *Nature*, 187, pp. 493-494 (1960).

58. T. H. Maiman, "Optical and Microwave-Optical Experiments in Ruby", *Physical Review Letters*, 4 [11], pp. 564-566 (1960).

59. P. F. Moulton, *Laser Focus*, pp. 83 (1983).

60. J. E. Geusic, H. M. Marcos and L. G. Van Uitert, "Laser Oscillation in Nd-doped Yttrium Aluminum, Yttrium Gallium and Gadorinum Garnets", *Applied Physics Letters*, 4 [10], pp. 182-184 (1964).

61. M. J. Weber, M. Bass, K. Adringa, R. R. Monchamp and E. Comperchio, *Applied Physics Letters*, 15, pp.342 (1969).

62. D. J. Robbins, *Microelectronics*, 11, pp. 10 (1980).

63. G. W. Cullen, "The Preparation and Properties of Chemically Vapor Deposited Silicon on Sapphire and Spinel", *Journal of Crystal Growth*, 9, pp. 107 (1971).

64. L. E. Matson, R. S. Hay and T. Mah, "Characterization of Alumina/Yttrium-Aluminum Garnet and Alumina/Yttrium Aluminum Perovskite Eutectics", *Ceramic Engineering Science Proceedings*, 11 [7-8], pp. 995-1003 (1990).

65. A. Verneuil, *Annales de Chimie*, 8, pp. 320 (1904).

66. B. Cockayne, M. Chesswas and D. B. Gasson, "Single-Crystal Growth of Sapphire", *Journal of Materials Science*, 2, pp. 7 (1967).

67. D. B. Gasson and B. Cockayne, "Oxide Crystal Growth using Gas Lasers", *Journal of Materials Science*, 5, pp. 100 (1970).

68. S. J. Schneider, R. S. Roth and J. S. Waring, *Journal of Research of the National Bureau of Standards. Section A. Physics and Chemistry*, 65, pp. 345 (1961).

69. L. E. Olds and H. E. Otto, in E. M. Levin *et al.*, Editors, Phase Diagrams for Ceramists, American Ceramic Society, Columbus, OH, Fig. 311, 1964.

70. I. Warshaw and R. Roy, "Stable and Metastable Equilibria in the Systems Y_2O_3-Al_2O_3 and Gd_2O_3-Fe_2O_3", *Journal of the American Ceramic Society*, 42 [9], pp. 434-438 (1959).

71. N. A. Toropov, I. A. Bondar, F. Ya. Galakhov, X. S. Nikogosyan and N. V. Vinogradova, *Izvestiya Akademii Nauk SSSR*, Ser. Khim., 7, pp. 1162 (1964).

72. M. Mizuno and T. Noguchi, *Rep. Gov. Ind. Res. Inst. Nagoya*, 16, pp. 171 (1967).

73. W. Class, "Growth of Yttrium Aluminate and Yttrium Aluminum Garnet by a Hollow Cathode Floating-Zone Method", *Journal of Crystal Growth*, 3 [4], pp 241 (1968).

74. J. S. Abell, I. R. Harris, B. Cockayne and B. Lent, "An Investigation of Phase Stability in the Y_2O_3-Al_2O_3", *Journal of Materials Science*, 9, pp. 527-537 (1974).

75. H. S. Yoder and M. S. Keith, *American Mineralogist*, 36, pp. 519 (1951).

76. B. Cockayne and B. Lent, "Complexity in the Solidification Behavior on molten $Y_3Al_5O_{12}$" *Journal of Crystal Growth*, 46 [3], pp. 371-378 (1979).

77. J. L. Caslavsky and D. J. Viechnicki, "Melting Behavior and Metastability of Yttrium Aluminum Garnet (YAG) and $YAlO_3$ Determined by Optical Differential Thermal Analysis", *Journal of Materials Science*, 15 [7], pp. 1709-1718 (1980).

78. S. Aasland and P. F. McMillan, "Density-Driven Liquid-Liquid Phase Separation in the System Al_2O_3-Y_2O_3", *Nature*, 369, pp. 633-636 (1994).

79. G. T. Adylov, G. V. Voronov, E. P. Mansurova, L. M. Sigalov and E. M. Urazaeva, "The Y_2O_3-Al_2O_3 System Above 1473 K", *Russian Journal of Inorganic Chemistry*, 33 [7], pp. 1062-1063 (1988).

80. Z. Jin and Q. Chen, "An Assessment of the $AlO_{1.5}$- $YO_{1.5}$ System", *Calphad*, 19 [1], pp. 69-79 (1995).

81. J. Gröbner, H. L. Lukas and F. Aldinger, "Thermodynamic Calculation of the Quasibinary Al_2O_3-Y_2O_3 System on the Y-Al-O Ternary System", *Zeitschrift fur Metallkunde*, 87, pp. 268-273 (1996).

82. A. A. Maier and I. G. Savinova, "Melting Behavior and Crystal Growth of $YAlO_3$", *Inorganic Materials*, 32 [10], pp. 1078-1080 (1996).

83. H. Yamane, M. Omori and T. Hirai, "Thermogravimetry and Rietveld Analysis for the High-Temperature X-ray Powder Diffraction Pattern of $Y_4Al_2O_9$", *Journal of Materials Science Letters*, 14, pp. 470-473 (1995).

84. H. Yamane, K. Ogawara, M. Omori and T Hirai, "Phase Transition of Rare-Earth Aluminates ($RE_4Al_2O_9$) and Rare-Earth Gallates ($RE_4Al_2O_9$)", *Journal of the American Ceramic Society*, 78 [9], pp. 2385-2390 (1995).

85. U. Kolitsch, H. J. Seifert, T. Ludwig and F. Aldinger, "Phase Equilibria and Crystal Chemistry in the Y_2O_3-Al_2O_3-SiO_2 System", *Journal of Materials Research*, 14 [2], pp. 447-455 (1999).

86. M. C. Brockway and R. R. Wills, "Rapid Solidification of Ceramics – A Technology Assessment", MCIC Report 84-49, Metals and Ceramic Information Center, Columbus, Ohio, 1984.

87. F. E. Luborsky, Ed., Amorphous Metallic Alloys, Butterworths, 1983.

88. P. W. McMillan, Glass-Ceramics, Second Edition, Academic Press, 1979.

89. R. S. Roth, Phase Diagrams for Ceramists, Volume XI, Compiled at the National Institute of Standards and Tenchnology, Edited and Published by The American Ceramic Society, Fig. 9265, 1995.

90. J. O. Strom-Olsen and P. Z. Rudkowski, "Apparatus and Method for Fabrication of Metallic Fibers Having a Small Cross Section", U.S. Patent No. 5027886, 1991.

91. P. Rudkowski, G. Rudkowska and J. O. Strom-Olsen, "The Fabrication of Fine Metallic Fibers by Continuous Melt-Extraction and Their Magnetic Properties", *Materials Science and Engineering*, A133, pp. 158-161 (1991).

92. M. Allahverdi, R. A. L. Drew and J. O. Strom-Olsen, "Melt Extracted Oxide Ceramic Fibers-The Fundamentals", *Journal of Materials Science*, 31 [4], pp. 1035-1042 (1996).

93. J. O. Strom-Olsen, G. Rudkowska, P. Rudkowski, M. Allahverdi and R. A. L. Drew, "Fine Metallic and Ceramic Fibers by Melt Extraction", *Materials Science and Engineering*, A179/A180, pp. 158-162 (1994).

94. J. O. Strom-Olsen, "Fine Fibres by Melt Extraction", *Materials Science and Engineering*, A178, pp. 239-243 (1994).

95. ASTM Standard D3379-75, "Standard Test Method for Tensile Strength and Young's Modulus for High-Modulus Single-Filament", American Society for Testing and Materials, Philadelphia, PA, 1989.

96. M. Allahverdi, R. A. L. Drew, P. Rudkowska, G. Rudkowski and J. O. Strom-Olsen, "Amorphous $CaO \cdot Al_2O_3$ Fibers by Melt Extraction", *Materials Science and Engineering*, A207, pp. 12-21 (1996).

97. V. J. Fratello, and C. D. Brandle, " Physical Properties of a $Y_3Al_5O_{12}$ Melt", *Journal of Crystal Growth*, 128, pp. 1006-1010 (1993).

98. O. V. Mazurin, M. V. Streltsina and T. P. Shvaiko-Shvaikovskaya, Physical Sciences Data 15, Handbook of Glass Data Part B, "Single Component and Binary Non-Silicate Oxide Glasses", Elsevier, 1985.

99. ASTM Standard C1322-96a, "Standard Practice for Fractography and Characterization of Fracture Origins in Advanced Ceramics", American Society for Testing and Materials, Vol. 15.01, West Conshohocken, PA, 1999.

100. D. W. Richerson, Modern Ceramic Engineering: Properties, Processing and Use in Design, Second Edition, Ed. Dekker, 1992.

101. K. Trustrum and A. de S. Jayatilaka, "On Estimating the Weibull Modulus for a Brittle Material", *Journal of Materials Science*, 14, pp.1080 (1979).

102. A. D. Papargyris, "Estimator Type and Population Size for Estimating the Weibull Modulus in Ceramics", *Journal of the European Ceramic Society*, 18 [5], pp. 451-455 (1998).

103. J. D. Sullivan and P. H. Lauzon, "Experimental Probability Estimators for Weibull Plots", *Journal of Materials Science Letters*, 5 [12], pp. 1245-1247 (1986).

104. B. Bergman,"Estimation of Weibull Parameters Using a Weight Function", *Journal of Materials Science Letters*, 5 [6], pp. 611-614 (1986).

105. M. D. Petry, T.-I. Mah and R. J. Kerans, "Validity of Using Average Diameter for Determination of Tensile Strength and weibull Modulus of Ceramic Filaments", *Journal of the American Ceramic Society*, 80 [10], pp. 2741-2744 (1997).

106. H. F. Wu and A. N. Netravali, "Weibull Analysis of Strength-Length Relationships in Single Nicalon SiC Fibres", *Journal of Materials Science*, 27 [12], pp. 3318-3324 (1992).

107. Y. Matsuo, J. X. Li and S. Kimura, "The Relationship Between Tensile Strength and Flaw-Size of Silicon Carbide Single Fibers", *Advanced Composite Materials*, 2 [1], pp. 17-28 (1992).

108. G. Simon and A. R. Bunsell, "Mechanical and Structural Characterization of the Nicalon Silicon Carbide Fiber", *Journal of Materials Science*, 19 [11], pp. 3649-3657 (1984).

109. J. Nunes, *Composite Technology Review*, 5, pp. 53 (1983).

110. V. Lavaste, J. Besson and A. R. Bunsell, "Statistical Analysis of Strength Distribution od Alumina Based Single Fibres Accounting for Fibre Diameter Variations", *Journal of Materials Science*, 30 [8], pp. 2042-2048 (1995).

111. S. N. Patankar, "Weibull Distribution as Applied to Ceramic Fibres", *Journal of Materials Science Letters*, 10 [20], pp. 1176-1181 (1991).

112. Ch. Lesniewski, C. Aubin and A. R. Bunsell, "Property-Structure Characterization of a Continuous Fine Alumina-Silica Fibre", *Composites Science and Technology*, 37 [1-3], pp. 63-78 (1990).

113. K. Jakus and V. Tulluri, "Mechanical Behavior of a Sumimoto Alumina Fiber at Room and High Temperature", *Ceramic Engineering and Science Proceedings*, 10 [9-10], 1338-1349 (1989).

114. Y. Tanabe, E. Yasuda, A. R. Bunsell, Y. Favry, and M. Inagaki, "The Strength of Pitch-Based Carbon Fibre at High Temperature", *Journal of Materials Science*, 26 [6], pp. 1601-1604 (1991).

115. J. J. Masson, K. Schulte, F. Girot and Y. Le Petitcorps, "Characterization of a C-Al Metal Matrix Composite Precursor", *Materials Science and Engineering*, A135 [1-2], pp. 59-63 (1991).

116. S-H. Own, R. V. Subramanian and S. C, Saunders, "A Bimodal Lognormal Model of the Distribution of the Strength of Carbon Fibres", *Journal of Materials Science*, 21 [11], pp. 3912-3920 (1986).

117. J. B. Jones, J. B. Barr and R. E. Smith, "Analysis of Flaws in High Strength Carbon Fibers from Mesophase Pitch", *Journal of Materials Science*, 15 [10], pp. 2455-2465 (1980).

118. Z. R. Xu, K. K. Chawla and X. Li, "Effect of High Temperature Exposure on the Tensile Strength of Alumina Fiber Nextel 610", *Materials Science and Engineering*, A171 [1-2], pp. 249-256 (1993).

119. J. K. R. Weber, J. J. Felten, B. Cho and P. C. Nordine, "Glass Fibers of Pure and Erbium- or Neodymium-Doped Yttria-Alumina Compositions", *Nature*, 393, pp. 769-771, (1998).

120. Y.-M. Sung, S. A. Dunn and J. A. Koutsky, "The Effect of Boria and Titania Addition on the Crystallization ans Sintering Behavior of LiO_2-Al_2O_3-$4SiO_2$ Glass", *Journal of the European Ceramic Society*, 14, pp. 455-462 (1994).

121. Y.-M. Sung, K.-Y. Yon, S. A. Dunn and J. A. Koutsky, "Wetting Behavior and Mullite Formation at the Interface of Inviscid Melt-Spun CaO-Al_2O_3 Fibre Reinforced Al-Si Alloy (4032) Composite", *Journal of Materials Science*, 29, pp. 5583-5588 (1994).

122. Y.-M. Sung, "Calcia-Alumina Fibre-Reinforced Al 7075 Alloy Composites Produced by Melt Infiltration: Interfacial Wetting and Reaction", *Journal of Materials Science*, 32, pp. 1069-1073 (1997).

123. M. Bass, Editor, Handbook of Optics Vol. 2: Devices, Measurements and Properties, Second Edition, McGraw Hill, New York, 1995.

124. B. D. Cullity, "Precise Parameters Measurements" in Elements of X-ray Diffraction, Second Edition, 1978.

125. V. Wilms and H. Herman, "Plasma Spraying of Al_2O_3 and Al_2O_3-Y_2O_3", *Thin Solid Films*, 39 [1-3], pp. 251-262 (1976).

126. P. T. Serjeant and R. Roy, *Journal of the American Ceramic Society*, 50, pp. 500 (1967).

127. A. C. Pierre, PhD Thesis, Dept. of Materials Science and Engineering, MIT, Cambridge, Mass., USA, 1985.

128. A. L. Dragoo and J. J. Diamond, "Transitions in Vapor-Deposited Alumina from 300° to 1200°C", *Journal of the American Ceramic Society*, 50 [11], pp. 568-574 (1967).

129. H. P. Rooksby, *Journal of Applied Chemistry*, 8, pp. 35-49 (1958).

130. O. Yamaguchi, K. Takeoka, K. Hirota, H. Takano and A. Hayashida, "Formation of Alkoxy-derived Yttrium Aluminium Oxides", *Journal of Materials Science*, 27, pp. 1261-1264 (1992).

131. M. L. Keith and R. Roy, "Structural Relations Among Double Oxides of Trivalent elements" *American Mineralogist*, 39, pp. 1-23 (1954).

132. S. Geller, *Journal of Applied Physics*, 31, pp. 30S (1960).

133. C. P. Khattak and F. F. Y. Wang, "Perovskite and Garnets" in Hanbook on the Physics and Chemistry of Rare Earths, edited by K. A. Gschneidner, Jr and L. Eyring, North-Holland Publishing Company, 1979.

134. C. S. Ray, and D. E. Day, "Determining the Nucleation Rate Curve for Lithium Disilicate Glass by Differential Thermal Analysis", *Journal of the American Ceramic Society*, 73 [2], pp. 439-442 (1990).

135. C. S. Ray, and D. E. Day, "Nucleation and Crystallization in Glasses as Determined by DTA", *Ceramic Transactions*, Nucleation and Crystallization in Liquids and Glasses, Edited by M. C. Weinberg, University of Arizona, The American Ceramic Society, 30, pp. 207-223 (1993).

136. X. J. Xu, C. S. Ray, and D. E. Day, "Nucleation and Crystallization of $Na_2O \cdot 2CaO \cdot 3SiO_2$ Glass by Differential Thermal Analysis", *Journal of the American Ceramic Society*, 74 [5], pp. 904-914 (1991).

137. H. E. Kissinger, "Variation of Peak Temperature with Heating Rate in Differential Thermal Analysis", *Journal of Research of the National Bureau of Standards*, 57 [4], pp. 217-221 (1956).

138. H. E. Kissinger, "Reaction Kinetics in Differential Thermal Analysis", *Analytical Chemistry*, 29 [11], pp. 1702-1706 (1957).

139. J. A. Augis and J. E. Bennett, "Calculation of the Avrami Parameters for Heterogeneous Solid state Reactions Using a Modification of the Kissinger Method", *Journal of Thermal Analysis*, 13, pp. 283-292 (1978).

140. W. Wm. Wendlandt, Thermal Analysis, 3rd Edition, John Wiley & Sons, 1986.

141. R. Melling, F. W. Wilburn, and R. M. McIntosh, "Study of Thermal Effects Observed by Differential Thermal Analysis – Theory and Its Application to Influence of Sample Parameters on a Typical DTA Curve", *Analytical Chemistry*, 41 [10], pp. 1275-1286 (1969).

142. R. C. Mackenzie, Editor, The Differential Thermal Investigation of Clays, Mineralogical Society, London, 1957.

143. T. Ozawa, "Kinetics of non-isothermal Crystallization", *Polymer*, 12, pp. 150-158 (1971).

144. Y.-M. Sung and J.-H. Sung, " Crystallization Behavior of Calcium Aluminate Glass Fibres-Part I Differential Thermal Analysis Study", *Journal of Materials Science*, 33 [19], pp. 4733-4737 (1998).

145. A. Marotta, and A. Buri, "Kinetics of Devitrification and Differential Thermal Analysis", *Thermochimica Acta*, 25, pp. 155-160 (1978).

146. E. D. Zanotto, A. Galhardi, "Experimental Test of the General Theory of Transformation Kinetics: Homogeneous Nucleation in a $Na_2O\cdot 2CaO\cdot 3SiO_2$ Glass", *Journal of Non-Crystalline Solids*, 104, pp. 73-80 (1988).

147. J. Málek, "The Applicability of Johnson-Mehl-Avrami Model in the Thermal Analysis of the Crystallization Kinetics of Glasses", *Thermochimica Acta*, 267, pp. 61-73 (1995).

148. V. B. Glushkova, V. A. Krzhizhanovskaya, O. N. Egorova, Yu. P. Udalov and L. P. Kachalova, "Interaction of Yttrium and Aluminum Oxides", Plenum Publishing Corporation, 1983, pp. 80-84. Translated from *Izvestiya Akademii Nauk SSSR, Neorg. Mater.*, 19 [1], pp. 95-99 (1983).

149. R. S. Hay, "Phase Transformations and Microstructure Evolution in Sol-Gel Derived Yttrium-Aluminum Garnet Films", *Journal of Materials Research*, 8 [3], pp. 578-604 (1993).

150. H. Haneda, Y. Miyazawa and S. Shirasaki, "Oxygen Diffusion in Single Crystal Yttrium Aluminum Garnet", *Journal of Crystal Growth*, 68, pp. 581-588 (1984).

151. J. M. Dynys, R. L. Coble, W. S. Coblenz and R. M. Cannon, "Mechanisms of Atom Transport during Initial Stage Sintering of Al_2O_3" in Sintering Processes, Edited by G. C. Kuczynski, Plenum Press, New York, pp. 391-404, 1980.

152. E. G. Moya, F. Moya, B. Lesage, M. K. Loudjani and C. Grattepain, "Yttrium Diffusion in α-Alumina Single Crystal", *Journal of the European Ceramic Society*, 18, pp. 591-594 (1998).

153. I. Sakaguchi, H. Haneda and J. Tanaka, "Effect of Composition on the Oxygen Tracer Diffusion in Transparent Yttrium Aluminum garnet (YAG) Ceramics", *Journal of the American Ceramic Society*, 79 [6], pp. 1627-1632 (1996).

154. M. Le Gall, B. Lesage and J. Bernardini, "Self-diffusion in α-Al_2O_3 – I. Aluminium Diffusion in Single Crystals", *Philosophical Magazine A*, 70 [5], pp. 761-773 (1994).

155. D. Prot and C. Monty, "Self-diffusion in α-Al_2O_3 – II. Oxygen Diffusion in Single Crystals", *Philosophical Magazine A*, 73 [4], pp. 899-917 (1996).

156. M. Le Gall, A. M. Huntz, B. Lesage and C. Monty, "Self-diffusion in α-Al_2O_3 – III. Oxygen Diffusion in Single Crystals Doped with Y_2O_3", *Philosophical Magazine A*, 73 [4], pp. 919-934 (1996).

157. D. Prot, M. Le Gall, B. Lesage, A. M. Huntz and C. Monty, "Self-diffusion in α-Al_2O_3 – IV. Oxygen Grain-Boundary Self-Diffusion in Undoped and Yttria-Doped Alumina Polycrystals", *Philosophical Magazine A*, 73 [4], pp. 935-949 (1996).

158. Y-M. Sung, S. A. Dunn and J. A. Koutsky, "Crystallization of Inviscid Melt Spun (IMS) Calcia-Alumina (CA) Eutectic Fibres", *Ceramics International*, 21 [3], pp. 169-172 (1995).

159. J.-R. Lo and T.-Y. Tseng, "Phase Development and Activation Energy of the Y_2O_3-Al_2O_3 System by a Modified Sol-Gel Process", *Materials Chemistry and Physics*, 56, pp. 56-62 (1998).

160. P. Wei and L. Rongti, "Crystallization Kinetics of the Aluminum Silicate Glass Fiber", *Materials Science and Engineering*, A271, pp. 298-305 (1999).

161. T. Takei, Y. Kameshima, A. Yasumori and K. Okada, "Crystallization Kinetics of Mullite in Alumina-Silica Glass Fibers", *Journal of the American Ceramic Society*, 82 [10], pp. 2876-2880 (1999).

162. T. T. Shih, "An Evaluation of the Probabilistic Approach to Brittle Design", *Engineering Fracture Mechanics*, 13, pp. 257-271 (1980).

163. W. Weibull, and S. Sweden, "A Statistical Distribution Function of Wide Applicability", *Journal of Applied Mechanics*, 18, pp. 293-297 (1951).

164. S. van der Zwaag, "The Concept of Filament Strength and the Weibull Modulus", *Journal of Testing and Evaluation*, 17, pp. 292-298 (1989).

165. B. Bergman, "On the Estimation of the Weibull Modulus", *Journal of Materials Science Letters*, 3, pp. 689-692 (1984).

APPENDIX A

WEIBULL STATISTICS

Fracture in ceramics is governed generally by processing flaws, making engineering design difficult. To date, strength characterization has been carried out using probabilistic methods.

It is known that the strength distribution of a set of samples does not follow a normal distribution. Because failure occurs at one flaw (the critical flaw), failure can be described by weakest link theory [162]. A probability function which describes the strength distribution of such materials is the Weibull function [163]. Weibull statistics are used almost exclusively in the characterization of strength distributions in ceramics.

Even though their simple geometrical form, filaments can be characterized by a large number of structural, mechanical, physical, and chemical parameters. One of the most important filament properties is the filament strength. Unlike physical parameters such as elastic modulus and thermal expansion coefficient, filament strength is a statistical parameter which cannot be fully described by a single value. The statistical

distribution of filament strengths at the monofilament level can usually be described by the so-called Weibull model.

A.1 Mathematical Formulation

The statistical description of the filament strength started with the work of Weibull [163, 164]. His model and later modifications of this model are statistical models that are not related to the physical nature of the fracture process. Implicit in the model in its simplest form, as described here, is the assumption that failure is due to sudden catastrophic growth of pre-existing defects. Each defect corresponds to a certain local failure stress. Failure at the most serious defect (i.e., the defect with the lowest fracture stress) leads to the immediate failure of the entire sample. The fracture process is therefore of a perfectly brittle nature and hence independent of time and environment. It is assumed that the defects are homogeneously distributed throughout the sample or, in the case of filaments, along the actual filament. Furthermore, it is assumed that the strength distribution along a filament is of the same form as between individual filaments.

In this model a filament is regarded as a single chain of imaginary unit of length L_0, each having a certain failure stress σ_{fi} (Figure A.1). Let $P_1(\sigma)$ be the probability of failure due to a stress σ for one unit, Then the probability of survival of that unit equals 1 - $P_1(\sigma)$. For the entire serial chain of N units the cumulative failure probability equals P_N with

$$P_N(\sigma) = 1 - [1 - P_1(\sigma)]^N \qquad \text{(A.1)}$$

or for very large N:

$$P_N(\sigma) = 1 - \exp[-N \cdot P_1(\sigma)] \tag{A.2}$$

Since N is proportional to the length, L, of the filament, Equation A.2 can be rewritten as

$$P = 1 - \exp\left[\frac{L}{L_0}\phi(\sigma)\right] \tag{A.3}$$

where $\phi(\sigma)$ is an unknown function. On empirical grounds, Weibull assumed a power law relation for $\phi(\sigma)$:

$$\phi(\sigma) = (\sigma/\sigma')^m \tag{A.4}$$

where σ is the applied stress and σ' a constant scale parameter with the same dimensions as used for the stress. The parameter m is dimensionless and is called the *Weibull modulus*. Combining Equations A.3 and A.4 yields the following equation for the cumulative failure probability function, P (i.e., the fraction of units or samples which fail at or below a stress σ):

$$P = 1 - \exp\left[-\frac{L}{L_0}\cdot\left(\frac{\sigma}{\sigma'}\right)^m\right]$$

which is usually written as

$$P = 1 - \exp\left[-L\cdot\left(\frac{\sigma}{\sigma_0}\right)^m\right] \tag{A.5}$$

where L is the gage length in meters and σ_0 no longer has simple units of stress.

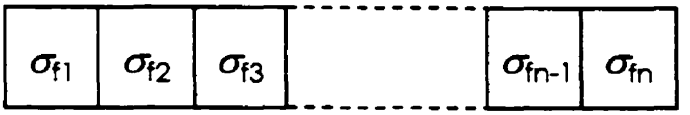

Figure A.1 Schematic diagram of a fiber consisting of n units with fracture stresses σ_{fi}.

Figure A.2 shows the cumulative failure probability versus the applied stress for various values of m. From this figure it is evident that a high value for m corresponds to a narrow fracture stress distribution function.

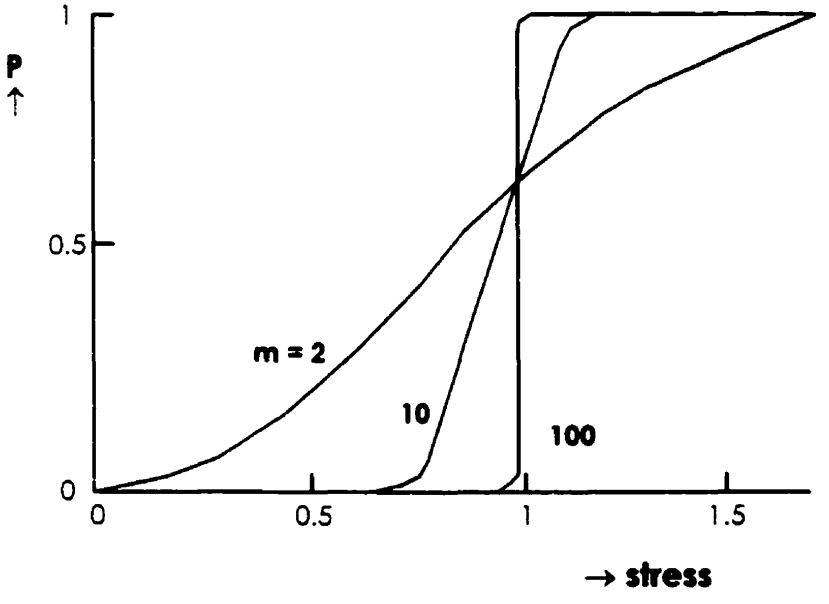

Figure A.2 Cumulative failure probability versus applied stress for various values of m ($\sigma_0 = 1$, $L = 1$).

In practice, rather than showing P versus σ it is advisable to plot $\ln[\ln(1/1 - P] - \ln(L)$ versus $\ln(\sigma)$, since this yields a linear dependence with slope m; rearrangement of Equation A.5 gives

$$\ln\left[\ln\left(\frac{1}{1-P}\right)\right] - \ln L = m \cdot \ln(\sigma) - m \cdot \ln(\sigma_0) \qquad \text{(A.6)}$$

In Figure A.3, the curves of Figure A.2 are represented in such a Weibull plot. They show that the shape of the fracture stress distribution is only determined by the magnitude of m.

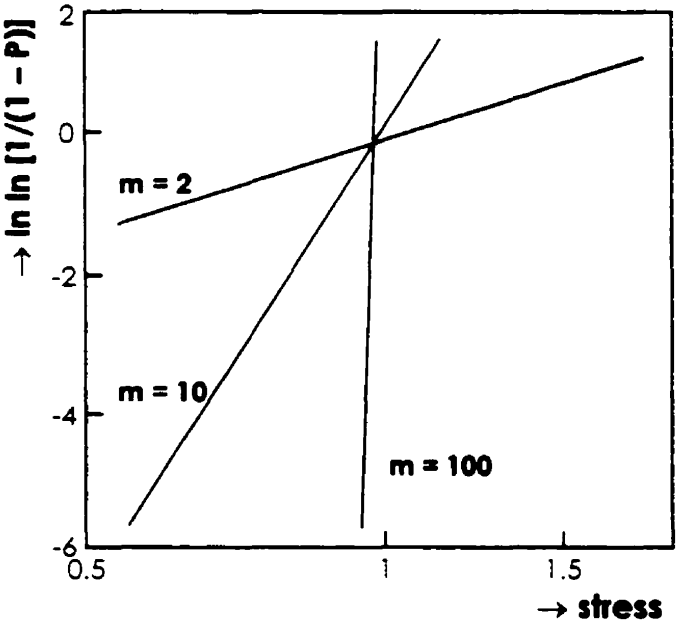

Figure A.3 Curves of Figure A.2 replotted in a Weibull plot.

The Weibull modulus is usually determined from a Weibull plot as mentioned before. However, the Weibull modulus can also be estimated from the variation coefficient of the fracture strength (the standard deviation s divided by the average value), since

$$\text{var.coeff.} = \frac{s}{\langle\sigma\rangle} = \frac{\left[\Gamma(1+2/m) - \Gamma^2(1+1/m)\right]}{\Gamma(1+1/m)} \tag{A.7}$$

The variation coefficient is independent of the gage length L and of σ_0. The following is a simple approximation of Equation A.7 of determining the Weibull modulus from the variation coefficient that yields a reasonably good estimate for m.

$$m \approx \frac{1.2}{(s/\langle\sigma\rangle)} \tag{A.8}$$

In Weibull statistics, the cumulative probability function $P(\sigma)$, the probability of failure at or below a stress, σ, for a constant tested volume, is given by

$$P(\sigma) = 1 - \exp\left[-\left(\frac{\sigma}{\sigma_0}\right)^m\right] \tag{A.9}$$

where m is the Weibull modulus which describes the flaw size distribution (and thus the data scatter), σ is the applied stress, and σ_0 is a scale parameter with the same dimensions as σ (often selected as the characteristic stress, at which the probability of failure is 0.632). Note that, in Equation A.9, all samples are assumed to have the same volume and stress distribution. Equation 1 is a two-parameter probability function. A plot of ln[ln(1/1 - P] against ln(σ) has slope m.

This probability function is generally fitted to tensile strength test data. The procedure is to measure the strength of a set of fibers or filaments of the test material. The next step in the analysis is to convert this set of test results into an experimental

probability distribution. This is done by ordering the results from lowest tensile strength to highest. The *i*th result in the set of *n* samples is assigned a cumulative probability of failure, P_i. The functions used to calculate these probabilities are called estimators.

The simplest (and possibly most common) estimator is

$$P_i = \frac{i}{n+1} \tag{A.10}$$

This estimator is generally thought to bias the measurements to a lower modulus. A better (and also common) estimator is

$$P_i = \frac{i-0.5}{n} \tag{A.11}$$

Two other estimators which are employed are

$$P_i = \frac{i-0.3}{n+0.4} \tag{A.12}$$

and

$$P_i = \frac{i-3/8}{n+1/4} \tag{A.13}$$

although their use is less widespread.

The accuracy of these estimators has been investigated using computer-generated "experimental" data [165]. These data were produced by Monte Carlo techniques in which random numbers were biased by a two-parameter Weibull function (Equation A.9) with known m and σ_0.

After an investigation in which actual experimental results were employed rather than using computer-generated data, it was found that the most successful estimator seemed to be $(i - 0.5)/n$, for which the predicted modulus was essentially independent of sample size for sample sizes of 20 or greater. Both $(i - 0.3)/(n + 0.4)$ and $(i - 3/8)/(n + 1/4)$ yielded conservative values of Weibull modulus. It has been recommended that the estimator $(i - 3/8)/(n + 1/4)$ be used for very small sample sizes (approximately 10). The less certain estimator was $i/(n + 1)$ which yielded a value for the modulus which was low for all subset sizes examined; even at a sample size of 100, the modulus from this estimator had not reached an asymptotic value. None of the estimators predicts a reasonable value for sample sizes less than 20, and such small sample sizes are not recommended [102, 103].

APPENDIX B

LATTICE PARAMETER CALCULATION

B.1 Cohen's Method

Many applications of x-ray diffraction require precise knowledge of the lattice parameter of the material under study. In the main, these applications involve solid solutions; since the lattice parameter of a solid solution varies with the concentration of the solute, the composition of a given solution can be determined from a measurement of its lattice parameter. Thermal expansion coefficients can also be determined, without a dilatometer, by measurements of lattice parameter as a function of temperature in a high-temperature diffractometer. Or the stress in a material may be determined by measuring the expansion or contraction of its lattice as a result of that stress. Since, in general, a change in solute concentration (or temperature, or stress) produces only a small change in lattice parameter, rather precise parameter measurements must be made in order to measure these quantities with any accuracy.

The process of measuring a lattice parameter is a very indirect one, and is fortunately of such a nature that high precision is fairly easy obtainable. The parameter *a*

of a cubic substance is directly proportional to the spacing d of any particular set of lattice planes. If we measure the Bragg angle θ for this set of planes, we can use the Bragg law to determined d and, knowing d, we can calculate a. But it is sin θ, not θ, which appears in the Bragg law. Precision in d, or a, therefore depends on precision in sin θ, a derived quantity, and not on precision in θ, the measured quantity. This is fortunate because the value of sin θ changes very slowly with θ in the neighborhood of 90°, as inspection of Figure B.1. For this reason, a very accurate value of sin θ can be obtained from a measurement of θ which is itself not particularly precise, *provided that θ is near 90°*.At $\theta = 85°$, for example, a 1 percent error in θ leads to an error in sin θ of only 0.1 percent. Stated in another way, the angular position of a diffracted beam is much more sensitive to a given change in plane spacing when θ is large than when it is small.

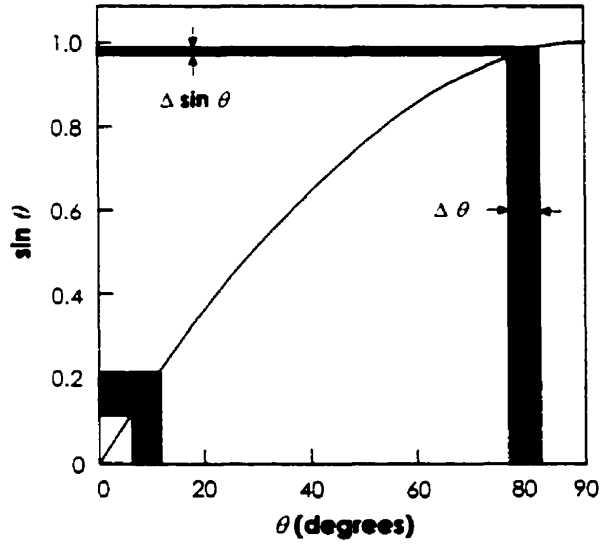

Figure B.1 The variation of sin θ with θ. The error in sin θ caused by a given error in θ decreases as θ increases ($\Delta\theta$ exaggerated).

B.1.1 Cubic System

The most accurate value of the lattice parameter of a cubic substance is found by plotting the value of a calculated for each reflection against a particular function, which depends on the kind of diffractometer used, and extrapolating to a value a_0 at $\theta = 90°$. Two different things are accomplished by this procedure: (a) systematic errors are eliminated by selection of the proper extrapolation function, and (b) random errors are reduced in proportion to the skill of drawing the best straight line through the experimental points. M. U. Cohen proposed, in effect, that the least-squares method be used to find the best straight line so that the random errors would be minimized in a reproducible and objective manner.

Suppose a cubic substance is examined in a diffractometer. Then Equation B.1, namely

$$\frac{\Delta d}{d} = \frac{\Delta a}{a} = K\cos^2\theta \tag{B.1}$$

defines the extrapolation function. But instead of using the least-squares method to find the best straight line on a plot of a against $\cos^2\theta$, Cohen applied the method to the observed $\sin^2\theta$ values directly. By squaring the Bragg law ($\lambda = 2d\sin\theta$) and taking logarithms of each side, we obtain

$$\ln\sin^2\theta = \ln\left(\frac{\lambda^2}{4}\right) - 2\ln d\,. \tag{B.2}$$

Differentiation then gives

$$\frac{\Delta \sin^2\theta}{\sin^2\theta} = -\frac{2\Delta d}{d}. \tag{B.3}$$

By substituting this into Equation B.1 we find how the error in $\sin^2\theta$ varies with θ:

$$\Delta \sin^2\theta = -2K \sin^2\theta \cos^2\theta = D \sin^2 2\theta, \tag{B.4}$$

where D is a new constant. Now the true value of $\sin^2\theta$ for any diffraction line is given by

$$\sin^2\theta(\text{true}) = \frac{\lambda^2}{4a_0^2}\left(h^2 + k^2 + l^2\right),$$

where a_0, the true value of the lattice parameter, is the quantity we are seeking. But

$$\sin^2\theta(\text{observed}) - \sin^2\theta(\text{true}) = \Delta \sin^2\theta,$$

$$\sin^2\theta - \frac{\lambda^2}{4a_0^2}\left(h^2 + k^2 + l^2\right) = D \sin^2 2\theta,$$

$$\sin^2\theta = C\alpha + A\delta, \tag{B.5}$$

where

$$C = \frac{\lambda^2}{4a_0^2},\ \alpha = \left(h^2 + k^2 + l^2\right),\ A = \frac{D}{10},\ \text{and}\ \delta = 10 \sin^2 2\theta.$$

(The factor 10 is introduced into the definitions of the quantities A and δ solely to make the coefficients of the various terms in the normal equations of the same order of magnitude).

The experimental values of $\sin^2\theta$, α, and δ are now substituted into Equation B.5 for each of the n back–reflection lines used in the determination. This gives n equations in the unknown constants C and A, and these equations can be solved for the most probable values of C and A by the method of least squares. Once C is found, a_0 can be

calculated directly from the relation given above; the constant A is related to the amount of systematic error involved and is constant for any diffractogram, but varies slightly from one diffractogram to another. The two normal equations we need to find C and A are found from Eq. B.5 and the rules previously given. They are

$$\sum \alpha \sin^2 \theta = C\sum \alpha^2 + A\sum \alpha\delta,$$

$$\sum \delta \sin^2 \theta = C\sum \alpha\delta + A\sum \delta^2 .$$

B.1.2 Orthorhombic System

Cohen's Method of determining lattice parameters is even more valuable when applied to noncubic substances. Cohen's method provides a direct means of determining these parameters, although the equations are naturally more complex than those needed for cubic substances. For example, suppose that the substance involved is orthorhombic, then

$$\sin^2 \theta(\text{true}) = \frac{\lambda^2}{4}\cdot\frac{h^2}{a_0^2} + \frac{\lambda^2}{4}\cdot\frac{k^2}{b_0^2} + \frac{\lambda^2}{4}\cdot\frac{l^2}{c_0^2}$$

and

$$\sin^2 \theta - \frac{\lambda^2}{4a_0^2}(h^2) - \frac{\lambda^2}{4b_0^2}(k^2) - \frac{\lambda^2}{4c_0^2}(l^2) = D\sin^2 2\theta .$$

If the pattern is made in a diffractometer, by rearranging this equation and introducing new symbols, we obtain

$$\sin^2 \theta = C\alpha + B\gamma + E\varepsilon + A\delta , \qquad \text{(B.6)}$$

where

$$C = \frac{\lambda^2}{4a_0^2},\ \alpha = h^2,\ B = \frac{\lambda^2}{4b_0^2},\ \gamma = k^2,\ E = \frac{\lambda^2}{4c_0^2},\ \varepsilon = l^2,$$

$$A = \frac{D}{10}, \text{ and } \delta = 10\sin^2 2\theta .$$

The values of C, B, E, and A, of which only the first three are really needed, are found from the three normal equations:

$$\sum \alpha \sin^2\theta = C\sum \alpha^2 + B\sum \alpha\gamma + E\sum \alpha\varepsilon + A\sum \alpha\delta ,$$

$$\sum \gamma \sin^2\theta = C\sum \alpha\gamma + B\sum \gamma^2 + E\sum \gamma\varepsilon + A\sum \gamma\delta ,$$

$$\sum \varepsilon \sin^2\theta = C\sum \alpha\varepsilon + B\sum \varepsilon\gamma + E\sum \varepsilon^2 + A\sum \varepsilon\delta ,$$

$$\sum \delta \sin^2\theta = C\sum \alpha\delta + B\sum \delta\gamma + E\sum \delta\varepsilon + A\sum \delta^2 .$$

B.1.3 Plane Spacings

The value of d, the distance between adjacent planes in the set (hkl), may be found from the following equations.

Cubic:
$$\frac{1}{d^2} = \frac{h^2 + k^2 + l^2}{a^2}$$

Orthorhombic:
$$\frac{1}{d^2} = \frac{h^2}{a^2} + \frac{k^2}{b^2} + \frac{l^2}{c^2}$$